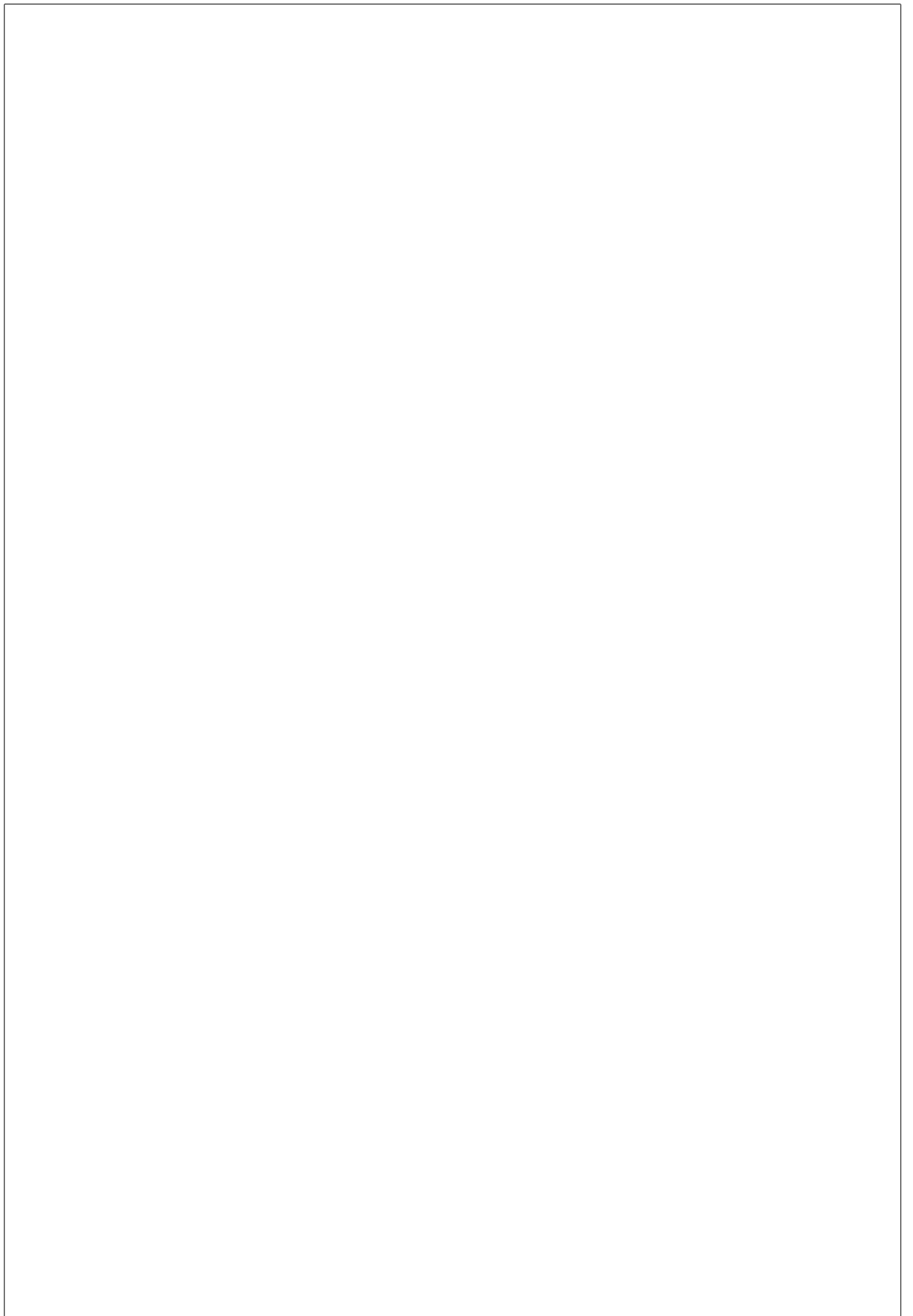


---

---



---

# Todo list

thickness . . . . .	18
resolution value . . . . .	19
resolution value . . . . .	19
optical diffraction, shadows . . . . .	19
Complete implantation parameters . . . . .	29
how much? . . . . .	31
time? . . . . .	31
Hier fehlt jeweils ein kurzer satz was die dinger bewirken sollen. . . . .	36
warum? . . . . .	36
type . . . . .	37
eher nur vermutung . . . . .	41
What does that mean? . . . . .	43
was soll ich als saettigungsleistung angeben, emitter starb vor messende . . . . .	52
ich glaub, das ist bullshit . . . . .	57
der satz muss noch einmassiert werden . . . . .	57
put in correct numbers . . . . .	68
warum schaut das spectrum anders aus als das, was einzeln geplottet ist? . . . . .	70
cps zu a.u. aendern . . . . .	84
zahlen fuer sat eintragen . . . . .	84
put in pictures for fdtd results and reference them . . . . .	85

---

---

# Contents

<b>Table of Contents</b>	i
<b>List of Figures</b>	i
<b>List of Tables</b>	ii
<b>1 Introduction</b>	1
<b>2 Silicon Vacancy Centers in Diamond</b>	6
2.1 Diamond as a host lattice . . . . .	6
2.2 Classification of diamond . . . . .	7
2.2.1 Classification by impurities . . . . .	8
2.2.2 Classification by crystallinity . . . . .	9
2.3 Silicon-vacancy center . . . . .	9
2.3.1 Luminescence properties . . . . .	11
<b>3 Photoluminescence Setup</b>	17
3.1 Confocal Setup . . . . .	17
3.2 Surface Imaging . . . . .	19
3.3 Spectrometer . . . . .	20
3.4 HBT . . . . .	21
<b>4 Fabrication of Nanodiamonds</b>	24
4.1 HPHT . . . . .	25
4.2 CVD . . . . .	25
4.3 Wet-Milling . . . . .	27
4.3.1 Wet-Milled HPHT Nanodiamonds . . . . .	29
4.3.2 Wet-Milled CVD Nanodiamonds . . . . .	29
4.3.3 Doubly Wet-Milled Implanted Nanodiamonds Implanted With Silicon . . . . .	30
4.4 Iridium Substrate . . . . .	32
4.4.1 Preparation of The Substrate . . . . .	33
4.5 Listing of available samples . . . . .	33
<b>5 Quality of Nanodiamonds</b>	35

5.1	Quality-improving Post-Processing Treatments . . . . .	36
5.1.1	Annealing and Oxidation . . . . .	36
5.1.2	Surface Treatment With Gas And Plasma . . . . .	36
5.2	Raman Measurements . . . . .	37
5.2.1	Surface Contamination . . . . .	38
5.2.2	Defect Concentration . . . . .	39
5.2.3	Lattice Strain . . . . .	39
5.3	Transmission Electron Spectroscopy Measurements . . . . .	40
5.3.1	Crystallinity and Grain Boundaries . . . . .	41
<b>6</b>	<b>Spectral Distribution</b>	<b>42</b>
6.1	Photoluminescence spectra . . . . .	42
6.1.1	Zero-phonon-line . . . . .	43
6.1.2	Sideband . . . . .	48
6.1.3	Cryostatic Measurements . . . . .	50
6.2	Photon correlation measurements . . . . .	51
6.3	Photostability . . . . .	53
<b>7</b>	<b>Coupling of Nanodiamonds to Photonic Structures</b>	<b>56</b>
7.1	Additional Experimental Methods . . . . .	57
7.1.1	Nano-manipulator . . . . .	58
7.1.2	Determination of The Position of Nanodiamonds . . . . .	59
7.1.3	The Pick-And-Place Process . . . . .	61
7.2	Coupling SiV centers to Vertical-Cavity Surface Emitting Lasers . . . . .	63
7.2.1	Vertical-Cavity Surface Emitting Lasers . . . . .	63
7.2.2	SiV center in a Vertical-Cavity Surface Emitting Laser . . . . .	64
7.3	Coupling Nanodiamonds to Optical Antennas . . . . .	71
7.3.1	Plasmonic Antennas . . . . .	71
7.3.2	Plasmonic Antenna Design and Simulation . . . . .	74
7.3.3	SiV center in a Plasmonic Double Bowtie Antenna . . . . .	76
<b>Summary and Conclusions</b>		<b>87</b>

---

---

# List of Figures

2.1	Face-centered cubic diamond lattice . . . . .	7
2.2	Reduced light extraction efficiency of diamond due to refraction . . . . .	7
2.3	Split-vacancy configuration for SiV centers in diamond . . . . .	10
2.4	Band gap of SiV centers hosted in diamond . . . . .	12
2.5	Huang-Rhys model of vibrational transitions . . . . .	13
2.6	Fluorescence spectra of SiV centers at room temperature . . . . .	15
2.7	Fluorescence spectra of SiV centers at low temperature . . . . .	16
3.1	Confocal microscopy setup . . . . .	18
3.2	Spectrometer and HBT setup . . . . .	20
3.3	Sketch of typical $g^{(2)}$ functions . . . . .	22
4.1	CVD production method . . . . .	26
4.2	Example of CVD nanodiamonds . . . . .	27
4.3	Wet-milling in a vibrational mill . . . . .	28
4.4	Distribution of nanodiamonds ontop of an iridium substrate . . . . .	29
4.5	(a) SEM picture of nanodiamonds sunken into a silicon substrate after annealing at 900 °C for 3 h. Magnification 20 000. (b) SEM image of the microdiamonds after milling on an iridium substrate, but before implantation. In the middle of the picture, there is a reference cross milled into the iridium substrate with a focused ion beam. Its size amounts to 10 µm. It can be seen, that the microdiamonds exhibit sizes of a few micrometer. . . . .	31
4.6	(a) Microscope image of a drop of water on an iridium substrate cleaned with Piranha etch. This picture was used to estimate the contact angle. (b) SEM picture of an 60 nm iridium layer that peeled off the substrate after an ultrasonic bath. . . . .	32
5.1	Raman spectrum of a single nanodiamond . . . . .	38
5.2	TEM imaging of a single nanodiamond . . . . .	40
6.1	Spectral distribution of SiV center ZPLs . . . . .	43
6.2	Sample SiV center photoluminescence spectra for group V and group H	44
6.3	Comparison of obtained SiV center linewidths with available data sources	45
6.4	Zoom-in onto SiV centers of the group V	47

6.5	Calculated dependence between SiV center ZPL and lattice pressure . . . . .	47
6.6	Side band peaks for SiV centers . . . . .	49
6.7	Shift of dominant side band peaks for SiV centers . . . . .	49
6.8	todo fix figure . . . . .	50
6.9	todo fix figure . . . . .	51
6.10	Intensity autocorrelation measurements for group H and group V . . . . .	52
6.11	Time trace of a single emitter. . . . .	53
6.12	Distributions of bright and dark state intervals . . . . .	54
7.1	Nano-manipulator in a SEM setup . . . . .	58
7.2	Detail of nano-manipulator tips . . . . .	59
7.3	Cross markers assisting identification of nanodiamonds . . . . .	60
7.4	Combining fluorescence light and laser scanning microscope to identify nanodiamonds . . . . .	61
7.5	Sketch of the pick-and-place process . . . . .	61
7.6	Nano-manipulator carrying a nanodiamond . . . . .	62
7.7	Sketch of a vertical-cavity surface emitting laser . . . . .	64
7.8	SEM image of an array of VCSELs . . . . .	65
7.9	Emission spectra and optical power of VCSEL Bm4 . . . . .	66
7.10	Scans of VCSELs with and without SiV center . . . . .	67
7.11	SiV center properties before and after pick-and-place . . . . .	68
7.12	Comparison of intensities between VCSEL Bm4 and VCSEL Bm2 . . . . .	68
7.13	Comparison of spectra between VCSEL Bm4 and VCSEL Bm2 . . . . .	69
7.14	Reflectivity of VCSEL Bm4 . . . . .	70
7.15	Schematic of a double bowtie antenna . . . . .	72
7.16	Hot-spot of a double bowtie antenna . . . . .	73
7.17	SEM images of double bowtie structures. . . . .	74
7.18	Simulation of the resonance spectrum of a double bowtie antenna . . . . .	75
7.19	Localizing suitable nanodiamonds . . . . .	77
7.20	Properties of a nanodiamond containing an ensemble of SiV centers . . . . .	78
7.21	Pick-and-place coupling of nanodiamond to antenna . . . . .	79
7.22	Confocal scan of a gold double bowtie antenna . . . . .	80
7.23	Spectra of a nanodiamond coupled to an antenna . . . . .	81
7.24	Spectrum of a double bowtie antenna without nanodiamond . . . . .	81
7.25	Properties of a nanodiamond containing a few SiV centers . . . . .	84
7.26	Spectrum of preselected nanodiamond containing few SiV centers . . . . .	84
7.27	Background-corrected spectrum of a nanodiamond in an antenna . . . . .	85

---

---

# List of Tables

2.1	Classification of diamond synthesized by chemical vapor deposition . . . . .	9
4.1	Samples grown with diamondoid seeds . . . . .	28
4.2	Listing of available wet-milled samples . . . . .	34

--

---

---

# Chapter 1

## Introduction

“Every competent physicist can “do” quantum mechanics, but the stories we tell ourselves about what we are doing are as various as the tales of Sheherazade, and almost as implausible.”

David J. Griffiths

The International System of Units (SI, abbreviated from the French Système international d’unités) emerged in the late 18<sup>th</sup> century as a coherent metric system of measurement with rationally related units and simple rules for combining them [?]. Since its inception it was improved and augmented continuously in an ongoing effort to accommodate continued scientific and technological progress. The current SI system is comprised of seven base units: The kilogram (kg), the second (s), the Ampere (A), the Kelvin (K), the mole (mol) and the candela (cd). Currently a redefinition of four of base units (kilogram, mole, Kelvin, Ampere) in terms of fundamental constants is under way [?, ?, ?]. The proposed change will improve the definitions of these base units to make them easier to realize experimentally, particularly for the measurement of electrical quantities [?]. It will also eliminate the last remaining base unit definition which relies on a historic material artifact, the international prototype of the kilogram. As a result all base units will, for the first time, be tied to one or more fundamental constants of nature.

As these developments are put into motion, similar discussions regarding the SI base unit for luminous intensity, the candela, have emerged. It has been suggested that it can be improved by leveraging recent advances in classical radiometry and photometry as well as the development of novel quantum devices and techniques [?].

At the time of writing the definition of the candela read:

The candela is the luminous intensity, in a given direction, of a source that emits monochromatic radiation of frequency  $540 \times 10^{12}$  Hz and that has a radiant intensity in that direction of  $638^{-1} \text{W sr}^{-1}$ .

Traditional applications relying on this definition in conjunction with accurate photometric and radiometric measurements are light design, manufacturing and use of optical

sources, detectors, optical components, colored materials and optical radiation measuring equipment [?]. In the classical regime of optical radiation high flux levels dominate. Here primary optical radiation scales for sources and detectors are generally based on cryogenic radiometry establishing a link to the SI units of electricity [?]. Other calculable sources such as synchrotron and blackbody radiators can serve as primary source scales in the ultraviolet and deep-UV regions by establishing traceability to SI units of thermometry, electricity and length [?, ?].

Scaling down to the quantum world of radiometry is associated with a loss of measurement accuracy. In this regime dedicated photon counting techniques are required to deal with the challenge of low flux levels. Since they rely on counting photons directly, in principle they can provide efficient and traceable measurements and improved uncertainties. For high-accuracy absolute radiometry in this regime, predictable single or quasi-single-photon sources and photon detectors as well as associated new quantum-based calibration methods and standards are called for. To promote the development of such technologies a reformulation of the candela has been proposed in terms of *countable* photon units [?, ?, ?, ?, ?]. Here we emphasize the distinction between *countable* and *calculable* sources of photons. The latter being available as blackbodies or synchrotron radiators.

A straightforward quantum-based reformulation has been suggested based on [?, ?]:

$$P = nh\nu, \quad (1.1)$$

where the radiant intensity per steradian  $P = 638^{-1}\text{W sr}^{-1}$  in a given direction and the photon frequency  $\nu = 540 \times 10^{12}\text{ Hz}$  are assumed to be exact with their numerical values inherited from the present definition of the candela. The anticipated proposed changes to the SI system will define Planck's constant  $h = 6.626\,070\,15 \times 10^{-34}\text{ J s}$  as an exact numerical constant [?]. As a consequence the number of photons per second per steradian in a candela  $n$  becomes a constant defined as:

$$n = \frac{P}{h\nu} \approx 4.091\,942\,9 \times 10^{15} \text{ counts s}^{-1} \text{ sr}^{-1}. \quad (1.2)$$

Given this definition of the radiant intensity of a candela in terms of countable photons, a possible formulation of the quantum candela could read:

The candela is the luminous intensity, in a given direction, of a source that emits photons of frequency  $540 \times 10^{12}\text{ Hz}$  at a rate of  $4.091\,942\,9 \times 10^{15}$  photons per second per steradian in that direction.

This definition would incur a deviation of 0.0014 % from the current value of the candela. This is an acceptable change, taking into account the fact that current experimental realizations of the candela are limited to uncertainties of 0.02 % [?]. Proposals such as this are regularly reviewed by the Consultative Committee for Photometry and Radiometry ensuring that the current best measurement practices and existing as well as emerging needs of the user community of the candela are met [?].

While a proposed formulation of a quantum-candela can be considered a small change to the SI system, a shift towards quantum based radiometric SI units is likely to become a critical enabler driving the development of accurate and traceable measurement methods on the single-photon level. In order for the definition of the quantum-candela to have practical meaning, photon counting detectors are required capable of accurately resolving single-photons. To ensure proper calibration of such devices, reliable deterministic single photon sources are key. As novel instruments and associated calibration standards emerge, our ability to work with individual photons in a wide range of applications is expected to improve [?, ?, ?, ?]. The quest for single photon sources is supported by large research projects such as "Single-Photon Sources for Quantum Technology" funded by European Metrology Research Program.

Advances in radiometry are particularly important for fields like quantum communication and quantum computing. They are heavily reliant on deterministic reliable single-photon sources and well-calibrated detectors. As such they have proven to be major driving forces in their development [?, ?]. Amongst others, some well known applications include quantum key distribution [?, ?, ?] or transmission in a quantum network [?, ?, ?].

At present several candidates for on-demand single-photon sources are available, which we shortly mention here. One possibility consists of using a laser beam attenuated such that the mean number of photons in the beam becomes close to one [?, ?, ?]. However, the mean photon number cannot be controlled perfectly and a non-zero probability remains that multiple photons are present in the beam simultaneously.

Quasi-single photon states can be realized more efficiently using photon-pairs consisting of a signal and an idler photon. Pairs are created when a photon interacts with a non-linear optical medium in a process called spontaneous parametric down-conversion (SPDC) [?, ?, ?, ?, ?, ?]. The deciding feature of the process is the strong time-correlation between signal and idler photons. If both photons are injected into individual signal paths, an detection event in one of the paths heralds the existence of a photon in the other path. SPDC pairs can thus be used to construct single-photon sources. Unfortunately, due to the poor efficiency of the SPDC process, the probability of generating pairs is unfavorable [?, ?]. Thus efforts have been undertaken to improve the efficiency [?, ?, ?].

Quantum dots emit photons by recombination of electron-hole pairs created by optical excitation or via an electric current [?, ?, ?]. The choice of semi-conducting material determines the electronic structure of the system and thus the characteristics of the emitter. Similarly, single-photons can be obtained as a result of radiative transitions between energy levels of single atoms or molecules trapped in an optical cavity [?]. While these sources have desirable properties such as high-collection efficiency, the practical usefulness is limited due to being technologically demanding. Amongst others a high vacuum is needed to operate these sources [?].

For a wide range of single photon sources, significant progress has been made towards improving purity, indistinguishability and collection efficiency [?, ?, ?, ?, ?].

As it stands, a single photon source suitable for the calibration of single-photon detectors remains difficult to realize [?]. Ideally, a standard single photon source should be emitting with a quantum efficiency of 100 % indicating that the entire excitation energy is transformed into radiation without losses. At the same time single photons should be emitted with a probability of one and subsequently collected with perfect efficiency.

Very recently, another interesting direction has been explored, identifying color centers in nanodiamonds involving silicon [?, ?] and nitrogen [?] as promising candidates for the realization of standard single photon sources [?, ?]. In particular it was shown that it is possible to absolutely calibrate single photon sources using a classical detector and a calibrated spectrometer, establishing an unbroken traceability chain to the SI system. The photon flux of the source can be controlled via the settings of the pump laser repetition rate. In this way a direct link between the high photon flux levels of the classical regime and low photon flux levels in the quantum world has been formed. For the nitrogen vacancy center a photon flux rate of  $\approx 1.4 \times 10^5$  photons per second was recorded.

In this thesis we continue researching the potential of color centers in diamond as single photon sources. More precisely, we focus on the silicon-vacancy center. In doing so we aim to add momentum to the development of single photon source as high-accuracy calibration devices and subsequently, to the development of photon counting detectors and the adoption of the quantum-candela.

The SiV center in diamond is an ideal candidate for single photon calibration purposes. It is a very efficient and stable narrow linewidth emitter, producing single photons with high intensity. Conveniently, SiV centers operate at room temperature under normal pressure and hence do not require overly sophisticated experimental setups. As an alternative to hosting SiV centers in bulk diamond, they can be implanted in nano-sized diamond grains offering increased collection efficiency. Grains containing individual SiV centers can be identified and preselected according to their properties.

In this thesis we synthesize nanodiamonds with SiV centers using a variety of different techniques. Chemical vapor deposition, high-pressure, high-temperature synthesis as well as wet-milling methods are used to produce a sizable set of samples. To investigate the samples, i.e. to study the optical properties of embedded SiV centers we rely on optical excitation. In particular, confocal microscopy is used to collect emitted fluorescent single-photons. An attached spectrometer or a Hanbury Brown and Twiss setup offer further insights into the properties of the SiV center as a single photon source.

Our work can roughly be subdivided into two larger explorations. The first, revolves around charting the luminescence properties of a large set of nanodiamonds and their hosted emitters, allowing us to establish distributions of selected SiV center properties. To our knowledge, our efforts result in the largest coherent examination of SiV centers to date. In contrast to that the second exploration focuses on individual nanodiamonds and our attempts to relocate them to different nano structures in order to achieve a coupling between SiV centers and the host structure. First we attempt to realize a controllable integrated single photon source by placing a nanodiamond containing SiV

centers on top of a vertical-cavity surface emitting laser (VCSEL). Furthermore, we combine nanodiamonds with plasmonic nano-antennas in order to enhance the emission properties of the contained SiV centers.

The thesis is structured as follows: chapter 2 introduces the reader to color centers and diamond as a host material. A discussion of SiV centers restricted to their most important luminous properties is presented. chapter 3 familiarizes the reader with the essential experimental setup and methods deployed in this thesis to study SiV center luminescence. Various relevant methods of synthesizing sample nanodiamonds containing SiV centers are presented and discussed in chapter 4. chapter 5 is dedicated to the important topic of gauging the quality of fabricated samples. The results of charting the luminous properties of our nanodiamonds samples is presented in chapter 6. Our attempts of coupling nanodiamonds hosting SiV centers to two different nano structures is investigated in chapter 7. Finally we summarize and discuss the findings of this thesis in chapter 7.3.3.

---

---

# Chapter 2

## Silicon Vacancy Centers in Diamond

In the following we introduce color centers, i.e. optically active point-defects present in a diamond lattice. We focus on color centers combining silicon impurities and lattice vacancies forming the silicon-vacancy center (SiV center). We start by presenting the most important properties of diamond and emphasize its suitability as a host for optical applications with color centers. A classification of diamond with respects to defects and impurities as well as crystallinities serves as a preparation for the introduction of methods to synthesize diamonds containing SiV centers presented in ?? . Finally, we discuss SiV centers in detail and focus on their most important optical properties which make them ideal candidates for realizing reliable single photon sources at room temperature. In particular, we zoom in on the key features of its luminescence spectrum, the zero-phonon-line and the phonon side band. Our discussion partially follows the presentation in [?, ?, ?, ?].

### 2.1 Diamond as a host lattice

Diamond is a metastable modification of carbon which is stable under normal pressure at room temperature [?]. Carbon atoms form strong  $sp^3$ -bonds with each other in a tetrahedral arrangement of neighboring atoms. The resulting  $sp^3$ -hybridized lattice is of exceptional mechanical stability, making diamond the hardest known material [?]. The crystal structure can also be interpreted as a face-centered cubic (fcc) lattice with two carbon atoms in the primitive Bravais cell, situated at  $(0, 0, 0)$   $a$  and  $(\frac{1}{4}, \frac{1}{4}, \frac{1}{4})$   $a$  with  $a = 3.567 \text{ \AA}$  denoting the lattice constant [?]. Figure 2.1 illustrates the structure.

The valence and conduction bands of diamond are separated energetically by a large direct band gap of 7.3 eV while its indirect band gap amounts to 5.5 eV [?, ?]. As a result diamonds are transparent for light of all wavelengths larger than 230 nm [?]. This transparent quality makes diamond an ideal host material for various optically active lattice defects or impurities. These induce a wide range of discrete energy levels situated in the sizable band gap. The absorption of optically active impurities or

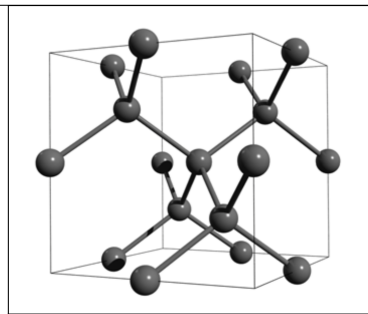


Figure 2.1: Face-centered cubic diamond lattice. Note the tetrahedral arrangements of carbon atoms. Figure reproduced with permission from [?].

impurity complexes gives rise to the observed variety of colors in diamonds, thus these impurities are commonly termed color centers [?]. Due to the exceptional mechanical stability of diamond, color centers too are very stable mechanically, another important property favorable for optical applications.

A property of diamond, detrimental to some optical applications, is its large refractive index with values of 2.49 at 360 nm and 2.4 at 800 nm respectively [?]. Thus, a portion of the light escaping from the diamond is reflected back into it, effectively reducing the efficiency of light extraction. If nanodiamonds smaller than the wavelength of the light to be collected are used, internal reflection is suppressed and the extraction efficiency can be increased [?].

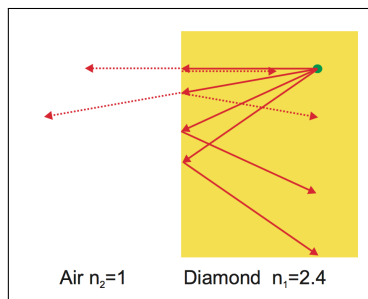


Figure 2.2: Light from a fluorescent emitter inside the diamond (green dot) undergoes reflection at the diamond-air interface. Figure reproduced with permission from [?].

## 2.2 Classification of diamond

Two major approaches for classifying diamond are commonly encountered. First, classification according to the presence or absence of certain impurities or impurity complexes. Second, classification based on different diamond crystallinities observed in the diamond. In the following both classification systems are briefly introduced.

### 2.2.1 Classification by impurities

Impurities or complexes of impurities in the diamond lattice can be optically active and thus change the optical properties of diamond. Most strikingly perhaps is the appearance of color in otherwise colorless diamond due to a sufficient concentration of such defects. Using IR absorption spectroscopy the degree of nitrogen impurities can be determined. It is used to subdivide diamonds into distinct groups named Type I and Type II [?, ?]. The groups are further subdivided as follows:

- Type Ia: With a nitrogen concentration of up to 3000 ppm most natural occurring diamonds belong to this group [?]. Nitrogen appears arranged predominantly in aggregate clusters forming complexes of impurities. These complexes are optically active, absorbing light in the blue range of the visible spectrum. Consequently Type Ia diamonds often exhibit a yellow to brownish coloration.
- Type Ib: With concentrations of up to 500 ppm nitrogen atoms appear predominantly in isolation, replacing individual carbon atoms in the diamond lattice. In addition to absorbing visible blue light, green is being absorbed as well. Type Ib diamond thus exhibits intensified the yellow or brownish coloration. While only 0.1 % of naturally occurring diamond fall into this class, almost all synthetic diamonds created using the high-pressure, high-temperature (HPHT) method are of Type Ib [?].

While Type I diamond exhibits an appreciable concentration of nitrogen, Type II diamonds lack nitrogen entirely. Type II diamond is divided into two subgroups according to the presence or absence of boron as follows:

- Type IIa: Can be considered pure as they lack boron impurities and other optically active defects [?]. They thus are colorless. Up to 2 % of naturally occurring diamond and most diamonds synthetically created using the chemical vapor deposition (CVD) method are of Type IIa [?].
- Type IIb: Contains appreciable concentrations of boron atoms replacing individual carbon atoms in the diamond lattice. Boron defects are optically active absorbing visible light ranging from red to yellow. Depending on the Boron concentration blue to gray colorations are observed. Furthermore, diamond changes from an insulator to an efficient *p*-type semiconductor in the presence of boron impurities [?].

We remark that for many modern applications of diamonds the presented “classic” categorization of diamond is insufficient. In these cases a precise quantification of the concentration and nature of various relevant impurities is called for [?, ?].

In this section we also briefly touched upon the CVD and HPHT methods, two approaches to synthetically produce diamonds. Both are relevant for this thesis and are explained in detail in chapter 4.

## 2.2.2 Classification by crystallinity

Up until now, the discussion assumed that diamond forms a lattice consisting of one giant single crystal. However, other crystallinities are possible and can be used to classify diamond. They range from mono or single crystals to polycrystalline, nano crystalline or even ultra-nano crystalline diamond films [?]. This classification is particularly useful for synthesized diamond as will be discussed in chapter 4. Table 2.1 summarizes the different sizes of diamonds or diamond films which can be achieved using variations of the CVD method.

Diamond films consist of isolated diamond grain of random orientation with sp<sub>2</sub> hybridized grain boundaries and graphite-like inclusions [?]. Carbon present in non-diamond phases, e.g. graphite or amorphous carbon gives rise to detrimental light absorption while crystal boundaries lead to increased scattering losses. As the size of diamond crystallites get smaller, the ratio of non-diamond carbon to diamond carbon increases. Thus losses are most pronounced for the smallest grain diamond films.

Table 2.1: Classification of diamonds synthesized using CVD [?].

Crystallinity	Grain size
mono crystalline	arbitrary
poly crystalline	50 nm to 10 µm
nano crystalline	10 nm to 50 nm
ultra-nano crystalline	< 10 nm

## 2.3 Silicon-vacancy center

A color center is an optically active point-defect in a crystal lattice, capable of absorbing and emitting light. Defects can consist of one or several vacant lattice sites, foreign atoms replacing lattice atoms or a combination thereof. If the presence of a defect induces discrete energy levels located in the band gap of the host material, the color center can be interpreted as its own quantum system. In other words, the color center can be viewed as a single isolated and localized artificial atom embedded in a host matrix. As such it is able to absorb light and emit single photons by means of fluorescence.

Compared to alternative single photon sources like single atoms [?], Ions [?] or individual quantum dots [?, ?], color centers offer a couple of advantages due to their solid state environment. As a result of the high mechanical stability of the host lattice color centers exhibit increased photo-stability, in particular compared to organic molecules as light sources. Furthermore the host lattices offers protection for color centers from detrimental interactions with aggressive free molecules [?]. Lastly, color centers can be

handled and investigated at room temperature, thus significantly reducing the experimental sophistication necessary to study them.

Of particular interest are color centers as single photon sources when hosted in diamond. With its transparency, exceptional stability and minimal phononic interactions at room temperature the diamond lattice is an ideal host matrix for color centers [?, ?]. While more than 500 different color centers in diamond are documented, only a small fraction has been investigated with respect to their properties as single photon sources [?]. For an in-depth review of color centers and their versatile applications see [?, ?]. The two arguably most prominent examples of well-studied color centers are vacancy centers featuring nitrogen and silicon [?, ?, ?].

The silicon-vacancy center (SiV center) in diamond and its properties is at the center of this thesis. The SiV center has been established as an reliable single photon source at room temperature. It shows very narrow emission lines with record count rates up to  $6.2 \times 10^6$  cps (counts-per-second) [?]. The emission of indistinguishable photons and the optical access of electronic spin states have been demonstrated [?, ?, ?, ?], hinting at the possibility of deploying SiV centers as spin-qubits.

A silicon-vacancy center is formed in a diamond lattice by substituting two carbon atoms by a silicon atom and a nearby empty lattice site respectively. The silicon atom occupies its energetically optimal position by sitting in-between two lattice sites. This is called “split-vacancy” configuration and induces a  $D_{3d}$  symmetry with the two vacancies and the impurity aligned along the  $\langle 111 \rangle$  diamond axis [?], see Figure 2.3.

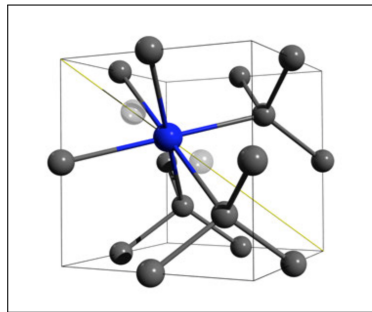


Figure 2.3: Crystal structure of the SiV center embedded into the diamond lattice: The silicon atom (blue sphere) sits in between two vacant lattice sites (white spheres) forming a “split-vacancy” configuration aligned along the  $\langle 111 \rangle$  crystallographic axis (yellow line). Figure reproduced with permission from [?].

The SiV center is known to occur in two different charge states. The first is the neutral state or  $\text{SiV}^0$  with a zero-phonon transition at 1.31 eV (946 nm). It is associated with a  $S = 1$  ground state [?]. The second state is the negatively charged state  $\text{SiV}^-$  where the silicon-vacancy center recruited an additional free electron. It exhibits a zero-phonon transition at 1.68 eV (738 nm). Its ground state has been determined as a  $S = \frac{1}{2}$  state [?, ?]. Due to its outstanding brightness and the location of the zero-phonon-line in the visible range of the spectrum, this thesis focuses on the negatively charged SiV center.

For convenience we drop the charge distinction from now on and refer to  $\text{SiV}^-$  centers simply as SiV centers.

SiV centers have been synthesized using CVD in nanodiamonds and single-crystal diamond films [?], see chapter 4 for details. It is also possible to directly implant silicon atoms into pure diamond. High temperature annealing must then be used to animate present lattice vacancies to recombine with silicon impurities in order to form split-vacancy SiV centers [?, ?].

In the following sections we detail the most important luminescence properties of SiV centers in diamond. For a comprehensive review we refer to [?, ?] and references therein.

### 2.3.1 Luminescence properties

The silicon-vacancy center as a quasi-atomic system is capable of absorbing and emitting light. When a ground state electron absorbs a photon of appropriate energy, it is promoted to a discrete higher-energy excited state located within the band gap of the diamond host matrix. Reversing this excitation relaxes the electron back down to the ground state while emitting a so-called fluorescent photon, accounting for the energy difference between excited and ground state. This transition is “spin-allowed”, limiting the life-times of excited states to nano-seconds and thus promoting rapid relaxation and associated fluorescence [?].

Fluorescence is directly linked to the electronic structure of the SiV center, see Figure 2.4. It follows that photoluminescence spectroscopy can be used to study it using a laser to optically excite the SiV center. In the context of this thesis, optical above-resonant excitation is the method of choice, in particular, when used in conjunction with a confocal photoluminescence setup which will be discussed in chapter 3. If the excitation energy exceeds the energy of the lowest excited state, electrons are promoted to higher electronic and vibrational states. Conveniently, these states relax rapidly towards the lowest excited state in non-radiative processes [?]. Once the lowest excited state is reached, a fluorescent transition to one of the ground state levels can follow. It has been shown that above-resonant excitation is feasible for excitation energies ranging from 1.75 eV to 2.55 eV [?, ?, ?]. If the excitation energy is chosen too high, however, the SiV center is ionized. This is unfavorable, since electrons escaping to the diamond conduction band do no longer participate in fluorescence. Ionization may be reversed if a positively charged SiV center manages to capture a free electron from the conduction band. This charge state conversion is believed to be linked to fluorescence intermittence, describing “blinking” SiV centers [?, ?].

The fluorescence spectrum of SiV centers typically show two prominent features: A narrow zero-phonon-line a broad phonon side band. The former is connected to fluorescent photons associated with a purely electronic transition while the latter involves vibrational transitions involving electron-phonon interactions. The phonon side band is typically shifted to higher wavelengths with respect to the zero-phonon-line. The resulting energy deficit can be explained by phonons being created during the relaxation

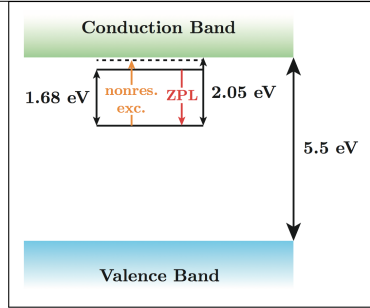


Figure 2.4: Simplified picture of the generous 5.5 eV band gap of diamond with discrete states induced by the presence of SiV centers. The SiV center ground state is situated 2.05 eV below the diamond conduction band. The lowest excited state sits 1.68 eV above the ground state with the zero-phonon-line transition in red connecting the two. Above-resonant optical excitation is indicated in orange. Figure courtesy of [?].

of higher vibrational states. A shift in the opposite direction can also be observed in rare cases if preexisting phonons are absorbed during the relaxation process [?].

The relative strength of the zero-phonon-line and the phonon side band is connected to the electron-phonon coupling of the excited color center and thus to lattice vibrations. When a color center is excited, its charge distribution changes. As a result, the equilibrium positions of all particles involved in the color center shift leading to slight changes in color center geometry. Naturally, the combined changes of charge distribution and geometry of the color center also affect the positions of surrounding atoms of the host lattice. Similarly, if the excited state relaxes back to the ground state, the process occurs in reverse. Thus, due to differing atomic arrangements for ground and excited states, the periodic emission and absorption of photons is accompanied by lattice vibrations, i.e. phonons. In other words, the electron-phonon interaction couples the motion of the lattice and electronic transitions of a color center [?, ?].

The Huang-Rhys model allows us to discuss the electron-phonon interaction in SiV centers in more detail. Our discussion follows the presentation in [?]. The model assumes in its simplest form that vibrational modes can be viewed as oscillations of nuclei between their equilibrium coordinates  $q$  associated with the electronic states [?]. Let  $\mathcal{K}_{3A_2}(q)$  and  $\mathcal{K}_{3E}(q)$  denote the harmonic potentials of the ground and excited states respectively:

$$\mathcal{K}_{3A_2}(q) = \frac{1}{2}\Omega^2 q^2 \quad (2.1)$$

$$\mathcal{K}_{3E}(q) = C_{3E} + aq + \frac{1}{2}(\Omega^2 + b)q^2 \quad (2.2)$$

$$= C_{3E} - C_R + \frac{1}{2}(\Omega^2 + b)(q - \delta q)^2. \quad (2.3)$$

It follows that the vibrational modes of ground and excited states are given as harmonic states with discrete energies  $\hbar\Omega(\nu + 2)$  as well as  $\hbar\sqrt{\Omega + b}(\nu + 2)$  respectively, where

$\nu$  denotes the occupation number and  $\Omega$  the frequency. Further, let  $aq$  denote the linear nuclear displacement of the excited state configuration with respect to the ground state equilibrium where  $q = 0$  holds. The quadratic term  $bq^2$  refers to the vibrational frequency shift due to a redistribution of charge between the electronic states. Given the linear and quadratic electron-phonon coupling strengths  $a$  and  $b$ , the equilibrium displacement of the  ${}^3E$  state can be obtained as:

$$\delta q = \frac{-a}{\Omega^2 + b}, \quad (2.4)$$

while the relaxation energy reads [?]:

$$C_R = \frac{a^2}{2(\Omega^2 + b)} = \hbar S \sqrt{\Omega + b}, \quad (2.5)$$

where  $S$  is referred to as Huang-Rhys factor.

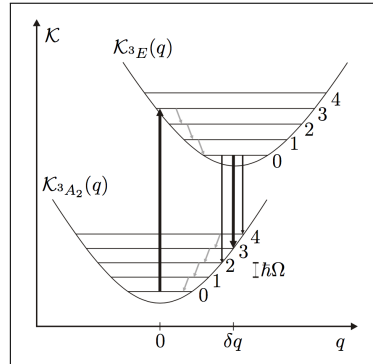


Figure 2.5: Huang-Rhys model of the vibrational transitions in the Frank-Condon picture: The excited state  $\mathcal{K}_{^3E}(q)$  is shifted by  $\delta q$  with respect to the ground state potential  $\mathcal{K}_{^3A_2}(q)$ . The recombination originating at  $\delta q$  marks the most probable transition (thick black arrow) from the fundamental  ${}^3E$  vibrational level to one of the vibrational levels of the  ${}^3A_2$  ground state followed by non-radiative transitions to the equilibrium position  $q = 0$ . The number of vibrational quanta involved in an optical transition are determined by the Huang-Rhys factor  $S$ . The excitation reverses the process. Optical transitions occur between states with identical values of  $q$  and are shown as vertical black arrows. Non-radiative transitions change the value of  $q$  and are shown as angled gray arrows. Figure and caption reproduced with permission [?].

To reason about the probabilities of various transitions between different vibrational levels associated with ground and excited states, the Franck-Condon principle can be applied [?, ?]. It states that transitions between electronic states become more probable if origin and destination states have vibrational levels with similar energy. This implies that the most probable transitions occur between states requiring no change of nuclei positions. Figure 2.5 illustrates the application of the principle for the Huang-Rhys model.

We find that the most probable optical relaxation from an  $^3E$  excited state back to an  $^3A_2$  ground state originates from the fundamental vibrational  $^3E$  state, i.e. the lowest-energy excited state. This state is shifted by  $\delta q$  with respect to the ground state, indicating that the energetically optimal nuclei positions differ from their ground state equilibrium positions. The most probable destination for the electronic relaxation process is a higher vibrational level of the  $^3A_2$  ground state with similar nuclei positions. From there, electron-phonon interactions continue the relaxation process down to the fundamental vibrational level of the ground state. This non-radiative process allows nuclei to return to their original ground state equilibrium positions. The process of exciting the system from the ground state, proceeds in reverse. The most probable optical excitation promotes an electron from the fundamental  $^3A_2$  ground state to a higher vibrational level of the  $^3E$  excited state. The optical transition is such that nuclei positions do not change. Note that optical transitions are faster than vibrational transitions since they do not require a change in positions of massive nuclei. Once in the higher vibrational excited state, electron-phonon interactions mediate a transition down to the fundamental  $^3E$  excited state with an associated change in nuclei positions. From there the relaxation-excitation cycle and its induced periodic changes in nuclei positions repeats.

As discussed, transitions involving phonons mostly originate from the fundamental vibrational level of excited electronic states and end in higher vibrational states of the electronic ground state. Photons emitted during the relaxation process are associated with the phonon side band of the SiV center. The observed red-shift of the phonon side band is directly tied to the phonon energy with higher order sidebands showing multiples of this energy. Note that the Huang-Rhys factor  $S$  can be interpreted as an indicator of the most probable optical transition involving photons. Thus, it can be used to quantify the strength of the electron-phonon interactions in SiV centers. A small value of  $S$  indicates a weak electron-phonon coupling resulting in negligible phonon side band emissions. If no phonons are involved, the entire emission is concentrated in the zero-phonon-line. Conversely, a large value of  $S$  indicates extensive electron-phonon interactions, leading to a pronounced phonon side band and a weaker zero-phonon-line. This dependence is naturally described by

$$e^{-S} = \frac{I_{ZPL}}{I_{ZPL} + I_{PSB}}. \quad (2.6)$$

For SiV centers hosted in polycrystalline diamonds the Huang-Rhys factors have been determined to be very small ranging from 0.08 to 0.24 [?, ?, ?]. As a result the zero-phonon-line as the most probable transition dominates the luminescence spectrum making SiV centers excellent narrow-band emitters. Figure 2.6 illustrates the stark difference between the zero-phonon-line and the phonon side band. In contrast,  $S = 3.74$  has been established for nitrogen vacancy centers [?]. A electron-phonon coupling of this magnitude concentrates almost all emission into the phonon side band and leaves the zero-phonon-line almost undetectable.

As an alternative measure for the electron-phonon coupling the Debeye-Waller factor

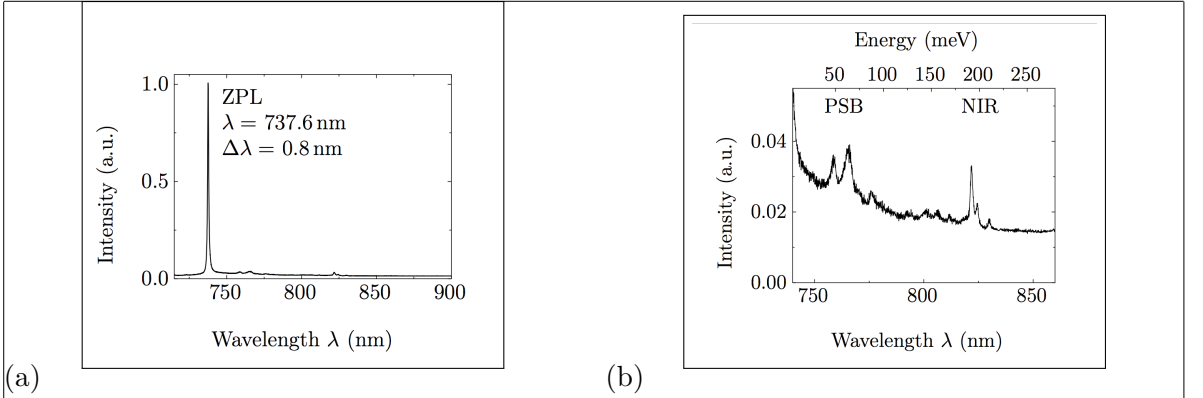


Figure 2.6: (a) The narrow zero-phonon-line dominates the luminescence spectrum. (b) Low intensity phonon side band shows distinct vibrational transitions. Figure reproduced with permission [?].

can be used. It is closely related to the Huang-Rhys factor  $S$  and defined as

$$D_w = e^{-S} = \frac{I_{ZPL}}{I_{ZPL} + I_{PSB}}, \quad (2.7)$$

which can be interpreted as the fraction of total photons that are emitted into the zero-phonon-line.

We remark at this point, that our discussion based on the Huang-Rhys model assumes that only one vibrational mode couples to the color center which is a strong assumption. In general it is believed that in a solid state host matrix a discrimination between the modes of the undisturbed lattice and quasi-local impurity-induced modes is appropriate [?, ?, ?]. Furthermore, various mechanical properties such as stress in the lattice are reported to affect phonon energies [?]. In addition, electron-phonon interactions and thus phonon side band features are believed to depend strongly on various local properties of color centers [?, ?]. Thus it is possible to encounter complex varying phonon side band features from one SiV center to the next. For a more detailed discussion of these effects we refer the reader to [?, ?] and references therein.

We close this chapter with a short discussion of the luminescence spectra of SiV centers at cryogenic temperatures. Naturally as temperatures approach absolute-zero the phonon side band must disappear since phonon creation ceases. If SiV centers are cooled below  $\approx 110 \text{ K}$  a fine structure is revealed [?]. It includes up to 12 different lines with intensities proportional to the natural abundance of the three stable isotopes of silicon  $^{28}\text{Si}$ ,  $^{29}\text{Si}$ ,  $^{30}\text{Si}$  [?]. Each isotope is associated with 4 lines attributed to doublet levels of ground and excited states which are split by 0.2 meV and 1.07 meV respectively [?, ?, ?]. The splitting itself is believed to be a result of spin-orbit coupling with a weak contribution of the dynamic Jahn-Teller effect [?]. Initial results were based on ensembles of SiV centers, however, recently the splitting was detected for isolated SiV centers as well [?]. Figure 2.7 shows exemplary spectra representative for ensembles and single

SiV center at cryogenic temperatures.

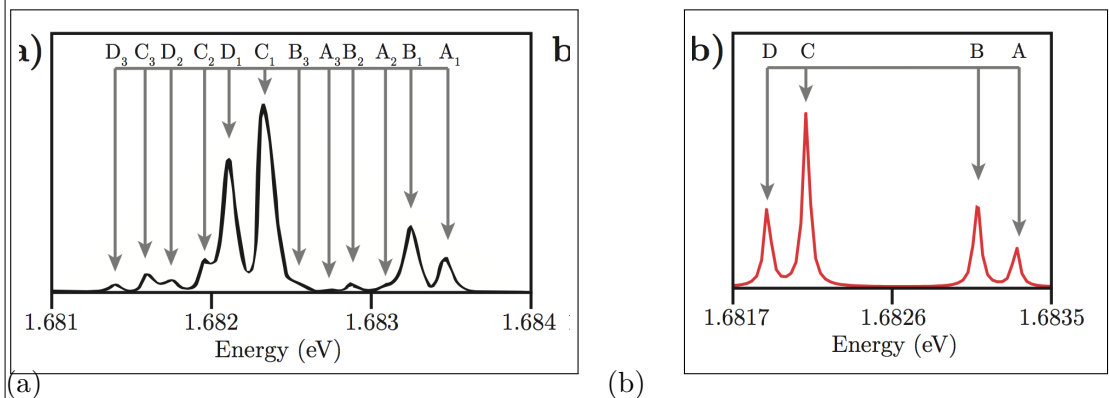


Figure 2.7: (a) Fluorescence spectrum of an ensemble of SiV centers at 10 K. 12 peaks can be seen, 4 for each stable isotope of silicon [?]. (b) Fluorescence spectrum of an isolated SiV center at 15 K. 4 peaks can be seen, 2 for the ground state and 2 for the excited state. Figure reproduced from [?].

---

---

# Chapter 3

## Photoluminescence Setup

### Remark:

Fill in missing values described as todos.

The study and handling of SiV centers in nanodiamonds requires dedicated experimental methods and techniques. In the following we detail the experimental setup used to obtain the results presented in later chapters. The core of the setup consists of a confocal microscope connected to either a grating spectrometer or a Hanbury Brown and Twiss interferometer. The former yields fluorescent spectra of SiV centers while the latter enables measurements of the intensity autocorrelation function of individual emitted fluorescent photons.

### 3.1 Confocal Setup

When studying SiV centers experimentally, two capabilities are key: Exciting SiV centers into emitting fluorescent light using a laser and the ability to register resulting SiV center fluorescence. A confocal setup elegantly supports both requirements. Confocal microscopy uses an objective to focus a laser onto a small volume of a sample which can be used to excite SiV centers in a controlled fashion. As the luminescence light returning from the emitter is in the same focus as the excitation laser light, it is effectively collected by the objective, thus the designation “confocal”. For an overview of confocal microscopy we refer the reader to [?].

Figure 3.1 illustrates the confocal setup deployed in this work. With the exception of the laser and the sample stage, the whole setup is fixed to a vertical breadboard. The vertical design permits a horizontal sample stage, promoting quick scanning and exchanging of samples. The sample itself resides on top of a translation stage and is held in place sufficiently by surface friction. It is oriented by an aluminum angle adjustable via a manual rotation stage. The translation stage is moved by two stepper motors (Newport MVP25XL) enabling the sample to be translated horizontally, i.e. in

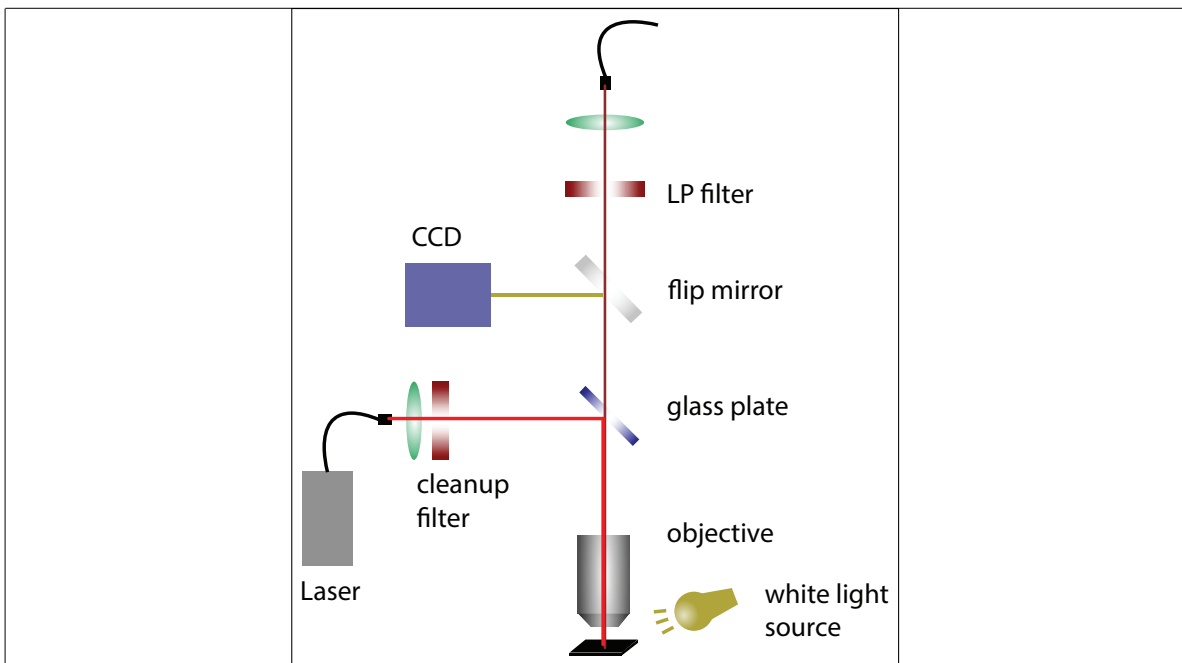


Figure 3.1: Confocal microscopy setup. An excitation laser beam (red) leaves an optical fiber and is directed towards a glass plate. The glass plate reflects  $\approx 10\%$  of the incoming beam towards an objective after which is focused onto the sample. The same objective collects the resulting fluorescent light and redirects it towards the glass plate where  $\approx 90\%$  of the light is allowed to pass. The passing fluorescence light is fed into an optical fiber which connects to the detection part of the setup. A flip mirror can be engaged to bring a CCD camera into the setup in case a white light source is used to illuminate the sample.

the  $x - y$  plane. Above the horizontal stage, the objective is fixed to another stage which in turn is mounted to a vertical breadboard. In this way, the vertical distance between the sample and the objective can be controlled. As a result the focus of the laser can be adjusted along the  $z$  axis, i.e. the optical axis, allowing to implement a full three-axis scan of samples.

The bright red color in the sketch in Figure 3.1 represents the path of the excitation laser beam. The sample is excited with a continuous wave diode laser (Schäfter-Kirchhoff, 58FCM) emitting at a wavelength of 660 nm. The outlet of the laser is a pigtail fiber. The laser light is out-coupled and collimated by an aspheric lens. To suppress sideband emission from the laser, a 660 nm bandpass filter with a filter window of 10 nm is used. After this cleanup filter, the excitation beam hits a mm glass plate (fabricator Halle Germany ) redirecting the beam. It is then focused onto the sample by a  $100\times$  microscope objective (Olympus, LMPPlanFLN) with a numerical aperture of 0.8.

The collected light follows the detection beam path depicted in dark red in Figure 3.1. Both the excitation light reflected from the sample surface and the fluorescence light from the color centers pass through the glass plate. Removing the flip mirror behind

the beamsplitter from the path directs light towards a single mode fiber (Thorlabs SM600) connecting the confocal setup with either the spectrometer or the HBT setup. Prior to focusing light into the single mode fiber using an aspheric lens, a long-pass filter is deployed to eliminate residual excitation light and ambient light. The filter is chosen with a cutoff wavelength of 710 nm or 720 nm. Besides the obvious purpose of guiding the photoluminescence light to the spectrometer and the Hanbury Brown and Twiss setup for spectroscopic investigations, it severs another crucial purpose. Namely, diameter of about  $4.3\text{ }\mu\text{m}$  acts as a pinhole to reject photoluminescence light from depths outside of the focal plane [?]. For this axis the resolution amounts to , in the plane of the sample it is .

We remark that the glass plate in used Figure 3.1 has a high transmission of  $\approx 90\%$ . This leads to a high collection efficiency of fluorescence light at the cost of excitation efficiency since most of the exciting light is not being redirected towards the sample. In contrast to that, certain use cases such as saturation measurements require high excitation intensities. To realize these the glass plate may be replaced by a dichroic mirror (DRLP692). A dichroic mirror spectrally separates excitation light from photoluminescence light as it selectively transmits and reflects light as a function of its wavelength.

In general, if high excitation setting is required we opt for a dichroic mirror, otherwise working with the glass plate at lower excitation is the default. This is advised since high intensities carry the danger of damaging SiV centers to the point of bleaching and can also cause fluorescent intermittence of SiV centers, i.e. blinking, as an unwanted side-effect see ??.

## 3.2 Optical Imaging of The Sample Surface

The setup introduced in the previous section can be modified to investigate the sample surface before starting fluorescence measurements. For this purpose, the sample is directly illuminated at a flat angle from outside the objective with white light from a halogen lamp, see the white light source in Figure 3.1. The flip mirror behind the glass plate is brought into an upright position to guide the light towards a CCD camera. The scattered light from the sample surface is collected by the objective and the surface is imaged on the CCD chip. Thus nanodiamonds and other features on the substrate are made visible. The resolution of this configuration of the setup is limited by .

In chapter chapter 7 we introduce applications of SiV centers in nanodiamonds, for which knowing the precise positions of specific nanodiamonds is crucial. Therefore, cross markers are milled into the surface of the substrate on which the nanodiamonds are situated. These markers of a size of  $10\text{ }\mu\text{m}$  can easily be recognized by optical imaging and can thus be used as landmarks for the purpose of indexing individual SiV centers. The starting point for a scan of an area of interest on the sample is fixed while navigating with the optical image. After flipping the flip mirror, light is directed towards the detection part of the setup enabling systematic scans of the sample.

resolution value

resolution value

optical diffraction, shadows

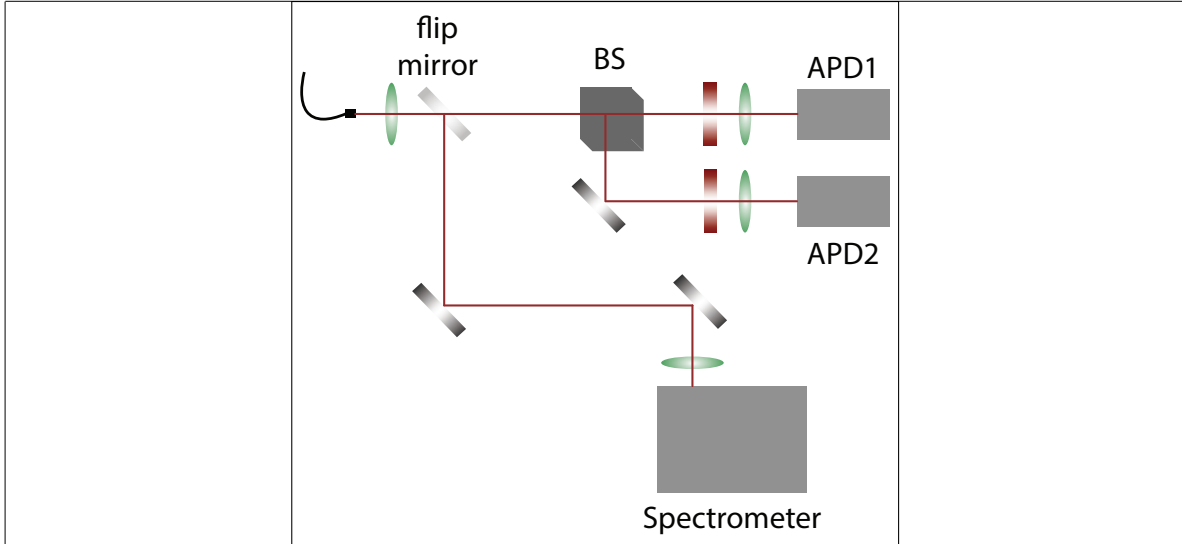


Figure 3.2: Spectrometer and HBT interferometer. Fluorescent light arrives via an optical fiber and is directed towards a flip mirror. The mirror directs the beam either towards a 50:50 beam splitter (BS) into the APDs of the HBT setup, or into a grating spectrometer.

### 3.3 Spectrometer

Figure 3.2 displays the detection part of the setup. The fluorescence light arrives via a pigtail fiber connecting the confocal setup with the detection setup and is out-coupled with an aspheric lens. A flip mirror is employed to direct the light either to a grating spectrometer or the HBT setup. The optical spectrum of a light source gives insight to the optically active constituents and therefore bears information about the emitter.

As mentioned before, the fluorescence light from the SiV centers is investigated with the grating spectrometer (Princeton Instruments Acton2500i). The incident beam passes through an entrance slit, is then scattered on the grating where the light is spectrally divided and finally hits a detector, imaging the entrance slit on the detector surface. The employed detector is a CCD camera (Princeton Instruments, Spec-10) cooled with liquid nitrogen to a temperature of  $-120^{\circ}\text{C}$ . This limits background signals due to thermally generated free charge carriers. The spectrometer is optimized for detection of light up to a wavelength of 900 nm. and features three gratings: 600 grooves/mm, 1200 grooves/mm, and 1800 grooves/mm. These gratings are mounted on a turret, allowing easy swapping of gratings between measurements.

With the spectrometer's step-and-glue function which is implemented in the spectrometer software (WinSpec) it is possible, to record several spectra over a wide wavelength range which are then stitched together. It is therefore possible to combine a larger wavelength range with a higher resolution. For most measurements the grating with 600 grooves/mm was used. The resolution of the spectrometer using the 600 grooves  $\text{mm}^{-1}$  is 0.13 nm at 738 nm and the accuracy amounts to  $\pm 0.4$  as stated

by the manufacturer. This resolution suffices for the measurements presented in this work.

### 3.4 Hanbury Brown and Twiss Setup

A Hanbury Brown and Twiss setup is used to establish the intensity autocorrelation function ( $g^{(2)}$  function) of an emitter [?, ?]. In this work, the  $g^{(2)}$  function is used to assert the non-classical behavior of a photoluminescence source, i.e. characterize its behavior as a single photon emitter. In the photon number representation, it is defined as follows:

$$g^{(2)}(\tau) = \frac{\langle N(t)N(t + \tau) \rangle}{\langle N(t) \rangle^2}. \quad (3.1)$$

Here,  $N(t)$  denotes the number of photons at a certain time  $t$ ,  $N(t + \tau)$  denotes the number of photon at a time interval  $\tau$  later than  $t$ . The angular brackets  $\langle \rangle$  denote temporal averaging. For a two-level system  $g^{(2)}(\tau)$  can be interpreted as the probability of detecting two photons separated by a time interval  $\tau$ . The physical intuition behind this definition is as follows: The detection of a fluorescent photon emitted from a quantum system is the result of an excited electron relaxing back to its ground state. To emit a consecutive single photon, an additional electron must first be promoted to an excited state, a process which takes a certain amount of time, see ?. If  $g^{(2)}(\tau) \neq 0$  in the limit of  $\tau \rightarrow 0$  a system is capable of emitting several photons simultaneously. This is known as photon bunching and is typical for classical light sources. In contrast,  $g^{(2)}(\tau) \rightarrow 0$  for  $\tau \rightarrow 0$  is an indication that no two photons can be detected simultaneously. This property is termed photon anti-bunching and is a defining characteristic of non-classical light sources such as single photon source. The last important type are coherent photons, as for instance produced via stimulated emission. Figure 3.3 shows how the  $g^{(2)}$  function distinguishes these three types. For an in-depth review of the intensity auto-correlation function we refer the reader to [?, ?].

The aim of the HBT setup is to record the time delay between two consecutive photons as a prerequisite to compute  $g^{(2)}(0)$ . A sketch of the HBT setup is shown in Figure 3.2. Photons are detected using single photon avalanche photo diodes (APDs, PicoQuant  $\tau$ -SPAD100). APDs are the semiconductor analog to photomultiplier tubes, i.e. an incoming photon creates secondary charge carriers through ionization. The secondary charge carrier is accelerated by a bias voltage to create further secondary charge carriers, resulting in an avalanche effect. Therefore, the signal of a single photon is intensified and detected as an electrical current pulse. These avalanche photo diodes have a nominal detection efficiency of up to 70 % at an optimal wavelength of about 670 nm and a dark count rate of under 100 cps. If a charge carrier created by the avalanche is temporarily trapped and later liberated, it induces a so-called after-pulse. To avoid detecting these artifacts as real events, the APDs have a dead time of about 70 ns.

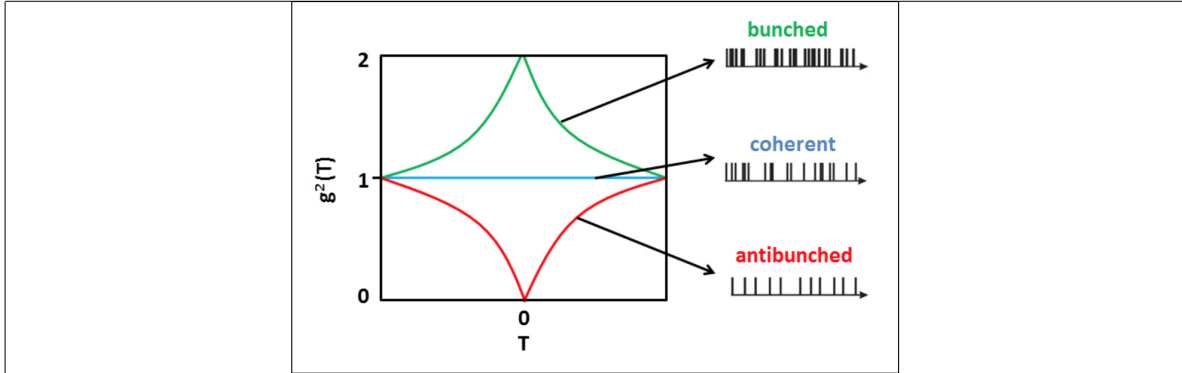


Figure 3.3: Intensity autocorrelation function for coherent, bunched, and anti-bunched light sources. Figure and caption reproduced from [?].

In the ideal case, one APD would be enough to measure the time delay between two consecutive photons. However, the second of two consecutive photons could hit the detector during its dead time. To circumvent this problem, two APDs are employed and the detection beam is split with a non-polarizing 50:50 beamsplitter cube. Each beam then goes through a band-pass filter and is focused on the avalanche photo diode with an aspheric lens. As the beam path is slightly different for each APD, a small optical path difference is introduced, however, this difference only results in an offset of the  $g^{(2)}$  function and does not alter the physical nature of the result. The bandpass filters serve two purposes: First, they limit optical crosstalk between the avalanche photo diodes. The detection process in an avalanche photo diode produces light due to recombination of charge carriers. Crosstalk between two avalanche photo diodes occurs, if one of the photons produced by recombination in one avalanche photo diode escapes and is detected in the other one [?]. Second, the band-pass filters serve to reduce background during the  $g^{(2)}$  measurement process or to spectrally separate emission from several emitters. Therefore, it is possible to find single emitters, which are not spatially separated enough to be separated by the spatial resolution of the setup. In particular, emitters can be individually investigated if their ZPLs exhibit wavelengths which are spectrally well separated. Band-pass filters suited for the respective wavelengths are used to selectively investigate light associated with distinct ZPLs.

When the APD fires, it outputs a digital TTL (transistor-transistor logic compatible) signal. The arrival times of the signals, so-called time-tags, are recorded with a time-tag unit (produced by dotfast-consulting) with a temporal resolution of 78.125 ps. The timing uncertainty of the photon detection process introduces variations of the digital signal's time-tag from the actual detection time. This is called timing jitter and adversely affects the recorded time-tags and consequently the value of  $g^{(2)}(0)$ . In the past it has been shown to significantly obfuscate the detection of anti-bunching behavior in single photon source and thus relevant corrections need to be taken into account [?, ?]. As stated earlier, the time delay between two consecutive photons is necessary for the reconstruction of the  $g^{(2)}$  function. The time delays are fed into a histogram which is then fitted to receive the continuous  $g^{(2)}$  function. As a suitable fit function a numerical convolution between the  $g^{(2)}(\tau)$  derived for a three-level system and detector timing

jitter can be used [?, ?, ?].

In the Hanbury Brown and Twiss-setup the arrival time of photons are recorded with two APDs, each of which keeping a list of arrival times as raw data. To get a single array of arrival times of the photons, which can then be binned to obtain the  $g^{(2)}$  function, the arrays of time-tags of the two APDs have to be correlated. For that, the time difference between each entry in one array and all consecutive time-tags in the other array are determined and binned according to the timing resolution of the time-tag unit. After normalizing and fitting these data,  $g^{(2)}(0)$  can be obtained determining whether a emitter characterizes as a single photon source.

---

---

## Chapter 4

# Fabrication of Nanodiamonds

### Remark:

die section mit den silicon implanted nanodiamonds muss von dir ueberarbeitet werden. Die hab ich deshalb vorerst ausgelassen. Es gibt 3 teile (einfuehrung, preliminary tests und final procedure). Ich hab den eindruck, dass sich da konzeptionell vieles wiederholt und das man das ganze vielleicht in einer section unterbringen kann und die feineren unterscheidungen einfach beilaeufig erwaehnt.

section iridium substrate sollte auch nochmal durchgelesen werden. Ich habt zwar nochmal ueberarbeitet, aber ich denke da koenntest du noch den einen oder anderen erklaerendne statz springen lassen. Insbesondere das listin in preparation of substrate ist nicht gerade selbsterklaerend.

Die tabelle mit dem ueberblick ueber alle samples hab ich in eine eigene section geschoben. Die is ja wichtig, weil in den results immer wieder die sample id genannt werden. Wennd as im inhaltsverzeichnis auscheint, find ich das praktisch.

“Diamond forms under high temperature and pressure conditions that exist only about 100 miles beneath the earth’s surface.”

Gemological Institute of America Inc.

Due to its extraordinary properties, diamond has transcended its sole purpose as a rare gem and developed into an important tool enabling various applications in industry and research. This change has been driven largely by the development of methods allowing to cheaply produce synthetic diamond. While synthetic diamonds are typically small and without the splendeur generally associated with diamond, they can be produced on-demand and are thus arguably more useful than rare gemstones. In this chapter we introduce the two most common methods for the fabrication of diamonds in a laboratory setting: The high-pressure, high-temperature and the chemical vapor deposition method. The aptly named high-pressure, high-temperature (HPHT) process mimics the conditions under which diamond is formed in nature and is widely used to synthetically produce diamonds for industrial applications such as utilization of diamond as a abrasive. While HPHT diamonds are utilized in this work, most reported measurements are

based on diamond produced with the CVD method in which diamonds are grown using a hydrocarbon gas mixture. Both processes have in common that defects and impurities are naturally occurring. For a more extensive list of diamond production processes refer to [?]. In the context of this thesis nano-sized diamonds are required. They can be obtained by milling larger sized HPHT or CVD diamonds down to the desired grain size in a vibrational mill. The obtained nanodiamonds are small enough that individual specimen have a chance of hosting a singleton SiV center. These can be identified and used for further exploration.

## 4.1 High-Pressure High-Temperature Diamond

The HPHT method was the first process to successfully synthesize diamond in 1879. Today, it is still widely used due to its relatively cheap production costs for small diamonds [?].

In the HPHT process, diamond is synthesized from graphite under temperatures of up to  $1.5 \times 10^3$  °C pressures between  $5 \times 10^4$  bar and  $10^6$  bar [?]. Under these extreme conditions, carbon transitions from its graphite to its diamond phase because the latter becomes energetically favorable [?, ?, ?, ?]. The machine used for this kind of synthesis is a press. For some forms of this method, a metallic catalyst solvent is added lowering the required pressures and temperatures by causing graphite to dissolve earlier. At the same time the catalyst promotes the crystallisation process. Several press designs exist, all of which relying on creating and maintaining high pressures and a high temperatures. While it is possible to grow big ( $> 10$  carat) high-quality diamonds with the HPHT process, its cost quickly increases and thus becomes unfavorable.

In this thesis, HPHT nanodiamonds produced by Davydov et al. [?] are spectroscopically investigated.

## 4.2 Chemical Vapor Deposition Diamond

In contrast to the HPHT method, diamond is crystallized from carbon available in the gas phase in the CVD method. The process still requires respectable temperatures in the range of 700 °C to 1300 °C but makes due with the low pressures of less than 1 bar available in a vacuum growth chamber [?].

The chamber contains a vapour consisting of a mixture of atomic hydrogen and methane. The gas can be forced into the plasma phase using strong microwaves or hot filaments [?, ?, ?]. While the hot filament is easy to implement, it has the disadvantage that atoms which are etched from the filament during the growth process are likely to contaminate the diamond. To minimize the introduction of defects other than SiV centers in the diamond, growing diamonds in a microwave plasma is preferred. In it methane molecules dissociate and release carbon. In the presence of a substrate such as iridium containing suitable seeds, carbon can crystalize forming diamond. Figure 4.1 illustrates

the setup. In a plasma containing atomic hydrogen, the formation of diamond is favored over the formation of graphite. This is due to the fact that the atomic hydrogen preferentially etches  $sp^2$  bonded carbon, i.e. graphite.

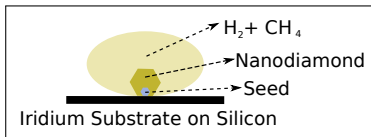


Figure 4.1: Sketch of the CVD method. A hydrogen-carbon plasma acts as a donor for carbon atoms which may crystallize to form diamond ontop of a suitable iridium substrate. An initial diamond seed facilitates the process.

Typically, single crystal diamond substrates are required to grow single crystal diamond. HPHT substrates are suitable to start a crystalization process. This approach is referred to as homoepitaxial growth. An alternative approach is to utilize non-diamond substrates such as iridium or platinum to trigger heteroepitaxial growth [?, ?]. This method is utilized for all the CVD nanodiamonds grown and investigated in this thesis. It relies on small diamond crystals deposited in the substracte acting as seeds for the diamond crystalization process. Seed diamond crystals are commercially available, and are usually particles produced by a so-called detonation process. In a detonation process, the high pressure produced by shockwaves of a detonation is used to create very small diamond particles of a size down to a few nanometers.

Growth on a substrate is favored, if the lattice constant of the substrate and the diamond to be grown are similar. The lattice constant of iridium is 0.384 nm [?, ?] and thus close to the lattice constant of diamond with 0.356 nm [?]. Therefore, we opted to grow diamond on a stratified substrate, consisting of iridium layers of 60 nm to 150 nm thickness. The iridium layers themselves were grown onto an yttria-stabilized zirconia (YSZ) buffer layer, which in turn was grown on a silicon wafer [?]. If the lattice constant of the substrate and the diamond are not matched, stress in the diamond lattice is induced. Therefore, the iridium substrate not only facilitates diamond growth, but also reduces unfavorable stress in the nanodiamonds. The detrimental effects of stress on the diamond lattice and its implications with respect to hosted SiV centers are briefly discussed in chapter 6.

To produce nanodiamonds of controlled size, the growth process is stopped when the diamonds grown onto the seed crystals are large enough. If the growth process is continued, the individual crystals grow together to form diamond films. Such diamond films are used as starting material for the wet-milling process described in section 4.3. One of the advantages of the CVD process is that silicon is incorporated automatically into diamonds, SiV centers can thus be formed *in-situ* as the diamond is grown. The presence of silicon atoms required to be absorbed into the diamond lattice is explained by the plasma etching the edges of the silicon waver underneath the growth substrate. To further increase the silicon content in the chamber, sacrificial silicon can be introduced.

After nanodiamond growth, the nanodiamonds are either investigated directly on the

growth substrate or transferred to an ultrasonic bath to obtain a solution which is coated onto other substrates for further exaporation.

In this thesis, two types of nanodiamonds samples were investigated. The first batch, henceforth referred to as CVD samples, was grown by the group of M. Schreck, Augsburg University using detonation diamond seeds of a size smaller than 3 nm (produced by the company Microdiamant, product Liquid Diamond monocrystalline, MSY 0-0.03 micron GAF). For the growth process, 1 % of methane was added to the hydrogen environment in the growth chamber. The growth process was performed with a pressure of 30 hPa for 30 min to 60 min, yielding nanodiamonds of a diameter of about 100 nm to 200 nm. A sample of the produced diamonds is given in Figure 4.2.

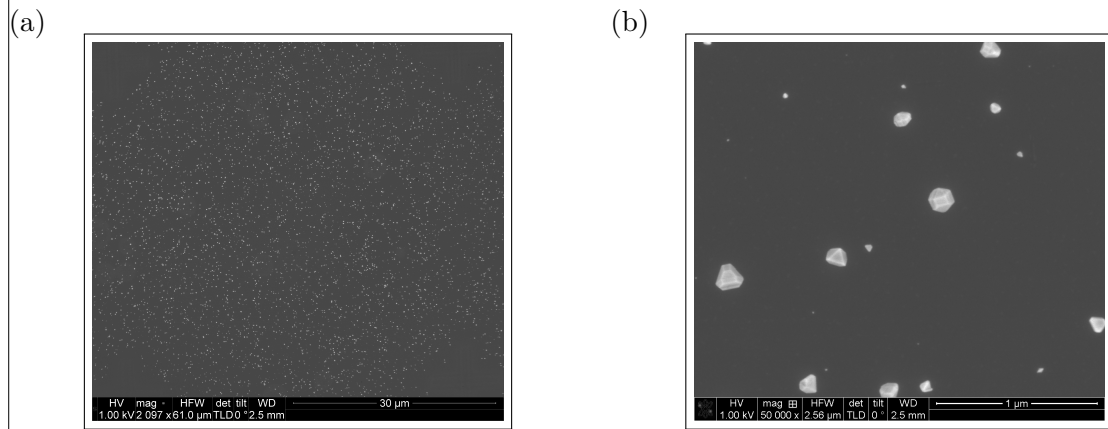


Figure 4.2: SEM images of CVD diamonds (sample insitu cvd) produced by M. Schreck's group at Augsburg University. The average size of these nanodiamonds is 100 nm. (a) Overview image, white dots are nanodiamonds. (b) Detail image, it can be seen that nanodiamond shape and size is varied.

The second type of samples consist of CVD nanodiamonds grown onto molecular analogs of diamond crystals. A subgroup of these molecular diamonds are called diamondoids and are carbon crystals based on the carbon cage molecule adamantane  $C_{10}H_{16}$ . The molecular diamonds used for this work are adamantane in cyclohexane, mercapto adamantane in cyclohexane, and cyclohexane. Each of these seed crystals was used in different growth processes. During the growth process, either 1 % or 3 % methane was added to the hydrogen plasma and either silicon (Si) or silicon dioxide ( $SiO_2$ ) was injected to promote the formation of *in-situ* incorporated SiV centers, see Table 4.1.

### 4.3 Wet-Milled Nanodiamonds

In addition to growing nanodiamonds of a specific size directly via a CVD process, macroscopic diamond starting material can be crushed to obtain small diamond particles. In contrast to nanodiamonds directly grown by a CVD process, the process is divided into two sub-processes: At first a macroscopic diamond is produced using one

Table 4.1: Summary of the samples grown on diamondoid seed crystals.

Sample name	Seed crystals	Methane conc.	Silicon source
160211_E	Mercapto adamentane in cyclohexane	1%	SiO <sub>2</sub>
160211_F	Cyclohexane	1%	SiO <sub>2</sub>
160212_C	Cyclohexane	3%	Si
160212_D	Adamentane in cyclohexane	3%	SiO <sub>2</sub>
160212_E	Mercapto adamentane in cyclohexane	3%	SiOs
160212_F	Cyclohexane	3%	SiO <sub>2</sub>

of the methods introduced in this chapter. Then macroscopic diamond is continuously milled into smaller diamond particles.

The wet-milled nanodiamonds investigated in this thesis were kindly provided by A. Muzha, group of A. Krueger, Julius-Maximilians Universität Würzburg. During the wet-milling process small metal beads in an aqueous solution are driven by the vibrations of a vibrational mill. The moving beads continuously collide with the present diamonds and thus keep breaking them into smaller and smaller particles. A sketch of the process is shown in ???. Steel contamination introduced by the beads can be eliminated in a post-processing treatment with acid.

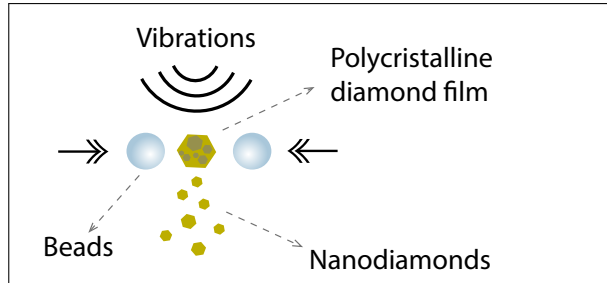


Figure 4.3: Sketch of a vibrational wet-mill. A macroscopic polycrystalline nanodiamond is progressively broken down into smaller polycrystalline nanodiamonds by metal beads.

The big advantage of the milling process is that it enables the production of a large quantity of diamond nanoparticles. When producing nanodiamonds directly via a CVD process, the number of produced nanodiamonds in one process scales with the surface of the substrate on which the nanodiamonds are grown. In contrast, the quantity of milled nanodiamonds scales with the volume of the starting material. Another advantage of the wet-milling process is that the nanodiamonds are already in an aqueous solution after milling. Therefore, it can be used to spin-coat the nanodiamonds directly onto any substrate. Samples created in this fashion can directly be used for further investigation and do not require additional processing.

If the starting material for the wet-milling process is a polycrystalline diamond film, it is likely to break along distinct crystal boundaries. However, due to imperfections

in the growth process, particles may break down such that progressively smaller milled diamond grain remain polycrystalline. As a result, the final nanodiamonds contain crystal boundaries themselves, indicative of reduced crystal quality. To improve diamond quality nanodiamonds are treated with post-processing steps including annealing in vacuum and oxidation in air. A detailed description of these processes and their effects is given in chapter 5.

In general any diamond, independent of production method, can be used as starting material for the milling process. In the following sections, available samples are distinguished by the respective starting material and milling method.

#### 4.3.1 Wet-Milled HPHT Nanodiamonds

We investigated nanodiamonds wet-milled from a HPHT starting material to median sizes of about 45 nm, 80 nm and 260 nm. They were then drop-cast onto an iridium substrate and implanted with  $^{28}\text{Si}^{1+}$ . The implantation itself was performed by D. Rogalla, Ruhr-Universität Bochum (RUBION - Zentrale Einrichtung für Ionenstrahlen und Radionuklide). All HPHT nanodiamonds were oxidized in air at 450 °C for 3 h. Resulting samples available for explorations are designated hphtimp45, hphtimp80, hphtimp260 and listed in Table 4.2.

Complete  
implan-  
tation  
parame-  
ters

#### 4.3.2 Wet-Milled CVD Nanodiamonds

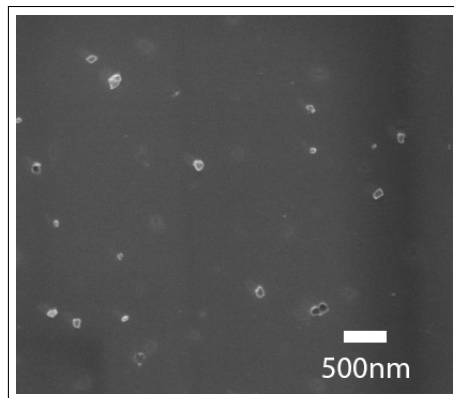


Figure 4.4: Pictures of milled nanodiamonds (sample insitu100) showing the distribution of the nanodiamond crystals on the iridium substrate.

In the following paragraphs, details of the production processes of nanodiamond produced by wet-milling a CVD diamond film in a vibrational mill are given. For an overview of the samples refer to Table 4.2. The starting material for the wet-milled nanodiamonds was a nanocrystalline diamond film [?] directly grown on a silicon wafer by CVD. A microwave hydrogen plasma containing 1 % methane was used to grow on purified 5 nm nanodiamond seeds (produced by PlasmaChem). To induce *in-situ* SiV

center creation, sacrificial Silicon pieces are placed in the growth chamber. During diamond growth the silicon pieces are etched by the plasma leading to individual atoms being incorporated into the diamond lattice. The diamond film is then wet-milled in a vibrational mill with steel beads. The high amount of steel containment due to the steel beads is removed by extensive acid treatment. We also investigated nanodiamonds milled with silicon nitride beads, and found that the choice of material of the beads does not result in any noticeable difference in dependent measurements. The median diameters of the diamonds are 50 nm, 70 nm and 100 nm as determined by laser diffraction spectroscopy. ?? shows milled nanodiamonds ontop of an iridium substrate. The aqueous solution containing the nanodiamonds is drop cast onto an iridium film on a Silicon substrate. The iridium film of a thickness of 130 nm is grown onto a buffer layer of yttria-stabilized zirconia (YSZ) which in turn is grown onto a Silicon wafer. The iridium surface has the advantage that it acts as an antenna and therefore enhances the collection efficiency of fluorescence light [?]. For a discussion on the properties of the substrate see section 4.4. Post-process treatment consist of annealing in vacuum at 900 °C or consecutive oxidation in air at a temperature of 450 °C, or a combination of the two. The duration for either treatment method was 3 h to 6 h.

### 4.3.3 Doubly Wet-Milled Implanted Nanodiamonds Implanted With Silicon

In addition to SiV centers that were implanted during diamond growth, we investigated nanodiamonds with SiV centers implanted after diamond growth. Here a polycrystalline Element Six diamond film (electronic grade) served as the starting material. In bulk material, the implantation causes the SiV centers to form in a specific depth dependent on the implantation energy, leaving most of the diamond vacant of SiV centers. As a consequence, a big portion of nanodiamonds milled from such a bulk material would not host any SiV centers. To obtain diamond particles with a homogeneous distribution of SiV centers, the process of fabricating implanted nanodiamonds is the following: First, the diamond film is milled to diamond particles a few microns in size. Next, these microdiamonds are spin-coated onto iridium substrates and implanted with  $^{28}\text{Si}^{1+}$ . To eliminate lattice damage and unnecessary vacancies resulting from the implantation process, diamonds were annealed in vacuum and subsequently oxidized. At last, the micrometer sized diamond particles are milled to the desired smaller sizes.

#### Preliminary Tests

The starting material was an Element Six electronic grade diamond film. The diamond was milled in a wet-milling process to sizes on the order of micrometers, which were then coated onto a silicon substrate. The microdiamonds were implanted with  $^{28}\text{Si}^{1+}$  at an implantation energy of 1.7 MeV, and fluences of  $10^9 \text{ cm}^{-2}$  to  $10^{12} \text{ cm}^{-2}$ . After im-

---

<sup>1</sup>Implantation performed by D. Rogalla, Ruhr-Universität Bochum (RUBION - Zentrale Einrichtung für Ionenstrahlen und Radionuklide).

plantation, the microdiamonds on the silicon substrate were annealed for 2 h at 900 °C and oxidized in air for another 2 h at 450 °C. However, we encountered the problem that the silicon sublimated and re-nucleated during annealing, causing the diamonds to sink into the silicon surface (Figure 4.5a). Iridium is less prone to damage by high temperatures and withstands annealing procedures up to our standard annealing temperature of 900 °C without problems. Therefore, we used a sample with microdiamonds on a silicon substrate which was not annealed to shake the nanodiamonds off the silicon substrate in an ultrasonic bath, and consecutively coated the microdiamonds on an iridium substrate. After annealing and oxidizing the nanodiamonds on the iridium substrate, the iridium surface was intact.

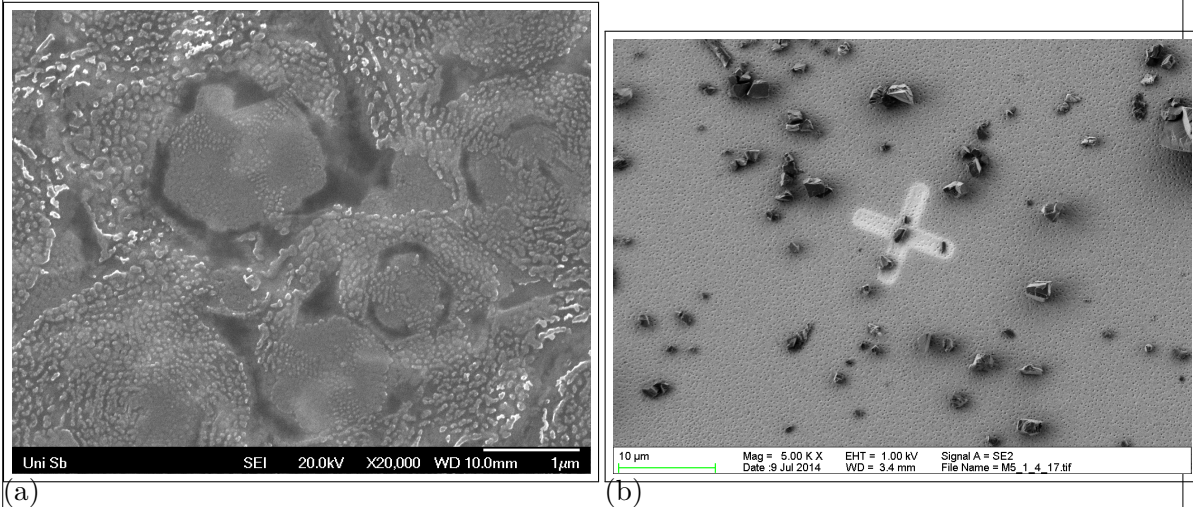


Figure 4.5: (a) SEM picture of nanodiamonds sunken into a silicon substrate after annealing at 900 °C for 3 h. Magnification 20 000. (b) SEM image of the microdiamonds after milling on an iridium substrate, but before implantation. In the middle of the picture, there is a reference cross milled into the iridium substrate with a focused ion beam. Its size amounts to 10 μm. It can be seen, that the microdiamonds exhibit sizes of a few micrometer.

## Final Procedure

For the milling process in a vibrational mill, a minimum amount of diamond material is necessary. When starting with a diamond film, this threshold is easily reached, however, a big quantity of microdiamonds is needed to meet the requirements. Therefore, production was carried out at a larger scale after the preliminary tests. The microdiamonds were directly spin-coated onto iridium substrates, implanted with  $^{28}\text{Si}^{1+}$  (implantation energy 900 keV, fluence  $10^{11} \text{ cm}^{-2}$ ) <sup>2</sup> The microdiamonds were then annealed in vacuum for 3 h at 900 °C and oxidized in air for 3 h at 450 °C. At last, they were milled again

how  
much?

<sup>2</sup>Implantation performed by J. Klug at rubitec - Gesellschaft für Innovation und Technologie der Ruhr-Universität Bochum mbH.

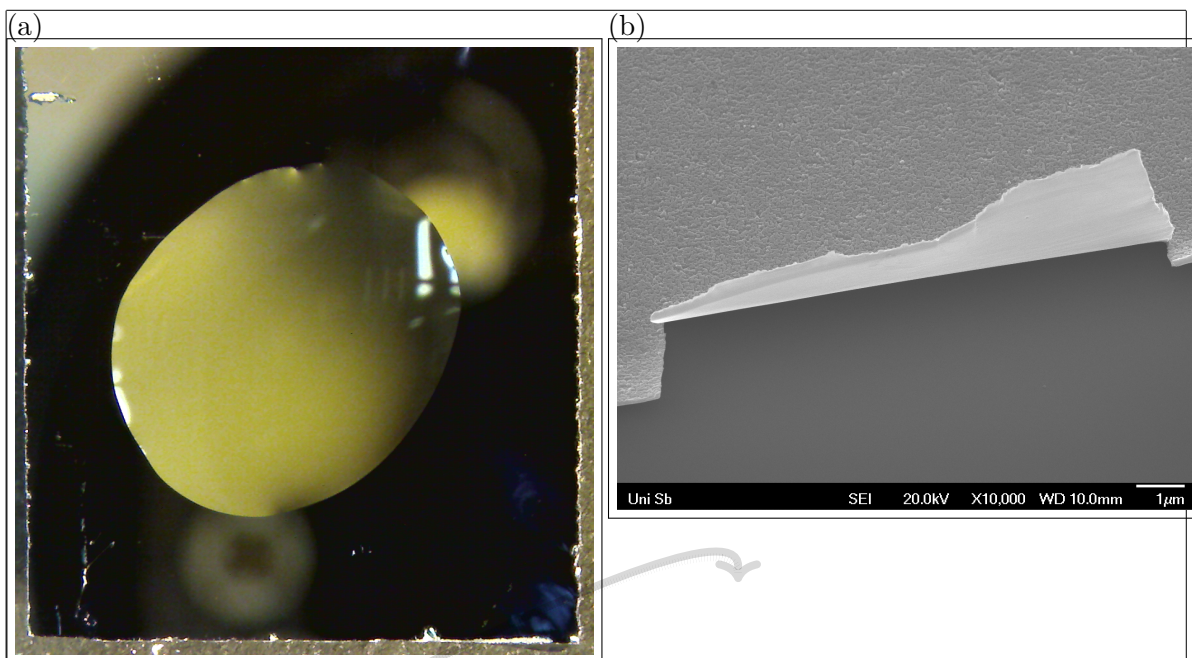


Figure 4.6: (a) Microscope image of a drop of water on an iridium substrate cleaned with Piranha etch. This picture was used to estimate the contact angle. (b) SEM picture of an 60 nm iridium layer that peeled off the substrate after an ultrasonic bath.

to sizes of about 40 nm, 45 nm, 240 nm and 260 nm. The diamonds of sizes 40 nm and 240 nm were annealed in vacuum at 1200 °C.

## 4.4 Iridium Substrate

As mentioned in section 4.2, we used a silicon substrate with an iridium layer on top for most experiments in order to match the lattice constants of substrate and diamond. We also use the same substrates for the experiments with wet-milled diamonds, as using iridium has several advantages:

- The high hydrophilicity of iridium enhances the homogeneity of the nanodiamonds on the substrate after spin-coating or drop-casting. The hydrophilicity is further improved by treating the substrate in a Piranha etch (50:50 mixture of sulfuric acid H<sub>2</sub>SO<sub>4</sub> and hydrogen peroxide H<sub>2</sub>O<sub>2</sub>) by removing oxide layers on the surface. The treatment with Piranha etch also has the advantage that all organic contamination is removed. Measurements after applying the Piranha cleaning yielded an estimation of the contact angle of slightly more than one degree. To determine the contact angle with water, the volume of a water drop is compared to the surface it covers after dropping it onto an iridium substrate, see Figure 4.6a. From that an estimation of the contact angle is deduced.
- During the post-processing steps, it is of major importance, that the substrate can

withstand high temperatures. As described in section 4.3.3, during the preliminary tests with implanted nanodiamonds on a silicon substrate we encountered difficulties with diamonds on a silicon substrate as the sunk into the surface after annealing. In contrast, iridium withstands the high temperatuers required for annealing without damage.

- Iridium acts both as a mirror and as an antenna for the fluorescence light light emitted by the SiV center [?]. Therefore, the collection efficiency of the fluorescence light light is enhanced.

At this point we comment upon a minor complication we experienced when using iridium surfaces. If the iridium layer is too thin, it tends to peel off the substrate, see Figure 4.6b. We encountered this problem during a cleaning procedure in the ultrasonic bath. However, this disadvantage is easily circumvented by using a thicker iridium layer. For our measurements, we used an iridium layer of a thickness of 130 nm, for which we did not encounter any adhesion problems.

#### **4.4.1 Preparation of The Substrate**

As a preparatory step preceeding drop-casitn, the iridium substrate is cleaned. The standard cleaning procedure is comprised of the following cleaning steps in an ultrasonic bath. Each step is in effect for a duration of 3 min to 7 min:

- Distilled water with a drop of dishwasher detergent
- Isopropanol (99.9 % p.a.)
- Acetone (99.9 % p.a.)
- Distilled water

Thereafter, the substrates are put into a Piranha solution (50 % sulfuric acid  $H_2So_4$ , 50 % hydrogen peroxide  $H_2O_2$ ) to enhance the surface hydrophilicity and therefore obtain a homogeneous distribution of diamonds on the surface. They are then put again into distilled water and blow-dried with compressed air to avoid residue from the water. The substrates were then either drop-casted or spin-coated with aqueous diamond solutions. For the former, the substrates are heated to a temperature of 60 °C and drops of a volume of about 5  $\mu L$  are dropped onto the substrate. If substantially more than 5  $\mu L$  is needed, then several drops of about 5  $\mu L$  are dropped onto the substrate consecutively. A single large drop is ill-advised since the solution would flow off the substrate before drying. For spin-coating, a spin coater was build on-site used. Here, drops of 5  $\mu L$  are dropped on the substrate and the spin-coater set to a velocity of 2500 rpm for 3 min.

### **4.5 Listing of available samples**

#### 4.5. LISTING OF AVAILABLE SAMPLES FABRICATION OF NANODIAMONDS

Table 4.2: Listing of available wet-milled samples. The first column indicates the names of the samples, the second the mean diameter of the nanodiamonds, and the third designates how the silicon was incorporated into the diamond.

Sample name	Size	Si incorporation	Post-processing
hphtimp45	45 nm	<i>implanted</i>	oxidized in air at 450 °C
hphtimp80	80 nm	<i>in-situ</i>	annealed in vacuum for 1 h at 1000 °C and at 900 °C for 3 h
hphtimp260	260 nm	<i>in-situ</i>	oxidized in air at 450 °C
insitu50	50 nm	<i>in-situ</i>	series of individual samples with diverse post-processing steps
insitu70	70 nm	<i>in-situ</i>	series of individual samples with diverse post-processing steps
insitu70n	70 nm	<i>in-situ</i>	no post-processing subset of insitu70
insitu70o	70 nm	<i>in-situ</i>	oxidized in air at 450 °C subset of insitu70
insitu100	100 nm	<i>in-situ</i>	series of individual samples with diverse post-processing steps
insitu100ao	100 nm	<i>in-situ</i>	annealed in vacuum at 900 °C, consecutively oxidized in air at 450 °C subset of insitu100
implanted250ao	250 nm	implanted	annealed in vacuum at 900 °C, consecutively oxidized in air at 450 °C
hphtimp260	40 nm	implanted	annealed in vacuum at 1200 °C, consecutively oxidized in air at 450 °C
hphtimp260	50 nm	implanted	oxidized in air at 450 °C
hphtimp260	240 nm	implanted	annealed in vacuum at 1200 °C, consecutively oxidized in air at 450 °C
hphtimp260	260 nm	implanted	oxidized in air at 450 °C

---

---

# Chapter 5

## Quality of Nanodiamonds

### Remark:

Ich hab das kapitel jetzt nochmal ueberarbeitet indem ich den aufbau vom SiV papier hier uebernommen hab. Das gibt nochmal einen besseren ueberblick. Es gibt aber noch loecher die du nochmal dezidiert stopfen solltest. Besonders die section mit den post-processing methoden ist noch nicht auf dem niveau der anderen sections in dem kapitel.

- In der introduction werden qualitaetsprobleme genannt und ein paar methoden die da helfen sollen. Hier muss noch kurz erwähnt werden warum die methoden helfen.
- In der ersten section sind annealing und oxidation zusammen. Im text steht aber nur was annealing oder? Falls oxidation dann erst in der naechsten section kommt, sollte man die ueberschriften aendern. Ich kenn mich halt nicht aus, d.h. das passt noch nicht. Es muss auch klar werden welche probleme diese methoden potentiell loesen und warum.
- Was die surface treatments bewirken sollen bzw. wie die die qualitaetsprobleme minimieren? Da ist auch von shells die rede und ich hab keine ahnung was das fuer dinger sind. Hier fehlt auch noch was.
- Wenns um TEM messungen geht, dann ist hier auch von nanodiamond boundaries die rede. Hier sollte jetzt auch eine diskussion boundaries einfließen, bzw. was fuer negative effekte die haben koennen.

In this thesis we perform measurements of SiV centers hosted in high-quality wet-milled nanodiamonds. In this context we use the term quality as a measure of how close diamond crystals are to their pristine form. The presence of lattice imperfections such as additional vacancies, lattice strain, impurities or the inclusion of graphite or amorphous carbon is known to adversely affect crystal quality [?, ?, ?].

Surface contamination like graphite and amorphous  $sp^2$  hybridized carbon atoms manifest themselves as additional peaks in the Raman spectrum. Strain in the diamond

lattice broadens the first order Raman peak and causes it to shift to higher or smaller wavenumbers. Similarly, high concentrations of lattice defects cause additional peaks, a broadening of the first order Raman peak and a shift towards smaller wavenumbers.

To improve crystal quality and to reduce the mentioned distracting effects the following methods are deployed here: Annealing in a vacuum, oxidation in air as well as surface treatments involving plasmas.

To study the effectiveness of these treatments and to gauge the quality of our nanodiamond samples we rely on Raman spectroscopy and TEM imaging. The former is used to detect strain, quantify defect concentration and the presence of carbon in non-diamond phases, while the latter enables imaging of individual nanodiamonds revealing details in crystallinity such as crystal boundaries.

## 5.1 Quality-improving Post-Processing Treatments

### 5.1.1 Annealing and Oxidation

During silicon implantation the diamond lattice gets damaged by the penetrating ions.  $sp^2$  bonds, carbon interstitials and vacancies disrupt the metastable equilibrium of the diamond phase. Hence, there is a tendency for damaged diamond to "tip over" to the thermodynamically stable form of carbon, i.e. graphite. At temperatures above about 500 °C, vacancies in the diamond lattice become mobile and diffuse towards the surface[?]. Literature suggests, that annealing at 900 °C for 1 h is sufficient to remove most of the damage following implantations. To reduce the damage in the diamond lattice even further, we anneal the implanted diamonds at 900 °C to 1200 °C for 3 h to 6 h in vacuum ( $10^{-6}$  Pa).

The surface of the nanodiamonds is contaminated with graphite and amorphous  $sp^2$  hybridized carbon . We apply oxidation in an oven under ambient air at a temperature of 450 °C for 3 h to 6 h.

### 5.1.2 Surface Treatment With Gas And Plasma

We wanted to assert whether surface treatments with different gases influence the emission properties, so we treated them with hydrogen ( $H_2$ ), oxygen ( $O_2$ ), ozone ( $O_3$ ) all both at room temperature and at 500 °C; and also with  $H_2$  plasma. However, we found that most nanodiamonds treated in this way only showed luminescence which immediately bleached when illuminated with a cw 660 nm laser even at low excitation powers of 200  $\mu$ W, or no luminescence at all. We double-checked with a CCD-image of the surface to be sure that there are nanodiamonds in the focus. This bleaching occurred so quickly, that after a scanning no spectrum could be taken. The only samples which did yield spectra with measurable ZPLs were the ones treated with  $H_2$ . However, also

these SiV centers were not single ones. Therefore, we did not further investigate these samples.

One sample showed shells around the nanodiamond after oxidizing in air. We attribute this effect to a contamination in the oven. When we illuminated these nanodiamonds in the SEM for several moments, the shell went away. We therefore deducted that the shell is organic material. To get rid of the shells on the whole sample, we treated it with oxygen-argon plasma for 3 min<sup>1</sup>. After the first treatment, the shells were smaller, but not gone. So we put them into the oxygen-argon plasma again for 3 min, however, the shells were bigger than before any treatment. We tried another approach to get rid of the shells with ozone treatment for 4 h at 360 °C. Before ozone treatment there the diamond Raman line and other Raman lines visible. After surface treatment, more lines appeared and all of these other lines got more intense. There are probably organic contaminations on the sample in which functional groups got introduced by the ozone treatment. We did not further investigate this sample and defined it as broken.

## 5.2 Raman Measurements

Raman spectroscopy of various samples gives insight into crystal quality and surface contamination of nanodiamonds. Raman scattering is the inelastic scattering of a photon  $\hbar\omega_i$  on a molecule or crystal lattice in the initial state  $|i\rangle$  with energy  $E_i$ . The molecule or crystal transitions into a higher energy state  $E_f$  and the scattered photon with frequency  $\omega_s$  loses the energy  $\Delta E = E_f - E_i = \hbar(\omega_i - \omega_s)$ . Therefore, energy is exchanged between the photon and the excited matter, changing the rotational or oscillation energy of the involved molecule or the oscillation energy, i.e. phonons of the crystal lattice. The Raman shift is typically referenced in wavenumbers. It is given by:

$$\Delta\omega = \left( \frac{1}{\lambda_{ex}} - \frac{1}{\lambda_R} \right) \quad (5.1)$$

As every solid exhibits characteristic phonon modes tied to the properties of its lattice structure, Raman spectroscopy can be used to characterize diamond. Raman measurements of wet-milled nanodiamonds give insight into the issues of surface contamination, lattice strain and defect concentration: Surface contamination like graphite and amorphous sp<sup>2</sup> hybridized carbon atoms cause additional peaks in the Raman spectrum. A high defect concentration may lead to additional peaks, a broadening of the first order Raman peak and a shift to smaller wavenumbers. Strain in the diamond broadens the first order Raman peak and causes a shift to higher wavenumbers [?, ?, ?].

For the Raman measurements the same layout of the setup described in ?? is used. As an excitation light source, a 532 nm continuous wave diode laser is used (IO ). It provides single frequency mode laser light, a prerequisite for Raman investigations. The beamsplitter is a dichroic mirror (DRLP645), the laser light is additionally filtered out with a 532 Notch filter in the detection path in front of the single mode fiber instead

type

<sup>1</sup>Treatment performed by J. Schmauch, group of R. Birringer, Saarland University

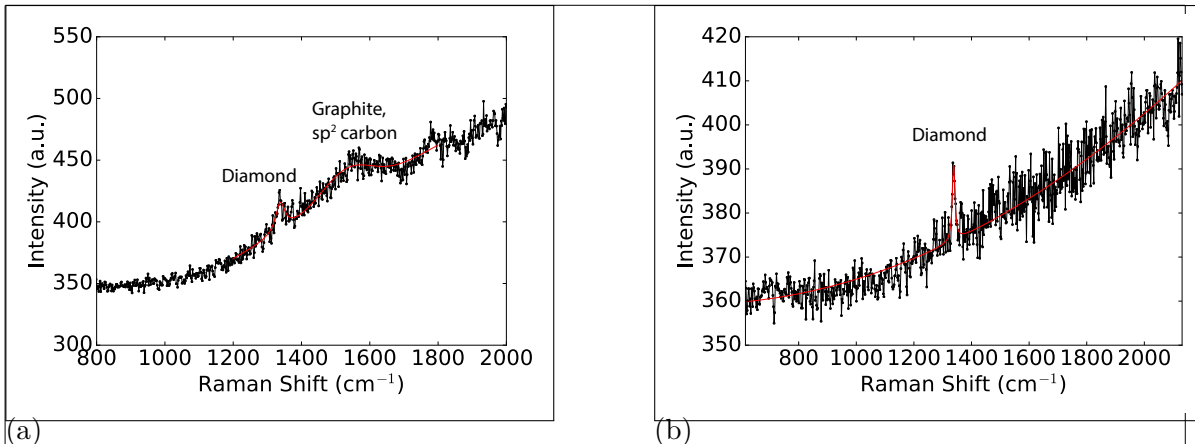


Figure 5.1: Raman measurements, black: data, red: fit. (a) Raman measurement before oxidation, sample insitu70. The diamond Raman peak is situated at  $1338\text{ cm}^{-1}$ . The broad feature around  $1580\text{ cm}^{-1}$  corresponds to the graphite G-band. (b) Raman measurement after oxidation, sample insitu70o. The G-band has vanished, indicating removal of graphite and amorphous  $\text{sp}^2$  hybridized carbon.

of a long pass filter. With these adaptations, the combination of the confocal unit and the spectrometer serves as a Raman spectrometer. As the diamond Raman line is very narrow, the 600 grooves/mm grating is used to as a starting point. Detailed measurements are realized using 1200 grooves/mm and 1800 grooves/mm gratings.

Since the size of single nanodiamonds is on the order of tens of nanometers, low signal intensities can become an issue when taking Raman measurements. To overcome this problem we pursue two different approaches:

- Nanodiamond Clusters: Collective measurements are carried out at several areas on the sample insitu70. Since this sample is densely covered with nanodiamonds, collective measurements of clusters of nanodiamonds (??) achieves higher signal intensities.
- Big Nanodiamonds: Raman measurements are carried out on the implanted sample implanted250ao. For this sample, diamond particles are big enough to yield sufficient intensities on single nanodiamonds.

### 5.2.1 Surface Contamination

We test the impact of oxidation treatment as described in ?? on surface contamination. ?? shows a measured Raman spectrum of a sample without oxidation treatment (insitu70n). To verify reproducibility, the measurement is performed on three different spots of the sample. The narrow peak in ?? corresponds to the first order diamond Raman peak and will be further analyzed in ?? . The spectrum also shows a broad

peak with a Raman shift of about  $(1582 \pm 5) \text{ cm}^{-1}$ . This shift corresponds to the G-band due to amorphous  $\text{sp}^2$  hybridized carbon atoms and graphite. The exact G-band position and linewidth is sensitive to parameters such as the clustering of the  $\text{sp}^2$  phase, bond-length and bond-angle disorder, presence of  $\text{sp}^2$  rings or chains, and the  $\text{sp}^2/\text{sp}^3$  ratio [?]. The nanodiamond Raman spectra are considerably modified after oxidation in air at  $450^\circ\text{C}$ . To verify this, we perform Raman measurements on three different spots of a sample produced in the same process as the above mentioned, which is additionally oxidized (*insitu70o*). While the G-band peak is present in every measurement performed on a non-oxidized sample, it is not present in any of the oxidized samples (?? ), indicating successful removal of  $\text{sp}^2$  hybridized carbon and surface graphite.

### 5.2.2 Defect Concentration

Several effects impact the first order diamond Raman line: 1. defects in the diamond lattice, 2. hydrostatic pressure, 3. uniaxial or more complicated stress configurations. In the measurement on nanodiamond clusters the width of the diamond Raman peak of sample *insitu70* varies between  $15 \text{ cm}^{-1}$  and  $30 \text{ cm}^{-1}$  without oxidation treatment, but is only  $9 \text{ cm}^{-1}$  to  $11 \text{ cm}^{-1}$  after the oxidation process. A possible reason for this change of the width is improved crystal quality [?]. In the measurement on big nanodiamonds we measured a Raman line at  $(1308 \pm 5) \text{ cm}^{-1}$  (denoted line R1) which exhibits a broad linewidth of  $(25 \pm 5) \text{ cm}^{-1}$ . One plausible explanation for both the position and the linewidth of the Raman line are defects in the diamond lattice[?].

### 5.2.3 Lattice Strain

We investigated how strain in the diamond lattice manifests itself in both measurements on nanodiamond clusters and on big nanodiamonds. In the Raman measurement on nanodiamond clusters, the position of the diamond Raman peak is the same for oxidized (*insitu70o*) and non-oxidized (*insitu70n*) samples, indicating that oxidation does not affect strain in the diamond. However, the Raman shift of both non-oxidized and oxidized samples amounts to  $(1338 \pm 5) \text{ cm}^{-1}$ , as compared to the literature value of  $1332.5 \text{ cm}^{-1}$  of pristine diamond [?] (given uncertainties are governed by spectrometer resolution). This shift indicates the presence of strain in the diamond particles. Performing the Raman measurement on big nanodiamonds we found one diamond Raman line at  $(1308 \pm 5) \text{ cm}^{-1}$  (line R1), one at  $(1345 \pm 5) \text{ cm}^{-1}$  (line R2) and one at  $(1348 \pm 5) \text{ cm}^{-1}$  (line R3), indicating a broad distribution of strain among the individual diamond particles (uncertainties governed by spectrometer resolution). Only line R1 can be explained with a high defect concentration in the diamond lattice due to its shift to smaller wavelength. However, a more consistent model which explains all occurring shifts is the presence of strain in the diamond nano particles. From the linewidths in the measurement on big nanodiamonds, the strain in the diamond is calculated using

the equation for hydrostatic pressure [?]

$$\omega(P) = \omega_0 + a_1 P + a_2 P^2, \quad (5.2)$$

where  $\omega_0 = 1332.5 \text{ cm}^{-1}$ ,  $a_1 = 2.83 \text{ cm}^{-1} \text{ GPa}^{-1}$  and  $a_2 = -3.65 \times 10^{-3} \text{ cm}^{-1} \text{ GPa}^{-1}$ . The calculation yields a pressure in the investigated diamonds of  $-8.56 \text{ GPa}$  tensile stress and  $4.26 \text{ GPa}$  and  $5.50 \text{ GPa}$  compressive stress. Pressure uncertainties due to the Raman line measurements are smaller than one Pascal and are therefore neglected. Under hydrostatic pressure, the triply degenerate first order Raman peak remains degenerate, while under uniaxial and more complex stress configurations (biaxial stress, shear stress etc.) mode splitting occurs [?]. As mentioned above, we observe broad linewidths up to  $(25 \pm 5) \text{ cm}^{-1}$ . The broad linewidths of the Raman lines may be attributed to uniaxial strain, as mode splitting manifests itself in a broadening of the peak due to limited spectrometer resolution. Therefore, we conclude that both hydrostatic and uniaxial strain is present in the nanodiamonds.

### 5.3 Transmission Electron Spectroscopy Measurements

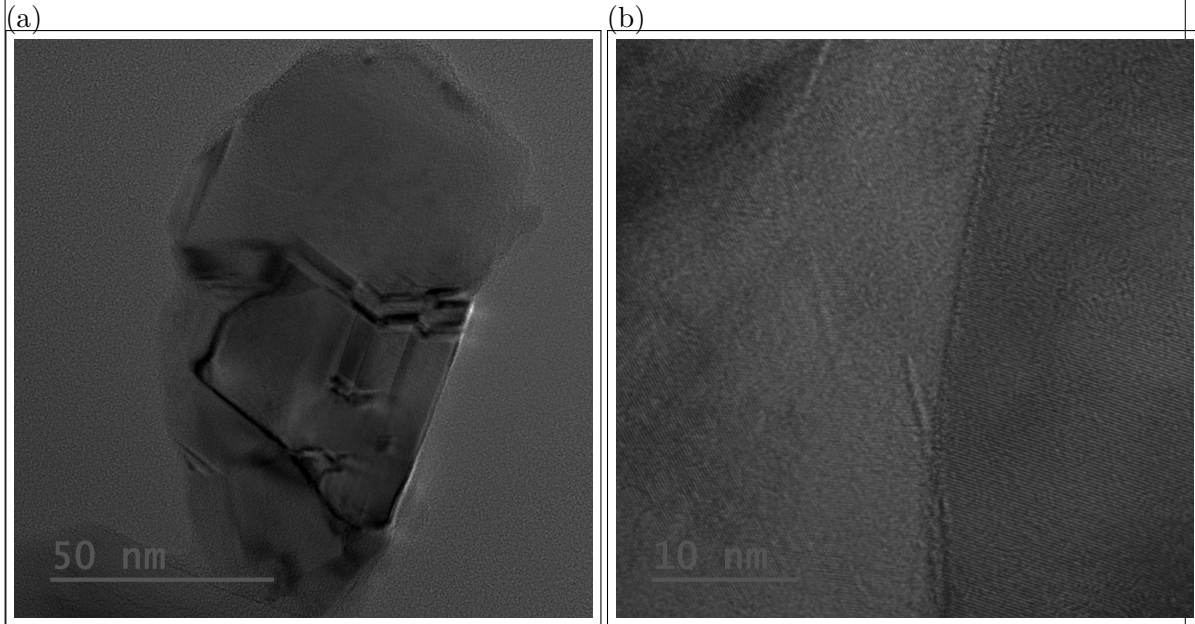


Figure 5.2: Transmission electron microscopy (TEM) pictures of sample insitu100. (a) Image of a single nanodiamond particle. Several crystal boundaries can be seen within the diamond particle. (b) Close-up image a diamond particle. The vertical line is a crystal boundary, to the left and right the more or less horizontal layers of one crystalline region can be seen.

Transmission electron microscopy (TEM, also sometimes conventional transmission electron microscopy or CTEM) is a microscopy technique in which a beam of electrons is transmitted through a specimen to form an image. The specimen is most often an ultra-thin section less than 100 nm thick or a suspension on a grid. An image is formed from the interaction of the electrons with the sample as the beam is transmitted through the specimen. During transmission electron microscopy a beam of electrons is transmitted through a sample, forming an image of the transmitted sample. Since electrons have higher de Broglie wavelengths than photons, a higher resolution is obtainable, allowing the surface of nanodiamonds to be resolved. Thus, the crystallinity of single nanodiamonds can be studied directly.

### 5.3.1 Crystallinity and Grain Boundaries

Sample insitu100 was investigated using TEM by J. Schmauch, group of R. Birringer, Saarland University. Smaller nanodiamonds would have been too small for the carbon grid which serves as a sample holder in the TEM, and might have fallen through the grid and bigger particles would have been too big to be transmitted by the electron beam, making the imaging impossible. In Figure 5.2 there are TEM images, one of them exhibits a single diamond particle and the other is a close-up image of a crystal boundary. From Figure 5.2a it can be seen that the diamond particle contains several crystallites and crystal boundaries. The edges of the crystallites are the sharp features within the diamond particle, the crystal boundaries the smoother features. In Figure 5.2b the crystal layers which are more or less horizontal and in the middle of the picture there is a vertical line which is the edge of a crystallite. So it is clear that the investigated sample does not contain beautiful single crystal diamond particles, which means a reduction of the crystal quality of the diamond particles.

er nur  
vermu-  
tung

---

---

# Chapter 6

## Spectral Distribution of SiV centers in Nanodiamonds

In this chapter we report our results regarding luminescence properties of SiV centers. The samples used in our investigation consists of a large set of CVD nanodiamonds containing *in-situ* SiV centers of a size in the range of 70 nm to 100 nm. Throughout the chapter we refer to samples using their distinct sample-id as listed in ??.

The obtained fluorescence spectra of SiV centers show that both the center wavelength of the ZPL as well as the linewidth of the zero-phonon-line vary significantly among different samples. Our measurements over a large set of SiV centers indicate a strong correlation between the center wavelength of the zero-phonon-line and the corresponding linewidths, resulting in a previously unreported bimodal distribution. We assert single photon emission from these SiV centers across the whole range of zero-phonon-line positions and linewidths. Furthermore we detect fluorescence intermittency, i.e. blinking. The obtained data for the bright and dark times indicate an exponential decay of the dark state and a log-normal decay of the bright state, the latter of which has to our knowledge not been reported as of yet.

### 6.1 Photoluminescence spectra

To identify nanodiamonds containing SiV centers, we performed confocal scans of the samples. To reduce bias in the measurements, not only the brightest spots of the confocal scans are investigated, but also those which barely exceed background fluorescence. SiV centers are further investigated by measuring photoluminescence (PL) spectra, single photon statistics and photo-stability. As discussed in chapter 2, the typical luminescence spectrum of an SiV center is composed of a prominent zero-phonon-line peak and weak sidebands. Investigations of both are reported independently in the following paragraphs.

### 6.1.1 Zero-phonon-line

The center wavelength and the linewidth of the zero-phonon-line (ZPL) of SiV center luminescence spectra for samples insitu50, insitu70, and insitu100 are determined by fitting a Lorentzian fit to the ZPL. Both spectra from single and multiple SiV centers are taken into account . In Figure 6.1 the linewidth for each measured ZPL is plotted against its center wavelength.

What does that mean?

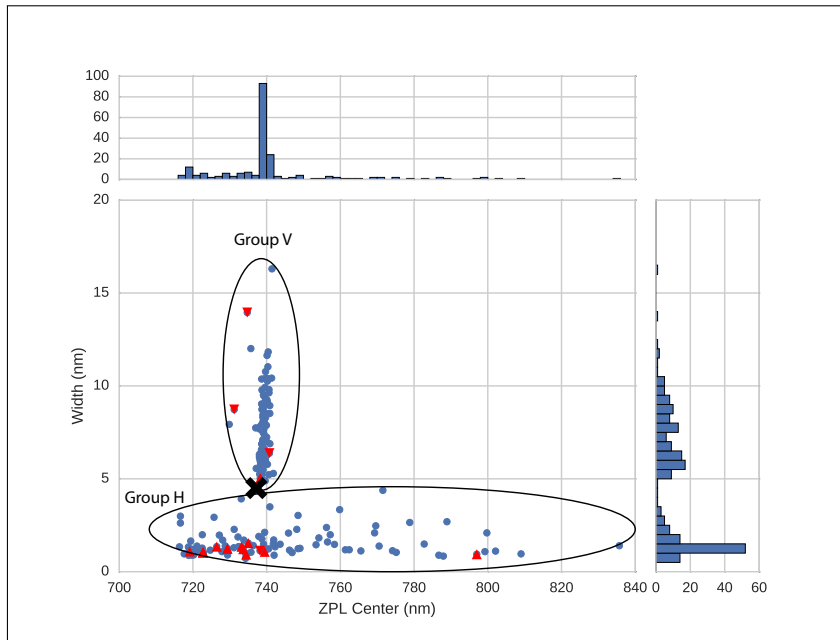


Figure 6.1: Distribution of the ZPL center wavelength versus the linewidth of the ZPL of the investigated SiV centers in milled nanodiamonds containing *in-situ* incorporated SiV centers for samples insitu50, insitu70, insitu100. The data separates into a horizontal (group H) and a vertical (group V) cluster. The bold black cross marks the position of an ideal SiV center in unstrained bulk diamond [?]. The red triangles indicate emitters with an anti-bunching dip in the  $g^{(2)}(0)$  measurement. Upwards pointing triangles represent blinking emitters (fluorescence intermittency), while triangles pointing down represent non-blinking emitters (see section 6.3).

What immediately strikes the eye is a pattern that to our knowledge has not been reported to date: The observed ZPLs partition into two groups, denoted a horizontal lobe (group H) and a vertical lobe (group V). The two lobes are separated by a gap, i.e. a region with a pronounced lack of data points. Single emitters are identified both in group H and group V, marked as red triangles in Figure 6.1. Further details on single emitters are given in section section 6.2.

The two groups are defined by their characteristic center wavelengths and linewidths: In group H very prominent ZPL peaks are found showing linewidths in the range of 1 nm to 5 nm and center wavelengths in the range of 715 nm to 835 nm. Figure 6.2a shows a representative spectrum of a single emitter in group H (denoted emitter H1), exhibiting a ZPL line width of 1.4 nm and a center wavelength of 726.5 nm. In contrast,

in group V, the spectra exhibit broader ZPL linewidths of approximately 5 nm up to 18 nm. Their ZPL center wavelengths, however, are distributed within the very narrow range of 738 nm to 741 nm. Figure 6.2b shows a spectrum of a single emitter of group V (denoted emitter V1) with a ZPL linewidth of 6.4 nm and a center wavelength of 740.8 nm. For comparison, the room temperature ZPL of SiV centers in unstrained bulk diamond exhibits a linewidth of 4 nm to 5 nm and a center wavelength of 737.2 nm marked with a black cross in Figure 6.1 [?, ?].

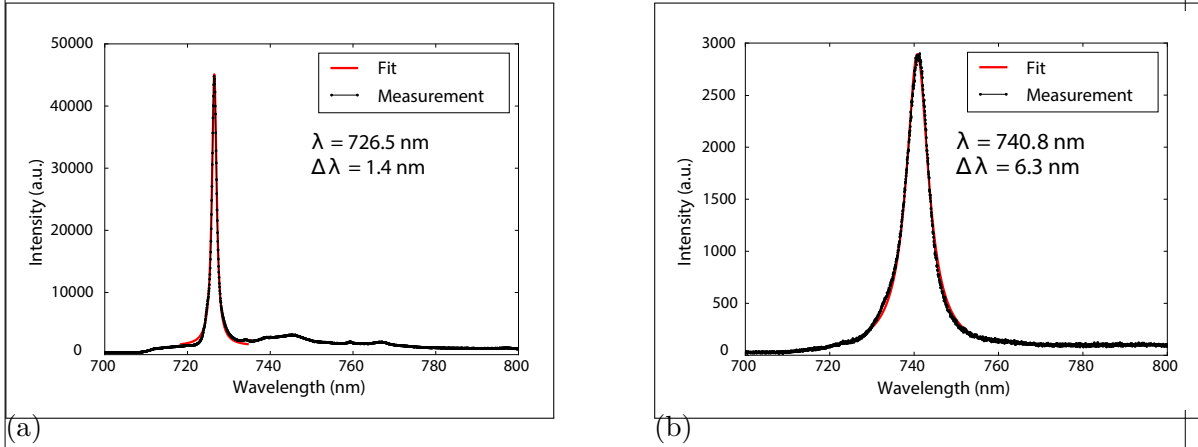


Figure 6.2: Representative photoluminescence spectra of sample insitu100ao measured at room temperature. (a) Spectrum of group H of Figure 6.1, denoted emitter H1. (b) Spectrum of group V of Figure 6.1, denoted emitter V1. The red lines are Lorentzian fits to the peaks.

To determine how much the ZPLs contribute to the total observed emission of emitter H1 and emitter V1, we determine the Debye-Waller factors for both. The Debye-Waller factor is defined by  $DW = I_{ZPL}/I_{TOT}$  and is therefore suited as a measure for sideband intensity. The Debye-Waller factor for emitter H1 amounts to  $0.81 \pm 0.01$  (given uncertainty due to fit). This Debye-Waller factor corresponds to a Huang-Rhys factor  $S = -\ln(DW)$  [?] of  $0.21 \pm 0.01$ , which is in good agreement with the values reported in [?]. The error is mainly due to background corrections. When zooming in onto the spectrum of emitter V1 we do not find distinct sidebands peaks, i.e. almost all emission for this emitter is allotted to the ZPL. Considering resolution limits of the spectrometer, dark-counts and fluorescence background, we evaluate the Debye-Waller factor to be larger than 0.97. It is the largest Debye-Waller factor amongst all our milled SiV centers. The two mentioned Debye-Waller factors should not be interpreted as single representative emitters for the respective groups, they rather serve as an orientation of the spread of the Debye-Waller factors of both groups. It has to be pointed out, that we did not find any systematic difference of the Debye-Waller factor between group H and group V.

To provide context for the novel findings presented in Figure 6.1, we compare our results to various earlier findings. Furthermore, we discuss an additional comparison to an investigated control sample fabricated using silicon implantation. The results are presented in Figure 6.3.

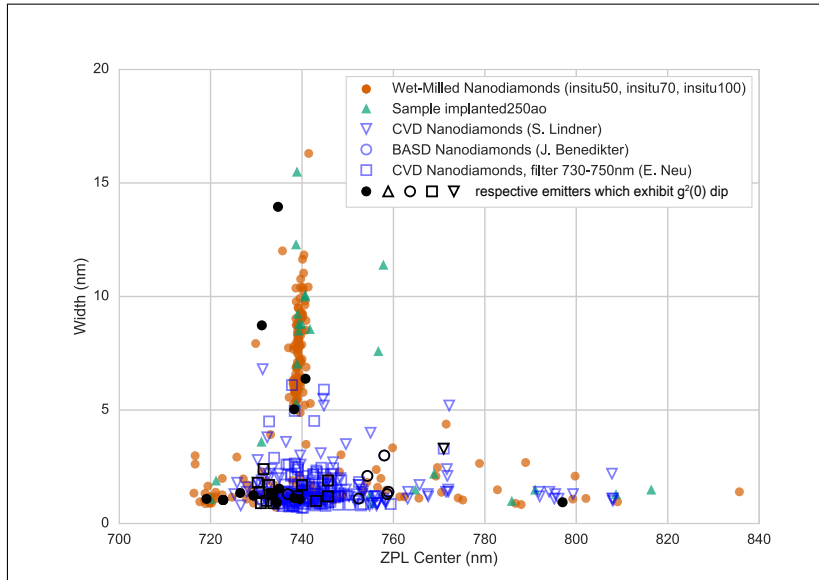


Figure 6.3: Comparison of the distribution of the linewidth vs. the center wavelength of the ZPL of the investigated SiV centers in milled nanodiamonds (samples insitu50, insitu70, insitu100) with data measured on sample implanted250ao (implanted with Silicon); with data measured in our group on CVD nanodiamonds produced by M. Schreck [?]; with data measured on nanodiamonds reported by J. Benedikter in [?]; and with data measured in CVD diamonds by E. Neu in a filter window between 730 nm and 750 nm [?]. Black symbols represent emitters exhibiting a dip in the  $g^{(2)}(0)$  function, indicating a single or very few SiV centers

Samples for which previous data has been taken are:

1. nanodiamonds produced by bead-assisted sonic disintegration (BASD) of polycrystalline CVD diamond films (blue rings in Figure 6.3 [?]; data taken from [?])
2. nanodiamonds produced directly via a CVD process with *in-situ* incorporated SiV centers; measured in a spectral filter window of 730 nm to 750 nm (blue squares in Figure 6.3; data reused from [?] with permission)
3. nanodiamonds produced in the same manner as the CVD sample in 2 (blue downwards pointing triangles in Figure 6.3; produced by M. Schreck [?]; spectroscopic measurement performed with setup described in ??)

All previous data from different nanodiamond material fit nicely with the ZPL distribution presented in Figure 6.3, confirming the findings of Figure 6.1.

We verify that the observed luminescent defects are indeed silicon related by performing control experiments with silicon implanted samples (sample implanted250ao). By doing so we rule out the possibility that the two lobes in the distribution are a result of artifacts. Such artifacts include other elements incorporated into the nanodiamonds during the growth process: Residue from previous processes performed in the diamond growth chamber or material from chamber parts may be incorporated during nanodiamond growth. Figure 6.3 shows that the implanted SiV centers cover roughly the same spectral range as the *in-situ* incorporated centers from around 720 nm to 820 nm as the *in-situ* incorporated centers. This correlation provides strong evidence for the silicon related origin of the defects.

To provide a theoretical interpretation, the ZPL center wavelength shift is investigated in further detail and compared to results from density functional calculations. Zooming in to group V (Figure 6.4a) it becomes clear that only six of the measured data points in group V are situated at a shorter center wavelength than the point attributed to an ideal SiV center in unstrained bulk material. The shortest wavelength shift is at 729.9 nm. At the same time, much more data exhibit a center wavelength bigger than the ideal SiV center. This asymmetry suggests that a red-shift of the ZPL of an SiV center is significantly more likely than a blue-shift.

Several mechanisms contribute to the center wavelength shift, predominantly hydrostatic and material strain. As explained in ??, we measured the Raman shift of samples *in-situ* and implanted250ao. These measurements indicate strain in the diamond lattice in the range of -8.56 GPa to 4.26 GPa. Figure 6.5 shows results from density functional calculations. The shift of the ZPL is modeled in dependence of pressure in the diamond lattice both for hydrostatic stress and for uniaxial stress. Figure 6.5 illustrates that the assumption stated in ??, namely that the strain in the nanodiamonds is due to hydrostatic and uniaxial stress, corresponds well with the measured ZPL shifts in group V.

With higher uniaxial pressure, the ZPL becomes more and more red-shifted. The blue shifted ZPL center wavelengths are explained by hydrostatic stress in the diamond material. The strain calculated from the Raman measurements corresponds well with

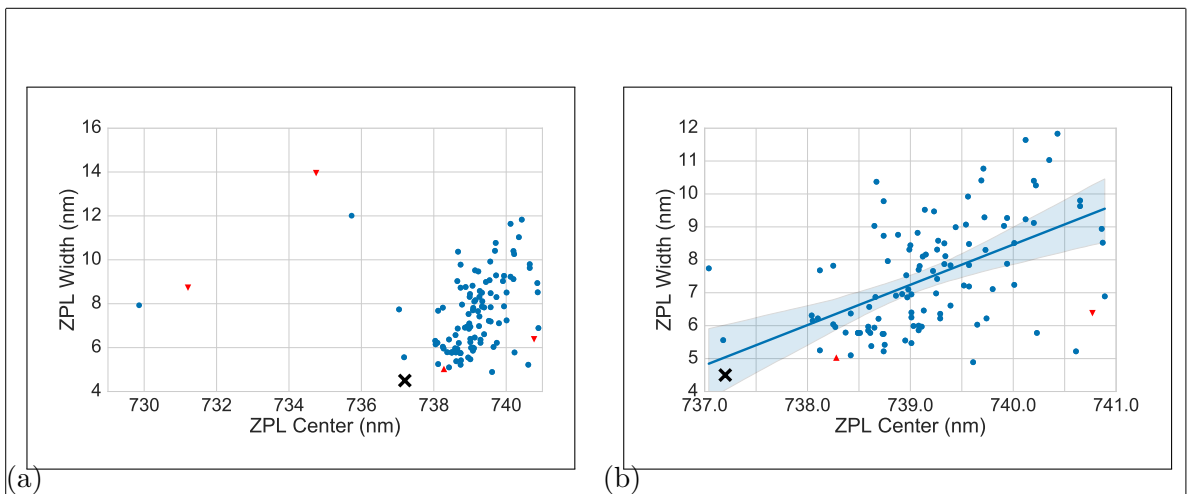


Figure 6.4: (a) A zoom into group V. While many data points exhibit higher center wavelengths (i.e. a redshift) than the ideal SiV center in bulk, only few exhibit shorter center wavelengths (i.e. a blue-shift). (b) Zooming further into group V, a clear trend of broader ZPL linewidths for larger ZPL center shifts is visible. The line is a linear regression to all data points between 737 nm and 741 nm which exhibit a linewidth bigger than 4 nm.

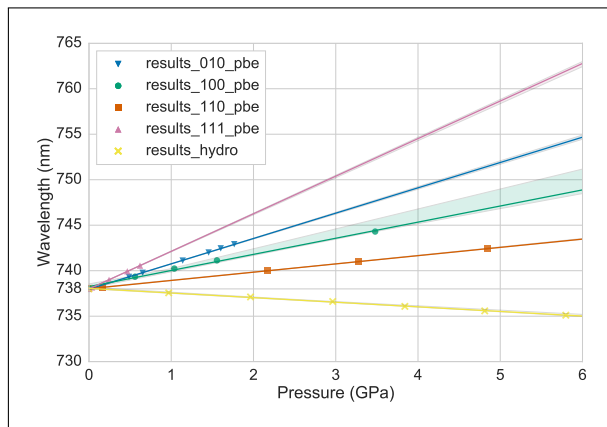


Figure 6.5: Calculations of the wavelength of the SiV center ZPL in dependence of pressure. Markers: calculated pressure with PBE functional; Lines: linear fits to the calculated points, the shaded area around the lines representing the one sigma (68%) confidence interval. Yellow: hydrostatic pressure; other colors: uniaxial pressure, for different orientations. All calculations are performed with a PBE functional. Hydrostatic-type pressure causes a moderate blue shift whereas uniaxial strain causes larger redshift with different magnitudes depending on the direction of the strain

the results in Figure 6.5 for group V. However, the measured shifts in group H are too broad to be solely explained by strain in the diamond. A potential explanation for the very broad distribution of defect center ZPL center wavelengths could be the association of SiV centers with a further nearby defect, such as a vacancy, or a modified SiV complex such as SiV:H [?].

Zooming in to group V, another effect becomes visible (Figure 6.4b): With increasing ZPL center wavelength, the linewidth becomes broader. As discussed above, a red-shift of the ZPL is linked to increasing uniaxial strain. Thus we conclude that the ZPL linewidth too is affected by strain in the diamond lattice. Here, a modified electron-phonon coupling [?] causes increased uniaxial stress, resulting in larger linewidths. A similar effect has been previously observed for SiV centers at cryogenic temperatures [?].

To conclude, we are able to explain the distribution of ZPL center wavelengths in group V very consistently with theoretical predictions based on perturbative shifts due to strain in the diamond lattice. On the other hand, we have to assume that group H is comprised of modified SiV centers, the structure of which is currently unclear.

### 6.1.2 Sideband

It is known that the photoluminescence spectra of SiV centers in nanodiamond are dominated by the zero-phonon-line. As a result phonon side band contributions remain small, a fact expressed in large Debye-Waller factors of over 70 % established previously [?, ?]. Our own measurements are consistent with these of emitter H1 and emitter V1 results. We also find distinct sideband peaks in many SiV center photoluminescence emission spectra. The investigated emitters exhibit two different structures of sideband spectra: The spectra in group V exhibit one strong sideband peak, spectra in group H exhibit several weaker sideband peaks. Figure 6.6a and Figure 6.6b illustrate the respective observations.

Most of the spectra in group V exhibit a characteristic shape, composed of the ZPL and one strong sideband peak. 70 % of the photoluminescence spectra with one distinct sideband peak exhibit a shift of the sideband peak from the ZPL between 37 meV to 43 meV. The range of line shifts for the prominent sideband peak coincides with a well-known feature at 42 meV, associated with SiV centers [?, ?], but also to a larger number of optically active defects [?]. The occurrence of this 42 meV sideband feature for a large number of defects and the absence of isotopic variations [?], favors an assignment as non-localized lattice vibration. We furthermore observe that the dominant sideband peak shifts towards smaller distance from the ZPL for increasing ZPL center wavelength, i.e. increasing strain. Figure 6.7 presents a linear fit to data for emitters in group V.. The low phonon energy of the sideband feature and its shift with strain might arise from a local “softening” of the crystal lattice in the vicinity of a defect [?].

A recent study [?] suggests that the 42 meV mode, similar to other broad phonon side band features, originates from a resonance attributed to phonons causing the dynamical Jahn-Teller effect with SiV centers [?]. As the Jahn-Teller coupling varies with strain

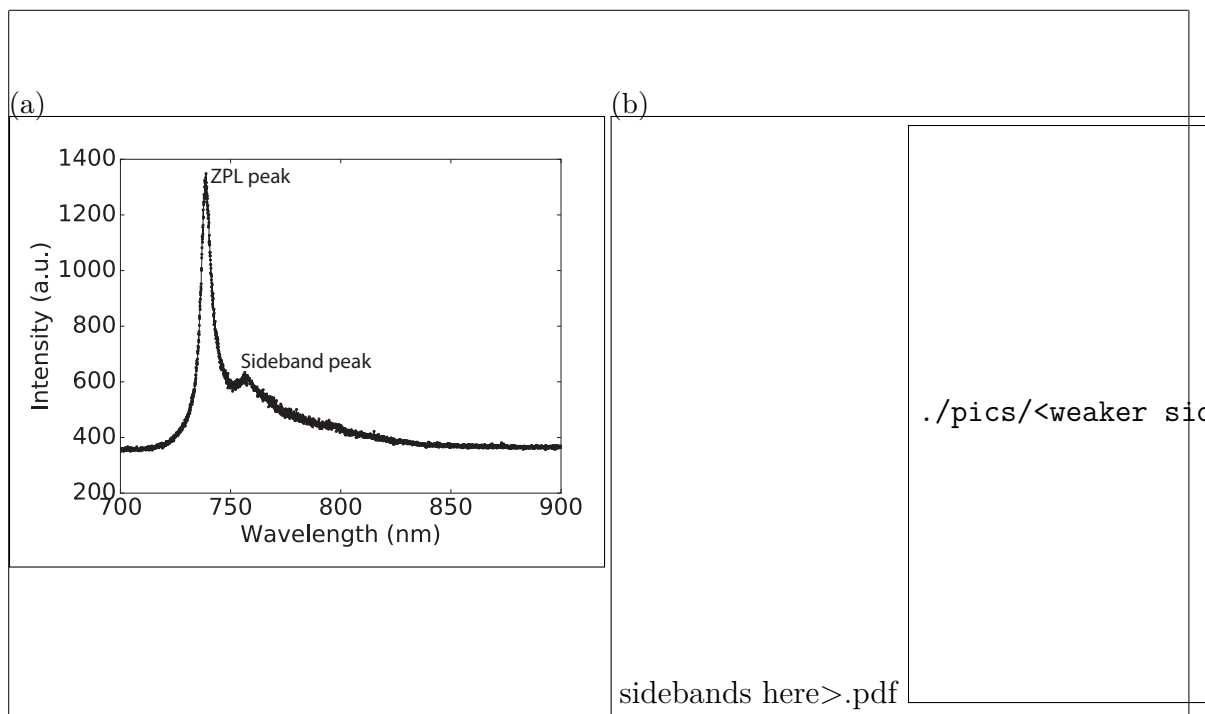


Figure 6.6: Representative spectra of emitters showing single (a) and multiple (b) sideband peaks. The former belong to group V, while the latter are members of group H.

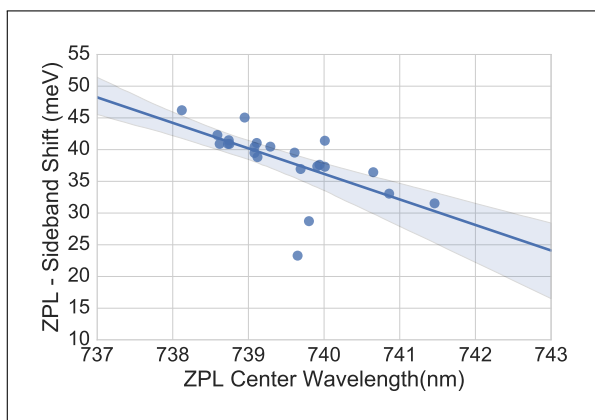


Figure 6.7: Shift of dominant sideband peak from the ZPL in spectra of SiV centers (group V, samples insitu50, insitu70, insitu100) vs. ZPL center wavelength. The linear fit shows that the shift decreases with increasing ZPL center wavelength, i.e. with increasing strain and exhibits a slope of  $(-4 \pm 1) \text{ meV nm}^{-1}$ . The shaded area is the 95 % confidence region.

it is also expected that the resonance shifts accordingly.

In the spectra of group V, we do not observe a typical SiV center sideband feature at 64 meV, attributed to a local vibration of the silicon atom, frequently much stronger than the 42 meV sideband peak. A possible explanation is, that the lattice mode at 37 meV to 43 meV is so strong that the local vibrational mode at 64 meV cannot be separated from the tail of the lattice mode.

In group H we observe many spectra which exhibit several peaks within the spectral range of our detection range between 710 nm to 900 nm. The challenge arises to unequivocally distinguish between peaks stemming from a phonon sideband and peaks stemming from shifted, less intense SiV center ZPLs.

Interestingly, we assert a tendency for peaks to accumulate at a shift of around 43 meV, 64 meV, 150 meV and 175 meV. This pattern in the phonon side band of group H is consistent with side band shifts reported in [?, ?, ?].

The possibility exists, that some these peaks believed to be phonon side bands are actually shifted ZPLs stemming from other SiV centers. To address this question, we perform photoluminescence measurements at cryogenic temperatures.

### 6.1.3 Cryostatic Measurements

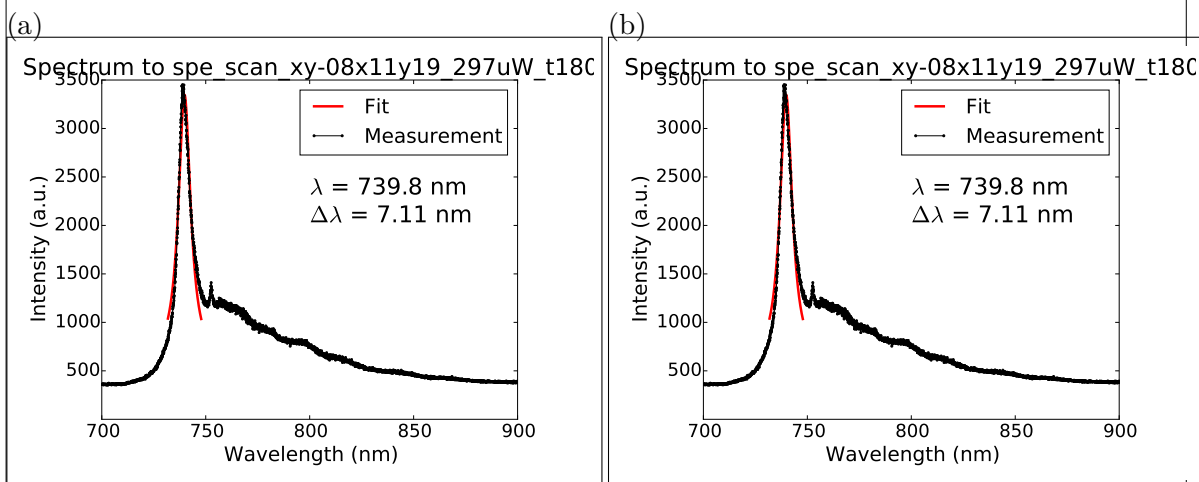


Figure 6.8

#### Remark:

den teil mit den cryogenic measurments musst du nochmal ordentlich aufschreiben.  
Hier fehlen noch dinge.

- Wie hast du messungen ueberhaupt machen koennen? Das setup in ?? spricht ja nicht von tieftemperaturen. Hast du den aufbau von jemand anderem (janine?) benutzt? Wenn ja dann unbedingt erwaehnen. Ansonsten erklaeren

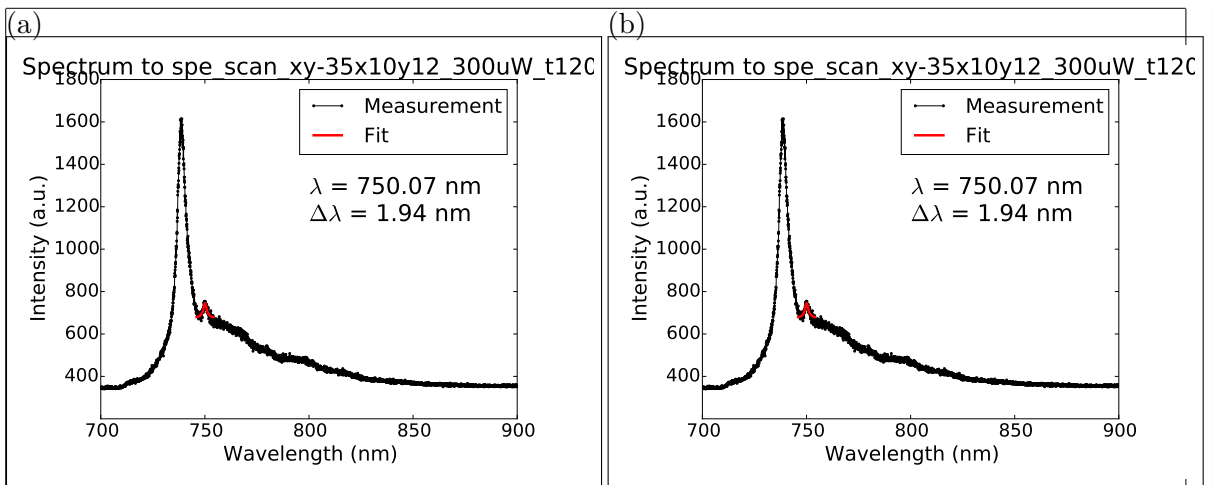


Figure 6.9

wie sich der genutzte aufbau vonm normalen unterscheidet.

- die bilder die du da bereits eingefuegt hast, die versteh ich nicht. Sind das nur platzhalter und da kommt noch was anderes hin? Ich seh den Zusammenhang die geschichte mit der feinstruktur nicht. Das sollte noch geklaert werden.
- wenn man die 4-fach aufspaltung nicht sieht und stattdessen mehrere linien hat, was bedeutet das? Klar ist, man hat kein einzelnes SiV center am start. Abgesehen davon, laesst sich noch was anderes sagen? Wenn man den wood vor lauter lines nicht sieht, dann heisst das auch, dass man nicht sagen kann ob manche der phonon side band peaks von anderen SiV centers kommen oder nicht. Wenn hier keine konklusive aussage moeglich ist, dann sollte das diskutiert werden.
- die sache mit den multiple lines that were strained is mir nicht klar. Soll das heissen die waren verschoben und der grund dafuer war strain? wenn ja, verschoben gegeneuber welchem wert, man erwartet ja 4 lininen fuer SiV centers.

We performed some cryostatic measurements to to pursue two goals: First, if we see the four-level splitting of the ZPL this is further proof that the dominant peaks of our spectra are indeed all due to SiV centers and do not stem from other impurities. Second, if the sideband peaks vanish at cold temperatures, this is evidence that they are caused by phonons. So we cooled down a sample, but all we saw was a wood of lines. Apparently, there were multiple SiV centers in the nanodiamonds and they were all strained, messing up the four-level line structure.

## 6.2 Photon correlation measurements

**Remark:**

Ich hab hier mal die paperversion hinkopiert. Mir ist aufgefallen, dass du in der diss version noch andere plots mit erklaerungen hattest. Ich schlage vor du fuegst das was in der neuen noch fehlt einfach ein. Dann ist sichergestellt, dass wir den text aus dem paper konsistent erweitern. Der alte text ist auskommentiert vorhanden.

The investigated SiV centers exhibit count rates of a few thousand to a few 100 000 counts per second (cps). We carried out measurements of the photon statistics and found that about 3 % of luminescent nanodiamonds contain single color centers. These measurements show, that the probability of finding a single emitter does not correlate in any way with the center wavelength or the linewidth of the ZPL. We found several single SiV centers with an anti bunching dip down to about 0.2 and attribute the residual  $g^{(2)}(0)$  value to background fluorescence from the diamond host. For the utilized nanodiamonds a background measurement without simultaneously measuring SiV center photoluminescence is infeasible, because the laser spot size is bigger than the nanodiamond, i.e. the SiV center will always be excited when the nanodiamond is illuminated. Therefore, the background is estimated from the sideband of SiV center spectra. The measured lifetimes of the single SiV centers are in the range of about 1 ns to 9 ns, which is of the same order as previous research suggests [?, ?]. Figure 6.10 shows the  $g^{(2)}$  functions of the two emitters introduced in ??, emitter H1 and emitter V1.

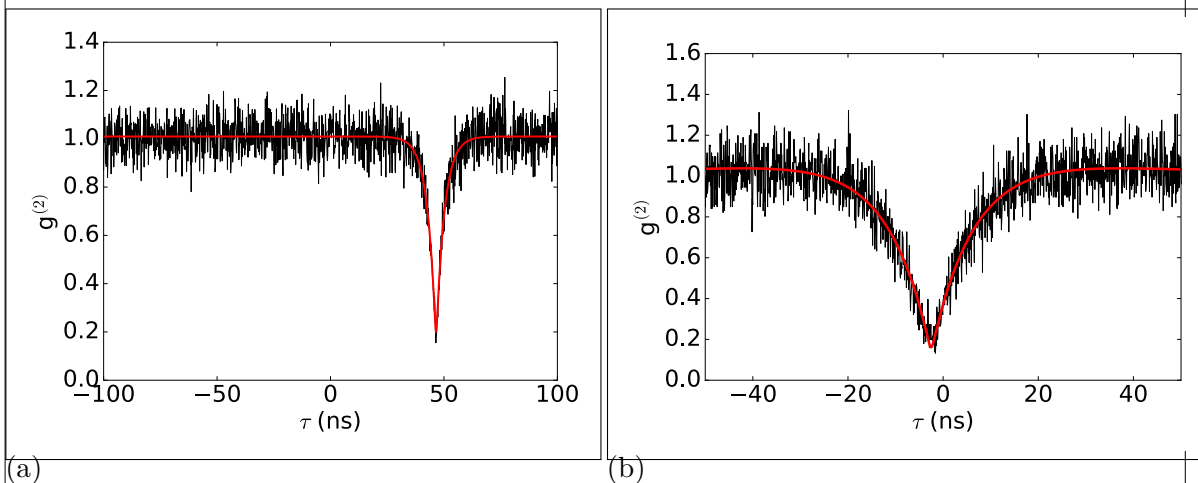


Figure 6.10: (a) Intensity autocorrelation function of an emitter in group H. (b) Intensity autocorrelation function of emitter V1 at an excitation power of 200  $\mu$ W (saturation power is 1 mW).

Figure 6.10a shows the photon correlation function of an emitter in group H. The shift of the dip to  $\tau = 50$  ns originates from a path length difference of the two detection paths in the Hanbury Brown and Twiss setup. The  $g^{(2)}(0)$  value of the fit is 0.20. The excited state lifetime of the emitter was determined to be  $(3.8 \pm 0.1)$  ns.

Figure 6.10b shows the  $g^{(2)}$  function of emitter V1 at an excitation power of 200  $\mu$ W, which is 20 % of the emitter's saturation power  $P_{sat} = (1.0 \pm 0.1)$  mW. The  $g^{(2)}(0)$

value yields 0.16. It is a representative  $g^{(2)}$  measurement of single SiV centers. It is well below 0.5, indicating single photon emission. The non-vanishing  $g^{(2)}(0)$  value is caused by background fluorescence of the diamond. The lifetime of the excited state of this emitter is  $(9.2 \pm 0.2)$  ns. It is the highest excited state lifetime we measured within this work.

Several nanodiamond photoluminescence spectra contain multiple narrow distinct peaks at different wavelengths. This circumstance is attributed to nanodiamonds containing more than one SiV center, each of which is subject to a different ZPL wavelength shift. We choose narrow bandpass filters to perform independent measurements of each individual peaks of such a spectrum. As a result it is possible to measure  $g^{(2)}(0)$  values below 0.5 for each of these narrow peaks. Hence the individual peaks are identified as single emitters with a different ZPL center wavelength.

We do not see a systematic difference regarding the photon autocorrelation functions of group H and group V, both reach similar  $g^{(2)}(0)$  values. Also, the timescales of the excited state lifetimes coincide.

## 6.3 Photostability

### Remark:

Auch hier hab ich einfach mal den gut formulierten text vom paper hineinkopiert.  
Wenn du aus dem alten text noch sachen einfuegen willst, dann gern. Ich hatte hier  
den eindruck, dass so ziemlich alles schon da ist, aber vielleicht taeusch ich mich.

As mentioned in the previous section, the single photon count rates observed from the investigated SiV centers varies strongly between a few thousand to a few 100 000 cps. To further investigate the count rate, the luminescence time trajectory of the emitters which exhibit a dip at  $g^{(2)}(0)$  is evaluated. It is found that some of the observed emitters exhibit fluorescence intermittence, also called blinking. Figure 6.11 illustrate the effect. Blinking is attributed to temporal ionization of the color center during optical excitation, forming an optically inactive charge state [?, ?, ?]. Therefore the emitters change between states of higher and lower emission, i.e. brighter and darker states, called blinking levels.

The photon count time trace of emitter H1 is shown in Figure 6.11. In the overview picture (Figure 6.11a), a few blinking dips can be seen with time intervals of up to a few minutes. The fact that the count rate never drops down to the dark count rate lets us assume, that there are at least two SiV centers present, one exhibiting fluorescence intermittence and one exhibiting a stable emission. When zooming in, shorter time intervals are observable (Figure 6.11b). The time intervals range from a few tens of milliseconds up to a few seconds with a few outliers exhibiting very long time intervals up to a few hundred seconds.

The bright and dark times exhibit different probability distribution functions and with that, different characteristic time constants. In Figure 6.12 the time intervals of the emitter are shown as small vertical dashed red lines and solid blue lines for the bright

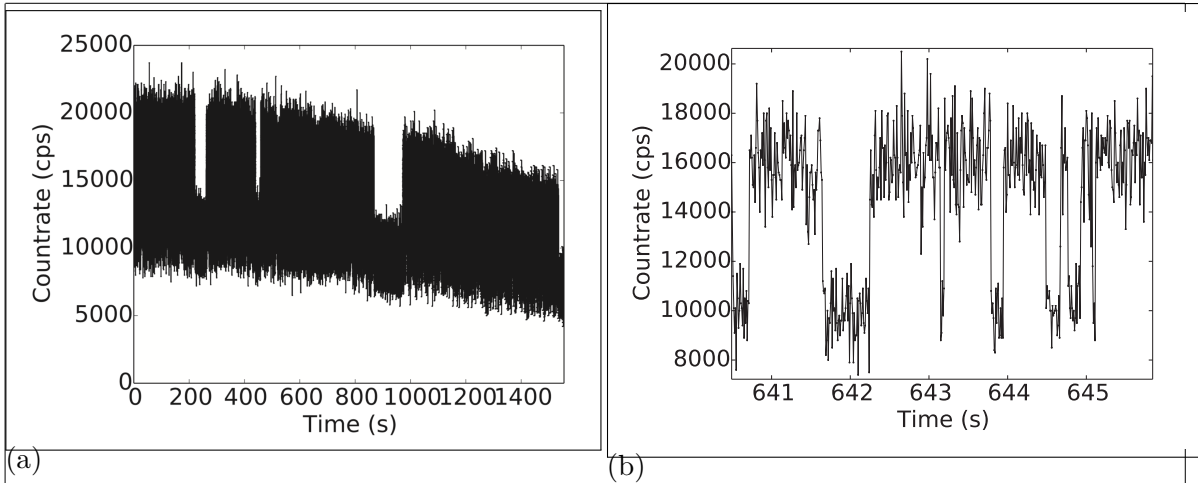


Figure 6.11: (a) Time trace of the single emitter H1, which exhibits strong blinking. The variation of the count rate in the upper state is attributed to a drift of the setup. (b) Detail of the time trace of the same emitter.

and dark state respectively.

Outliers with very long time intervals are omitted here. The dashed lines are kernel density estimators of the distribution of the respective time intervals. This implies that every data point is represented with a Gaussian function and the resulting functions are added up to model the whole data. The red solid line is an exponential fit of the distribution of time intervals in the bright state. The high p-value of 0.92 confirms the goodness of the fit. The median time interval in the bright state obtained by the exponential fit amounts to 0.09 s. While other literature about solid state quantum emitters reports an exponential probability distribution for both time intervals in bright and dark states[?, ?], we found a log-normal probability distribution for the time interval in the dark state. The solid blue line in Figure 6.12 is a log-normal fit of the distribution of the time intervals in the dark state. A Kolmogorov-Smirnov test yields a p-value of 0.77 for the log-normal fit and is by far the best model to describe the data distribution. For comparison: The p-value of an exponential fit amounts to 0.36. The median time interval in the dark state obtained by the log-normal fit is determined as 0.10 s, therefore being close to the median time interval in the bright state. Very long time intervals are not shown in the plot for better visualization of the small timescales, however these long time intervals are included in the fit. The longest measured time interval amounted to 41.14 s and occurred in the dark state.

Measurements of blinking time intervals in [?] and [?] report time intervals between about 0.03 s to 1 s, and 0.1 s to 2 min, respectively. These findings are in good agreement with our measurements.

In general, excitation and emission process is mediated by charge separation (i.e. excitons). If an electron or hole is localized far enough that there is sufficiently negligible overlap with the wave function of the remaining carrier, blinking occurs [?]. We explain the observed blinking as a manifestation of the local crystal disorder due to disloca-

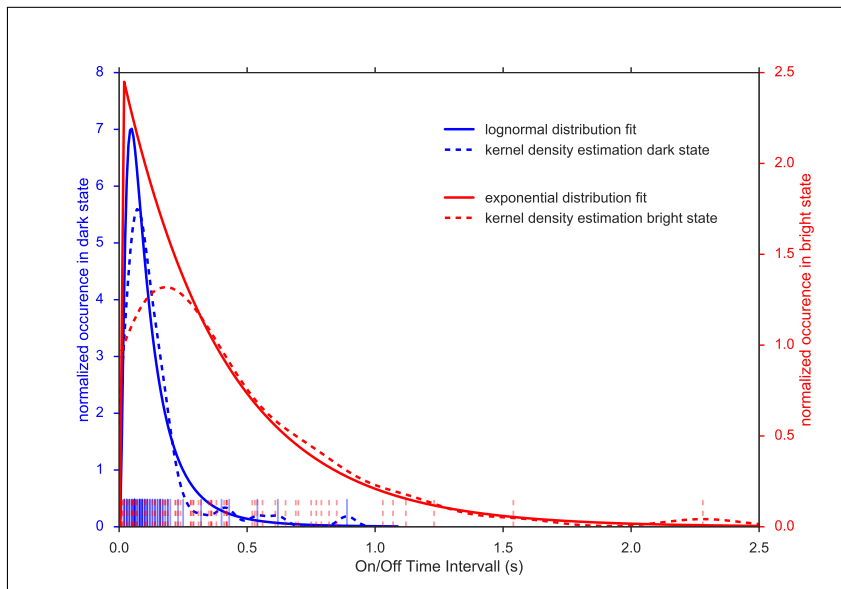


Figure 6.12: Time intervals of the single emitter exhibiting the highest blinking rate in the bright (red) and dark (blue) states. Each flank of the blinking state was individually read out from the photoluminescence time trace. On the horizontal axis small vertical lines represent the individual data points of the bright/dark time intervals. The blue and red dashed curves represent kernel density estimations of the distribution of time intervals of the dark and bright states, respectively. The y-axis is scaled to the normalized kernel density estimate. The red solid line is an exponential fit of the bright state time intervals whereas the blue solid line is a log-normal fit of the dark state time intervals. These fitting functions were chosen because they provide the best agreement with the data using a Kolmogorov-Smirnov test with respect to other functions (p-values: bright state (red) 0.92, dark state (blue) 0.77).

tions and impurities which act as a trap for the excited electron and therefore switch the emitter to the dark state. The capture of the electron of the exciton by traps due to local crystal disorders may inhibit recombination and therefore induce the dark state [?]. The assumption that dislocations and impurities are responsible for blinking emitters is in agreement with our findings reported in ??.

Research of blinking rhodamine molecules confirms power law distributed bright state times and log-normal distributed dark state times [?]. The log-normal distribution is explained by a Gaussian distribution of activation barriers of the electron transfer to trap states in the surrounding material [?]. It hints towards a recapture of the electron via multiphonon relaxation channels.

---

---

## Chapter 7

# Coupling of Nanodiamonds to Photonic Structures

In the previous chapter, we reported on photoluminescence properties of different sets of SiV centers. Across the available samples, emitters were found to exhibit considerable variations in wavelength, linewidth as well as intensity of zero-phonon-lines. This broad variety in combination with the ability to examine SiV centers individually opens up the possibility to preselect emitters according to desired spectroscopic parameters, such as narrow linewidths, high count-rates and single photon emission.

Once suitable emitters are identified, their host nanodiamonds can be moved with precision using pick-and-place methods. In particular, SiV centers may be transferred and coupled to photonic structures where their extraordinary properties can be exploited to create single photon source. Such sources are useful tools, widely required for applications in metrology and various quantum technologies such as quantum computing or quantum cryptography.

In the scope of this thesis, nanodiamonds including suitable SiV centers were identified and coupled to two different kinds of structures: Vertical-Cavity Surface Emitting Lasers (VCSELs) and plasmonic nano-antennas.

To create a hybrid-integrated single photon source, a nanodiamond containing an SiV center placed on top of a VCSEL. The SiV center is positioned such that it is directly pumped by the VCSEL output laser beam. Thus, the emission of the SiV center is steered indirectly via the operation of the VCSEL. Through the use of suitable optical filters allowing only SiV center fluorescence light to emerge, a controlled single photon source can be realized. This system is interesting in the context of metrological applications, as it constitutes a promising building block for a portable device ready to calibrate single photon detectors.

Coupling SiV centers to plasmonic nano-antennas aims at enhancing the detectable photoluminescence intensity of an emitter. As described in previous chapters, not only ZPL position and linewidth, but also the photoluminescence intensity varies strongly

among individual SiV centers. Obtaining a single photon source with a photon flux rate large enough to reliably and precisely be measured by a low photon flux detector is a key requirement for applications in metrology [?]. Furthermore, plasmonic antennas can be used to tune the emitters' photoluminescence spectrum.

## 7.1 Additional Experimental Methods

Coupling SiV centers to photonic structures requires specialized experimental methods. A range of challenges must be overcome: First, additionally to the spectroscopic preselection, the pick-and-place process poses further technical restrictions on the suitability of a host nanodiamond. The size of the host nanodiamond has to be bigger than 70 nm and they have to lie isolated on the substrate surface, i.e. with a distance of about one micrometer. This substantially reduces the number of SiV center candidates ready to be coupled to photonic structures. Another challenge is posed by accurately picking up a single nanodiamond hosting an SiV center and placing it precisely at a specified position within a given photonic structure. Furthermore, since the SiV center is to function as the photoluminescence emitter, it must not be damaged during the relocation process. To minimize both the damage cause by electron radiation, both the dose and the energy are minimized. Hence, the pick-and-place process is performed as fast as possible and with a low acceleration voltage that is just strong enough to see a hazy image of the nanodiamond.

In the context of this thesis we explored the following methods to couple nanodiamonds to photonic structures:

1. Directly spin-coat the target structures with a nanodiamond solution and consecutively look for a structure containing a nanodiamond with an SiV center exhibiting the desired spectroscopic properties. Frankly, this method relies on chance and is only feasible for the application with antenna structures due to the large number of antennas on one substrate. It is not advised to be used with VCSELs because of their morphology and the small number of VCSELs on an individual piece of substrate.
2. Identify nanodiamonds containing suitable SiV centers and individually relocate them to the destination structure using the tip in a scanning electron microscopy to perform a pick-and-place routine. For this method to be effective, nanodiamonds must have a certain size. The obvious advantage of this method is the fact that only the very best emitters are used. Furthermore, the pick-and-place process can be monitored in real-time. On the other hand, the electron radiation present during the pick-and-place process may damage the SiV center, introducing a risk of completely invalidating an emitter.
3. Identify nanodiamonds containing suitable SiV centers and individually relocate them to the destination structure using an atomic force microscope to perform a pick-and-place routine. While this method has the advantage that the nan-

odiamonds are not irradiated with electrons, the disadvantage is that it is not possible to observe the picking process in real time. As a consequence, the area of the preselected nanodiamond has to be scanned after every pick-up attempt, which is prohibitively time consuming and therefore was not further pursued after initial trials.

In the following we detail the pick-and-place technique since it the key technique in this chapter. We also discuss the properties of the nano-manipulator and how we identify nanodiamonds suitable for pick-and-place transfer. The pick-and-place process itself is very fickle and difficult to execute correctly. We are grateful for the guidance and support provided by C. Pauly, group of F. Mücklich, Saarland University in addition to the nano-manipulator setup itself.

### 7.1.1 Nano-manipulator

The nano-manipulator used for our experiments (Kleindiek, model MM3A-EM) has a exchangeable tungsten tip mounted inside a Thermo Scientific™ Helios NanoLab™ DualBeam™ microscope. This device combines a focussed ion beam and an electron microscope. The bent nano-manipulator tip can bee seen in Figure ?? has 3 degrees of freedom: up/down and left/right both in an arc up to 240°, and 12 mm in/out.

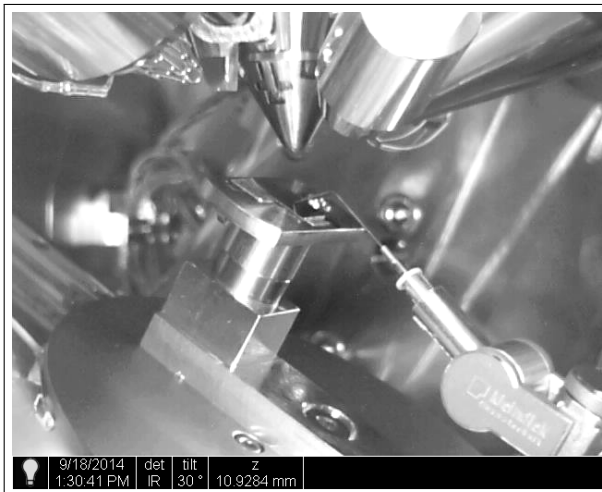


Figure 7.1: Image of the nano-manipulator mounted in the FIB. The arrows indicate the degrees of freedom of motion of the nano-manipulator. The custom made workbench is situated in the middle of the picture. On top of it, there is a  $1\text{ cm}^2$  substrate with coated nanodiamonds, the nano-manipulator tip pointing to the middle of it. Behind it, there is the target vertical-cavity surface emitting laser. Perpendicular to the workbench, the objective of the electron microscope can be seen. The angled cone perpendicular to the top edge of the image is the objective of the focussed ion beam.

Before using the nano-manipulator, its tip was “sharpened” with a focused ion beam

by etching away tungsten with gallium ions. Its final radius of curvature amounts to 100 nm. The sharpening enables the pick-up of nanodiamonds of a size suitable for use with photonic structures. In Figure 7.2a two sharpened tips are shown.

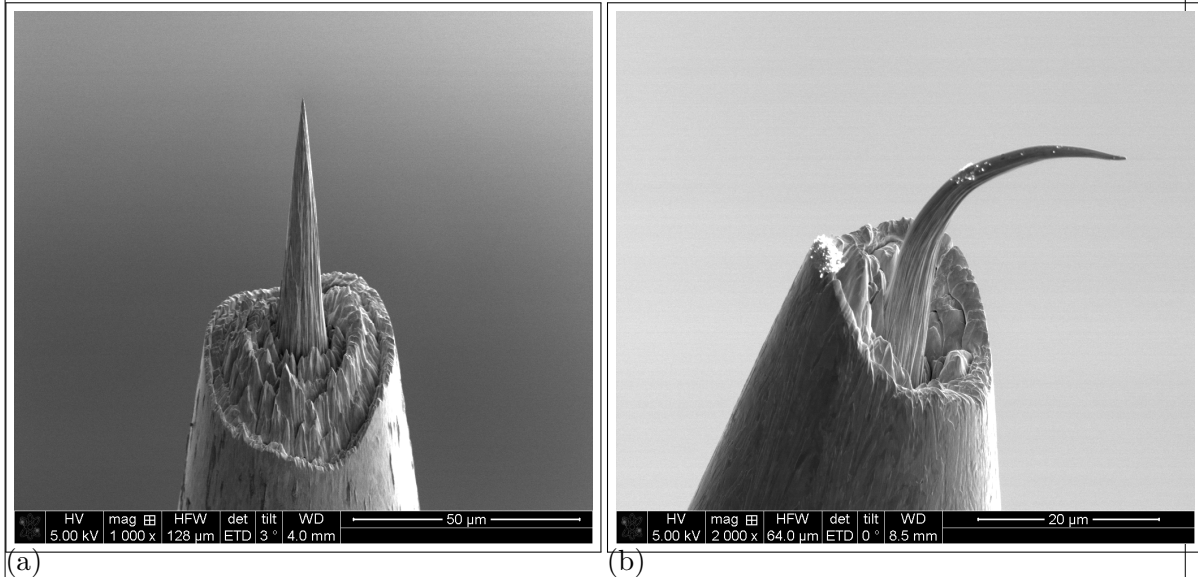


Figure 7.2: Detail of tips used as nano-manipulators. The actual tip can be seen projecting out from a bigger supporting structure. (a) Well-formed tip after sharpening. (b) Bend tip, silently attesting to the use of excessive force.

### 7.1.2 Determination of The Position of Nanodiamonds

Using the confocal setup detailed in chapter 3 we identified nanodiamonds containing SiV centers suitable for the use in photonic structures. However, to actually move those nanodiamonds to a target photonic structure the SEM setup described in the previous section must be used. This implies that after substrates containing suitable nanodiamonds are mounted in the SEM setup, the same nanodiamonds must be located on the substrate in order for the nano-manipulator to address them correctly. To facilitate this and help locate relevant nanodiamonds,  $10 \mu\text{m}^2$  cross markers with a nominal depth of 40 nm were milled into the iridium coating of the silicon substrate using the focussed ion beam prior to spin-coating the substrate with nanodiamond solution. The markers were arranged in a regular  $11 \times 11$  grid covering an area of  $0.5 \text{ mm} \times 0.5 \text{ mm}$ . Figure 7.3a illustrates a sample array. Typically three arrays of markers were milled per substrate used.

To record the position of a nanodiamond with respect to a cross marker, we used two different methods:

In the first method the confocal setup is used with a white light source illuminates the sample from the side at an acute angle. As a result, the edges of the cross markers become visible in the fluorescence light scan, see Figure 7.3b. After turning the white

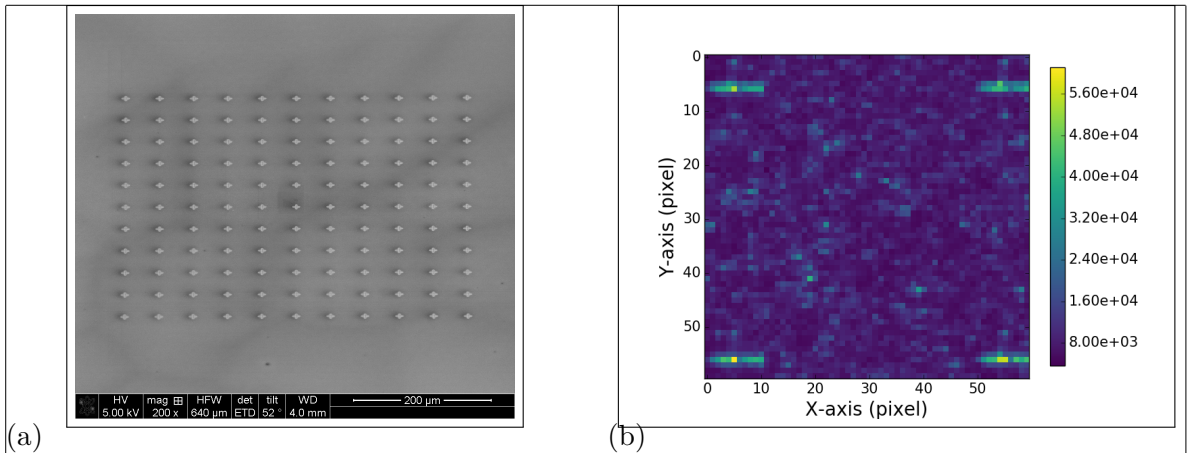


Figure 7.3: (a) Top-view of a regular array of cross markers. (b) White light scan of an area. Cross markers can be seen in all four corners.

light lamp off, the same area is scanned again to record the fluorescence from the SiV centers. An overlay of the two images identifies the position of fluorescent SiV centers with respect to the cross markers. The disadvantage of this method is the increased time consumption, as every scan for every subregion of the sample has to be performed twice. As only fluorescence light scans are performed, no information about the size of individual nanodiamonds is available. Furthermore, it remains unknown whether nanodiamonds are present in isolation or close to each other. Such information is only available in the SEM where the pick-and-place is conducted. It is only at this later stage, that individual nanodiamonds can be excluded as unusable for the pick-and-place process. For such nanodiamonds the time spend of characterizing its properties was unfortunately wasted.

To mitigate this problem, a more efficient method consists of scanning the substrate first using a commercial laser scanning microscope. The laser scanning microscope is a confocal microscope where the focus of a laser can be used to obtain the height of a structure. When scanning an array of cross markers a gray-scale image is obtained, where the gray value corresponds to the height deviation of a structure. As a result, both the crosses with a nominal depth of 40 nm and the nanodiamonds themselves are revealed as darker shades of gray. In contrast to the previous method, information on the size and isolation of nanodiamonds is accessible. After scanning the substrate with the laser scanning microscope, it is inserted into the confocal setup. While observing the surface with a CCD camera, a specific cross marker is chosen as the starting point for a fluorescence light scan. Comparing the laser scanning microscope image and a fluorescence light scan, fluorescent dots of the fluorescence light scan can be attributed to nanodiamonds in the laser scanning microscope scan. ?? illustrate the process.

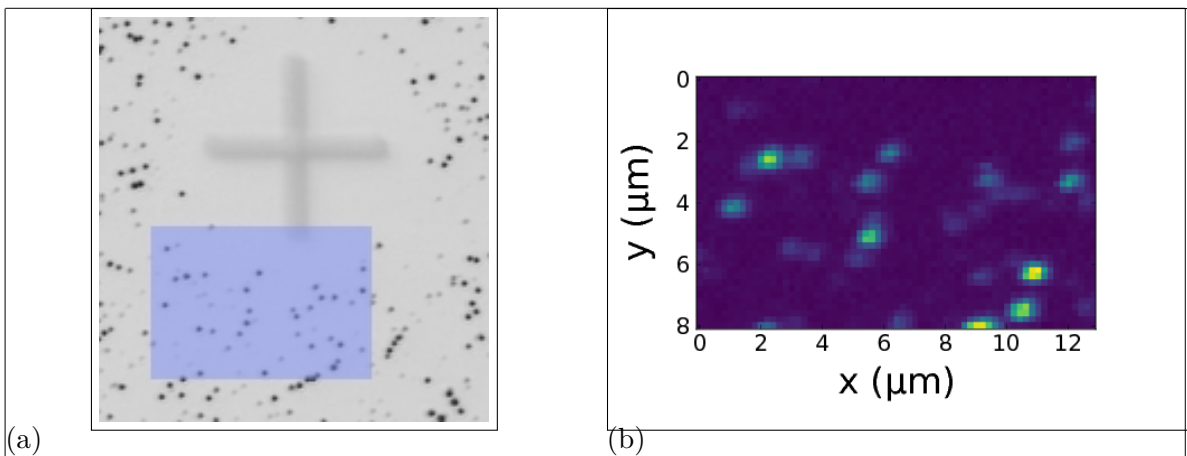


Figure 7.4: a) Picture recorded with a commercial high resolution laser scanning microscope. Cross marker is visible as well. b) Photoluminescence scan of a  $8 \mu\text{m} \times 13 \mu\text{m}$  corresponding to the blue shaded area in b). The area shaded in blue represents the photoluminescence scan in image b).

### 7.1.3 The Pick-And-Place Process

The pick-and-place process aims to transfer a select nanodiamond between two substrates using the tip mounted inside a scanning electron microscopy. The advantage of using the SEM tip as a nano-manipulator lies in the fact that the progress of the manipulation process can be visualized directly, allowing for a better control of the operation. Figure 7.5 illustrates the process.

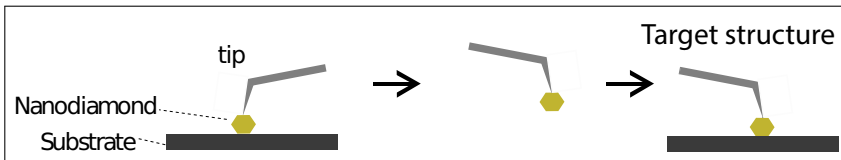


Figure 7.5: Sketch of the pick-and-place process

After we identified nanodiamonds as well-suited for transfer to the target structure, both the substrate with the nanodiamonds and the target structure were mounted inside the SEM. The process was performed using a high resolution mode with a low acceleration voltage of the SEM of 1 keV and a current of 1.7 nA. The tip is approaching the target preselected nanodiamond from above. As the SEM objective is mounted above the nanomanipulator, the proximity the nanomanipulator tip to the nanodiamond is not observable. To enable the tip of the nano-manipulator to pick up a target nanodiamond a precise approach is necessary. To facilitate this difficult procedure, the approach is divided into two stages: A coarse stage and a fine stage.

In the coarse stage the distance between tip and target nanodiamond is indirectly estimated from the shadow the tip itself casts onto the substrate and the focus area. As the tip approaches the target, the shadow of the tip starts to coincide with the nanodi-

amond position. At this point the fine stage of the approach begins in order to cover the remaining distance. To precisely control the final approach the focus of the SEM is used. Note that, as the distance between the tip and the target decreases, the focus must become sharp. Note that if the SEM is focused on the nanodiamond, the tip is out of focus and appears blurry. However, as the distance between the tip and the target decreases, the focus must become sharp. Thus the tip must be moved with utmost care until the focus becomes sharp at which point the tip touches the nanodiamond and pick-up can commence. While the process appears straightforward in concept, it is extremely challenging to operate the involved machinery to the required precision. As can be seen in Figure 7.2b it is easy to overshoot the target and to ruin the tip in the process.

When performed correctly, the nanodiamond sticks to the tip due to adhesion when the both get in contact, see Figure 7.6a. The nano-manipulator is then moved to the target structure and the approach procedure is applied in reverse. Figure 7.6b illustrates the tip of the nano-manipulator carrying a nanodiamond towards its destination structure. Depending on the material of the target structure, the nanodiamond either sticks to the structure right away due to higher adhesion forces between the nanodiamond and the structure (as is the case for golden plasmonic antennas). Alternatively, a sideways motion of the nanomanipulator tip must be used in an attempt to strike-off the nanodiamond. Either way, with patience it is possible to place a nanodiamond in a target position within a precision of a few nanometers.

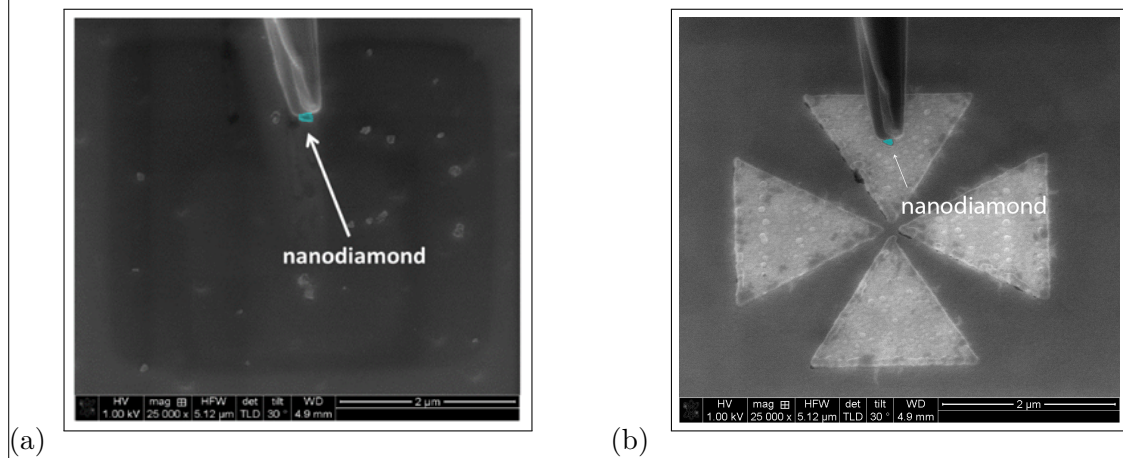


Figure 7.6: a) Tip of the nano-manipulator after successful pick-up of a nanodiamond. b) Tip of the loaded nano-manipulator approaching the target structure about to deliver a nanodiamond.

## 7.2 Coupling SiV centers to Vertical-Cavity Surface Emitting Lasers

In the context of metrology, controllable single photon sources, operating at room temperature, are an extremely important prospect. Such devices are anticipated to play a key role in the development and calibration of detectors and measurement methods aiming to resolve optical flux down to single-photon resolution [?]. As such single photon source form a cornerstone of the efforts directed towards the redefinition of the candela in terms of single photons, see discussion in chapter 1.

Here we attempt to create a hybrid-integrated single photon source by placing a nanodiamond ideally containing a solitary SiV centers on-top of a vertical-cavity surface emitting lasers (VCSELs). The SiV center is situated such that output laser of the VCSEL can be used to optically excite the color center. Since the VCSEL laser can be controlled very well, SiV center operation can be steered reliably. Through the use of suitable optical filters allowing only SiV center fluorescence light to emerge, a controlled single photon source can be realized in principle.

In the following we give a short discussion of VCSELs. Next we discuss the coupling of SiV centers to VCSELs and report on the optical properties of the resulting hybrid-integrated light source.

### 7.2.1 Vertical-Cavity Surface Emitting Lasers

A vertical-cavity surface emitting laser is a type of semi-conductor laser diode [?, ?, ?]. Figure 7.7 illustrates a common design consisting of a  $p$ -layer on top and a  $n$ -layer at the bottom separated by a so-called active area. When a current is applied across the device, charge carriers migrate towards the active region. Holes act as charge carriers in the  $p$  region, whilst electrons carry charge in the  $n$ -region. The material properties of the active region is chosen such that when electrons and holes spontaneously recombine, a photon is emitted in the process. Electron-hole pairs can also dissipated via the creation of phonons leading to losses in the form of heat. To define the region for recombination to occur and to control the optical properties of the device, additional thin layers of semi-conducting material can be introduced in the active area. These result in the formation of quantum wells with associated energy levels and resulting preferred transitions with well-defined energies for the recombination of electrons and holes.

To achieve lasing, stimulated recombination and thus stimulated emission of photons is required. To facilitate this both  $p$ -region and  $n$ -region are constructed in a layered fashion allowing them to act as highly-efficient distributed Bragg reflectors (DBR). Thus the active region is sandwiched by two mirrors forming the resonator of the laser diode. Spontaneously emitted photons thus are temporarily trapped continuously interacting with the active region. Provided the presence of sufficient electron-hole pairs, a photon

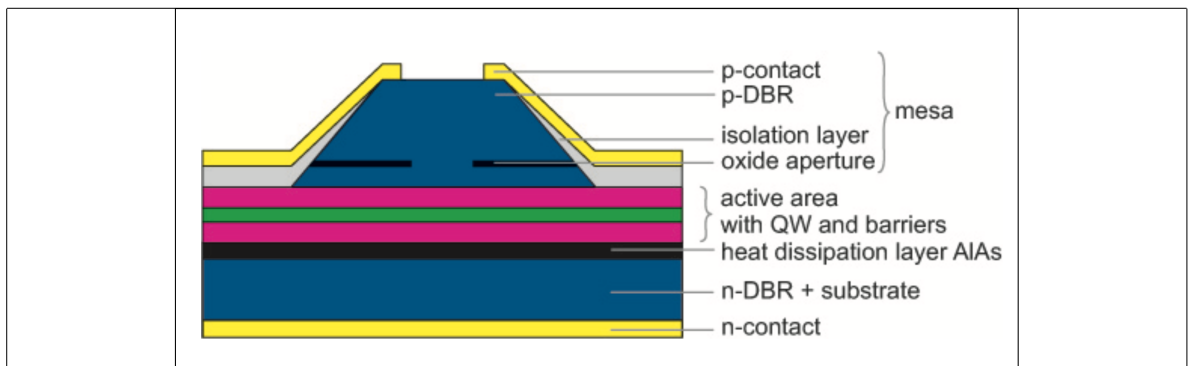


Figure 7.7: Illustration of a VCSEL laser diode [?]. When a current is applied across the device via contacts (yellow), holes and electrons migrate from the *p*-region (blue, top) and the *n*-region (blue, bottom) towards the active region (purple+green, center) where they recombine emitting photons. A quantum well is inserted in the active region, shaping the recombination process. *p*-region and *n*-region are acting as DBRs forming the resonator of the laser. When enough photons are gained by via stimulated emission, a laser beam emerges from the *p*-region after passing an oxide aperture.

can stimulate their recombination and thus the emission of further identical photons which themselves increase the stimulated emission. If enough identical photons are gained in this process, a coherent laser beam is formed by the fraction of photons escaping the resonator through the *p*-region. As a result the laser beam produced by a VCSEL is perpendicular to the substrate it resided on.

VCSELs have a range of properties that make them particularly interesting for industrial applications such low power consumption, ease of fabrication and cheap production. As a result, VCSELs are utilized in a broad range of applications including fiber optic communications or precision sensing and are used widely in commonly encountered devices such as computer mice or laser printers [?].

In the context of this thesis VCSELs offer several advantages. Their output beam is perpendicular to the substrate surface and suitable to excite SiV centers. This means that nanodiamonds containing SiV centers can simply be placed onto the device. Furthermore their physical size is ideal for the nanodiamonds we work with. The small size of VCSELs will make it easier to deploy the resulting hybrid-integrated light sources in future applications.

## 7.2.2 SiV center in a Vertical-Cavity Surface Emitting Laser

### Remark:

Gegeben einen nanodiamond ist es ja a priori unwahrscheinlich, dass ein einziges SiV center drin vorkommt. In antenneteil gehen wir darauf ein. Hier nicht. Warum nicht? Auch im Siv paper ist keine thematisierung.

To conduct our research, we received an array of red AlGaInP-based oxide-confined VCSELs from P. Michler, Stuttgart University. The array includes three individually operable VCSELs, two of which, labeled VCSEL Bm4 and VCSEL Bm2 were used in our experiments, see Figure 7.8a.

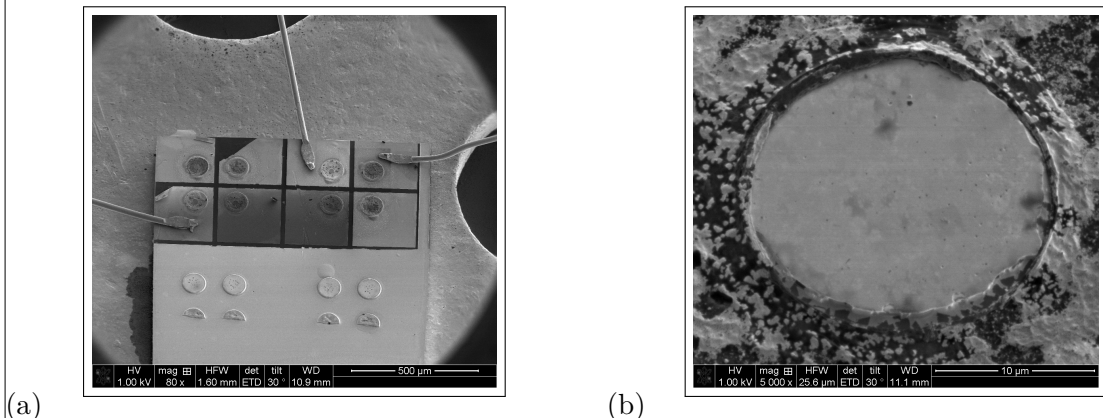


Figure 7.8: (a) SEM image of an array of VCSELs. The three wires are the anodes, which are connected to the top layer (*p*-contact) of the VCSEL. Therefore, three of the VCSEL structures can be operated. VCSEL Bm4 is located in the top right while VCSEL Bm2 to the left of it. (b) Detail SEM image of the top of VCSEL Bm4. The circular middle part is the hole in the *p*-contact through which the top DBR is visible. The smaller active diameter measures  $5.8\text{ }\mu\text{m}$  through which the laser light exits the structure is not visible in the SEM. A successful pick-and-place operation positions a nanodiamond hosting an SiV center directly in the path of the VCSELs laser.

The VCSELs we obtained use a *n*-type DBR consisting of 50 pairs of AlAs/Al<sub>0.5</sub>Ga<sub>0.5</sub>As mirror pairs while the *p*-type DBR is formed by 36 Al<sub>0.95</sub>Ga<sub>0.05</sub>As/Al<sub>0.5</sub>Ga<sub>0.5</sub>As [?]. The active region itself consists of 4 GaInP quantum wells. An oxide aperture in a field node of the standing wave serves as a spatial filter for maximum modal gain by confining the current and the optical mode. The active diameter which is defined by the oxide aperture is  $5.8\text{ }\mu\text{m}$ .

The available VCSELs are perfect candidates for the excitation of SiV centers in a hybrid integrated single photon source for several reasons. They exhibit a circular beam profile, have low divergence angle and emit linearly polarized light. Their physical size and the fact, that their output beam is perpendicular to the substrate implies that our nanodiamonds containing nanodiamonds can simply be placed on-top of the structure light-emitting region using pick-and-place methods, see Figure 7.8b. Thus the VCSELs output laser can be used to optically excite SiV centers.

As a first step towards using VCSELs to excite color centers, we characterized the behavior of VCSEL Bm4. To this end we operated it at currents of 1.5 mA and 3 mA and recorded the resulting lasing wavelength. The emission spectra showed that the emitted continuous wave laser light to be around 655 nm in wavelength for both currents, see Figure 7.9a. Previous research within the authors group recorded SiV center intensity

maxima at excitation wavelengths of 720 nm and 680 nm [?], aligning reasonably well with the output wavelength of VCSEL Bm4.

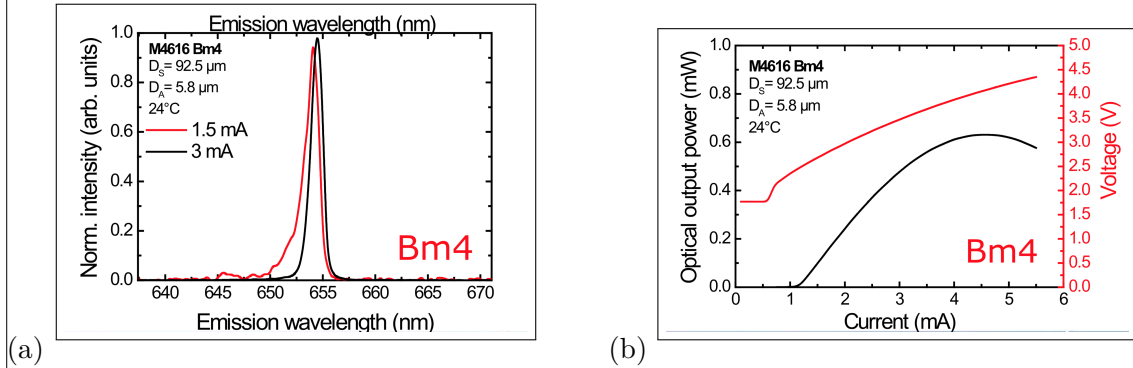


Figure 7.9: (a) Emission spectrum of VCSEL Bm4 at two different currents. (b) Optical output power and voltage of VCSEL Bm4 in dependence of input current. □

The optical output power of VCSEL Bm4 as a function of the current applied is given in Figure 7.9b. In addition, the resulting voltages are shown. It can be seen that the maximum power of  $\approx 0.6$  mW is reached for moderate currents of  $\approx 4.5$  mA. While the available optical powers are small comparable to using a conventional laser, low powers are sufficient for initial explorations.

The next step consists of selecting a suitable nanodiamond containing an SiV center followed by transferring it onto of VCSEL Bm4. To this end nanodiamonds 200 nm in size were grown with the CVD method in an iridium coated silicon wafer. We refer the reader to section 4.2 for details on the process.

Next, using the confocal setup described in chapter 3 a nanodiamond was identified exhibiting one dominant line at 746.0 nm with a linewidth of 1.9 nm. Its position on the substrate was determined consecutively using a white light laser scan as described in subsection 7.1.2. Given the position of the nanodiamond it was then transferred to VCSEL Bm4 and placed precisely in its active, i.e. light-emitting region. The process of introducing an SiV center to another structure is referred to as coupling.

After successful transfer VCSEL Bm4 was inserted into the confocal setup. Using the laser from the confocal setup we checked if the pick-and-place process caused any modification of the spectroscopic properties of the SiV center such as a decrease of count-rate or a modification of the fluorescence light spectrum. During these checks, the VCSEL itself was not active.

As a first check, we scanned the VCSEL surface in an attempt to detect the activity of the introduced SiV center. Figure 7.10a shows the SiV center as a bright dot in the aperture of VCSEL Bm4. For comparison, a Vertical-Cavity Surface Emitting Laser without coupled SiV center exhibits solely background counts which is shown in Figure 7.10b.

The spectrum of the SiV center in the transferred nanodiamond was investigated before and after the pick-and-place process. section 7.11 shows that the original spectrum

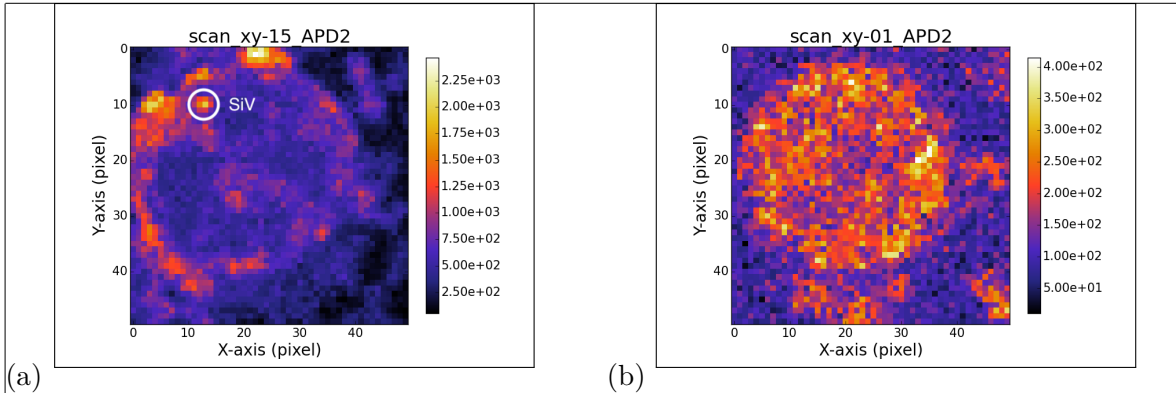


Figure 7.10: (a) Scan of the VCSEL Bm4 with coupled nanodiamond under excitation with the laser from the confocal setup. The big visible ring is the edge of the circular aperture in the *p*-contact of VCSEL Bm4. The bright spot in the upper left corner corresponds to the transferred nanodiamond containing an SiV center causing a spike in the count-rate. (b) Scan of the VCSEL Bm2 lacking a nanodiamond under excitation with the laser from the confocal setup. The circular aperture in the *p*-contact exhibits a constant count-rate. Note the different scales.

before nanodiamond transfer exhibits one dominant line at 746.0 nm, denoted line *A*. Furthermore, two minor peaks can be seen. The lower wavelength peak is denoted as line *B*. Interestingly, after the pick-and-place process, a different picture emerges shown in section 7.11. The once dominant line *A* is strongly reduced. The new dominant feature is line *B*. Note that the count rate of line *B* remained the same before and after pick-and-place.

The observed reduction of the intensity of line *A* is difficult to explain. One cause could be damage to the color center due to the electron radiation it was exposed to during the pick-and-place process. This is supported by previous research in this authors group recording reduced fluorescence light intensities after color centers were exposed to electron radiation [?]. However, the fact that line *B* remains virtually the same before and after pick-and-place is curious, raising the question whether damage alone is sufficient to explain the observed effect. As it stands, the question remains open and is thus subject to further investigation.

With line *B* as remaining dominant line we then operated VCSEL Bm4 at 1.84 mA and 3.3 V, turning off the laser of the confocal setup. Thus SiV center excitation is due to the output laser of VCSEL Bm4.

For comparison, we scanned both the surface of VCSEL Bm4 including a nanodiamond as well as VCSEL Bm2 without a nanodiamond. A bandpass filter allowing light between 730 nm to 750 nm to pass was used. This filter window suppresses the VCSEL laser line at 655 nm while leaving the SiV center emission nearly unchanged. The results of the two scans are given in Figure 7.12, where the bright areas correspond to the circular VCSEL output regions. It can be seen that no difference in brightness can be established between a VCSEL with and without a nanodiamond containing a SiV

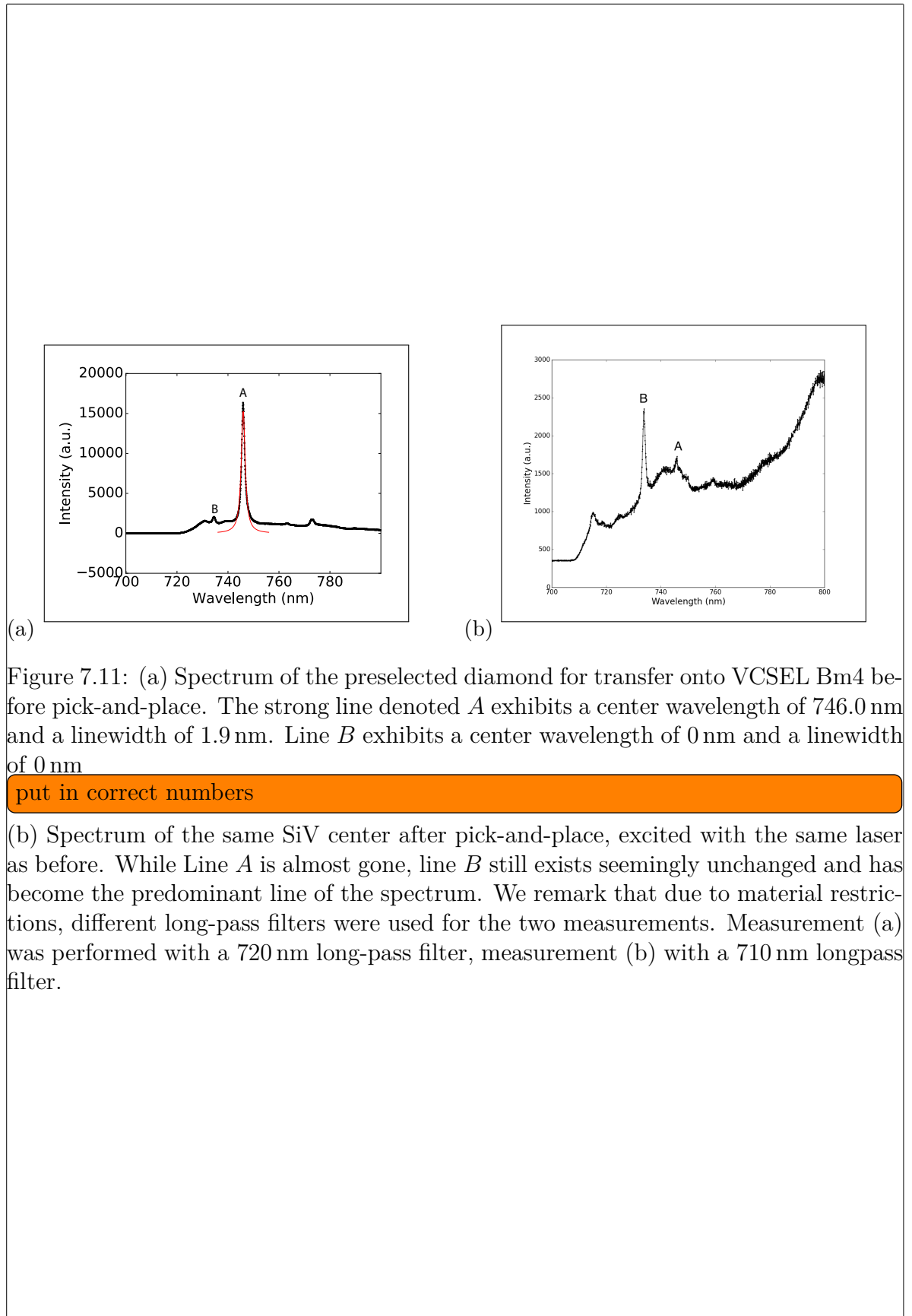


Figure 7.11: (a) Spectrum of the preselected diamond for transfer onto VCSEL Bm4 before pick-and-place. The strong line denoted *A* exhibits a center wavelength of 746.0 nm and a linewidth of 1.9 nm. Line *B* exhibits a center wavelength of 0 nm and a linewidth of 0 nm

put in correct numbers

(b) Spectrum of the same SiV center after pick-and-place, excited with the same laser as before. While Line *A* is almost gone, line *B* still exists seemingly unchanged and has become the predominant line of the spectrum. We remark that due to material restrictions, different long-pass filters were used for the two measurements. Measurement (a) was performed with a 720 nm long-pass filter, measurement (b) with a 710 nm longpass filter.

center.

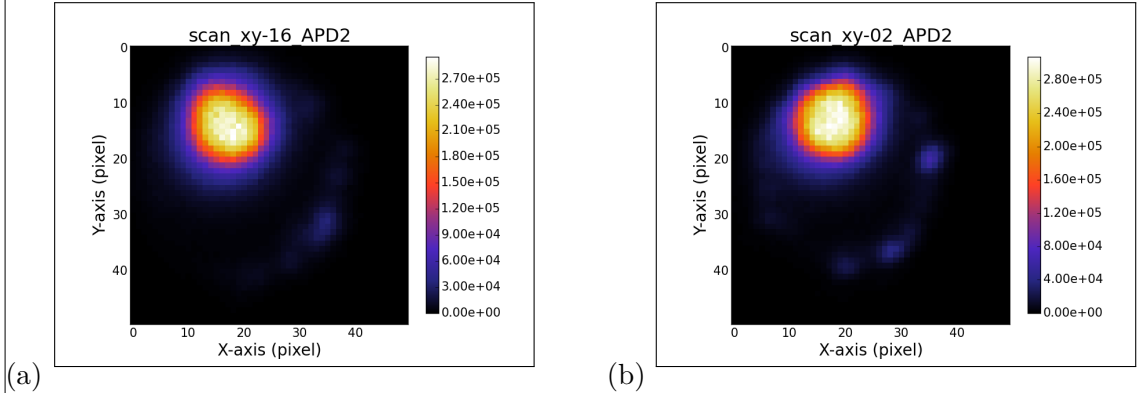


Figure 7.12: (a) Scan of the laser light stemming from VCSEL Bm4 and the fluorescence light from the SiV center in the filter window 730 nm to 750 nm. (b) Scan of the laser light stemming from VCSEL Bm2 without a coupled SiV center. The outcome of the two scans is almost identical.

To further investigate we conduct spectroscopic measurements. Since the position of the nanodiamond in VCSEL Bm4 is known, we measure the spectrum of light originating from this position. A second spectrum is obtained from VCSEL Bm2 measuring the corresponding position without a nanodiamond present. Figure 7.13 reports the results. Again no meaningful difference between the two VCSELs can be established. The lack of any distinct lines in the spectrum taken for VCSEL Bm4 which can be attributed to SiV center emission is striking.

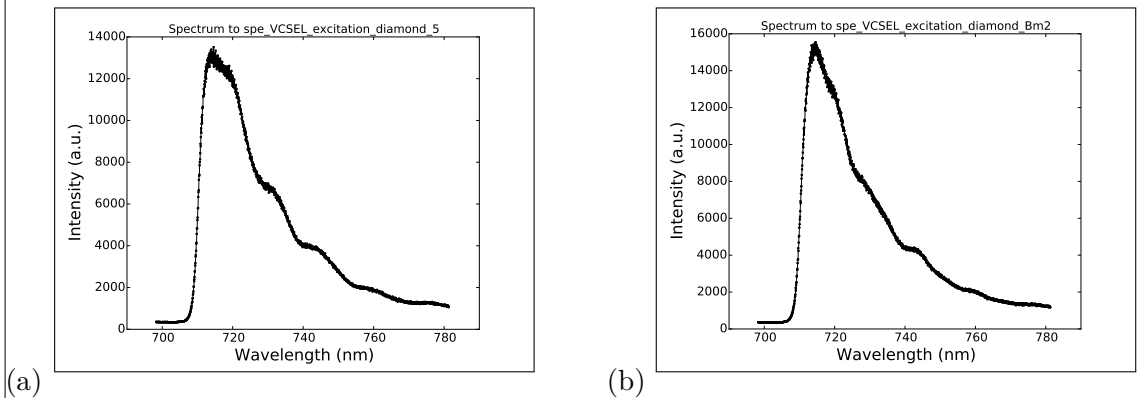


Figure 7.13: (a) Recorded Spectrum of the SiV center in the transferred nanodiamond coupled to VCSEL Bm4 during VCSEL operation. No distinct SiV center lines are visible. (b) Recorded spectrum of VCSEL Bm2.

To explain the observation, the following considerations are reasonable: The SiV center is excited by the VCSELs laser and thus emitting single photons which are passing through the filter window. The same is true for photons stemming from VCSEL side band emission. Given that the emission from the side band of VCSEL Bm4 dwarfs the

single photon emission of its SiV center, the obtained results are reasonable. To confirm we examine the reflectivity of the DBR of VCSEL Bm4. section 7.14 illustrates that the DBR exhibits imperfect reflexivity in the wavelength region relevant for SiV center emission. As a result, relevant side band emissions of VCSEL Bm4 are not sufficiently suppressed to allow for SiV center emission to be detected. This in turn means that our initial attempt to realize a hybrid-integrated single photon source by coupling an SiV center to a VCSELs is thwarted by large side band emissions of the latter.

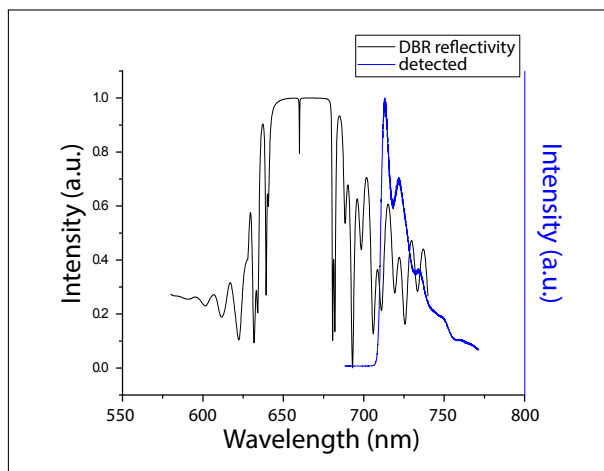


Figure 7.14: Reflectivity of the Distributed Bragg reflector (DBR) of VCSEL Bm4 [?], and a spectrum of the SiV center measured during VCSEL excitation for comparison. The reflectivity of the DBR and the VCSEL emission spectra are depicted with different scales. The shape of the measurement of the SiV center during VCSEL operation is reminiscent of the shape of the DBR reflectivity. The spectrum of the SiV center is not visible. As the emission from the SiV center is small compared to the intensity of the laser side band in the same wavelength regime, the SiV centers emission is not detectable

warum schaut das spectrum anders aus als das, was einzeln geplottet ist?

Despite a failed first attempt, a clear direction for further improvement was identified, i.e. focusing on ways to reduce VCSEL side band emission in the relevant SiV center emission regime. A promising approach to suppress the side band is to add a gold layer on top of the VCSEL acting as an additional mirror. While films of gold have a transmittance maximum at 500 nm, the transmittance minimum depends on the film's thickness [?]. Thus a gold layer could in principle be used to suppress the VCSEL side band in the SiV center emission regime. Provided such a layer can be engineered and is effective, one may expect SiV center emission to be recovered. Efforts in this direction are a required next step towards the realization of hybrid-integrated single photon sources based on SiV centers coupled to VCSELs.

## 7.3 Coupling Nanodiamonds to Double Bowtie Antenna Structures

Plasmonic nano-antennas are very recent devices designed to efficiently convert freely propagating optical radiation into localized energy and vice versa [?, ?, ?, ?, ?, ?]. Leveraging this unique property, integrating SiV centers with optical antennas creates coupled systems with a range of desirable features. These include enhanced photoluminescence emission and the ability to tailor photoluminescence spectra of the integrated emitters. The latter can be achieved by tuning the physical design parameters of the system including antenna geometry and emitter placement.

In this chapter we report on our efforts aimed at enhancing the properties of SiV centers by coupling them to optical double bowtie antennas. To this end we transfer selected nanodiamonds containing SiV centers to the target antenna structure using pick-and-place methods. After successful coupling we investigate the integrated structure experimentally. In addition to that we successfully relate some of our results to theoretical predictions.

In the following we give a short discussion of the most important properties of optical antennas. Then we sketch the actual coupling process and report on the optical properties of the resulting integrated structure. To our knowledge, our experiments were the first attempts of coupling SiV centers to plasmonic bowtie antennas.

### 7.3.1 Plasmonic Antennas

Optical nano-antennas act as converters between propagating and localized electromagnetic fields. Thus, they can be used efficiently to couple photons in and out of nano-scale objects [?]. Due to their small physical sizes, comparable or smaller than the wavelength of visible light, they are capable of focusing optical fields to sub-diffraction-limited volumes, offering the ability to manipulate electromagnetic fields at nano-scales [?, ?]. This property, dubbed sub-wavelength confinement, has successfully been exploited to enhance the excitation and emission of quantum emitters [?, ?, ?, ?] and to modify their spectra [?]. Resulting practical applications include near-field optical microscopy [?], surface enhanced spectroscopy [?, ?] and molecular sensing [?].

A nano-antenna is a nano-structure made from materials such as noble metals like gold or silver. These metals have in common that they are very susceptible to being polarized by electro-magnetic fields. When illuminated by the incident electromagnetic radiation causes electrons in the metal to behave as a plasma that tends to move with respect to the atomic lattice. As a result excess charge at the opposite surfaces of the material accumulates and the material becomes temporarily polarized until restoring forces equilibrate the charge distribution.

Thus incident light of a given frequency induces oscillations in the free electron gas density in the surface layers of the metal. At resonance these light-induced oscillations

exhibit modes of standing waves. The quasi-particles associated with these modes are known as localized surface plasmons (LSPs). For an in-depth treatment of LSPs in the context of nano-antennas we refer the reader to [?] and references therein.

Here it suffices to say, that LSPs facilitate the deciding property of optical antennas: Converting electromagnetic energy from the far-field into localized energy in the near-field. This allows, in combination with the high collection-efficiencies of nano-antennas, to efficiently couple visible radiation with wavelengths of hundreds of nanometers, into small effective spatial volumes of only a few nanometer in diameter.

To create a controlled hot-spot several antenna designs are possible. In the context of this thesis we rely on double bowtie antennas available via a collaboration with N. Rahbany, group of C. Couteau, University of Technology of Troyes. Figure 7.15 illustrates the typical bowtie antenna.

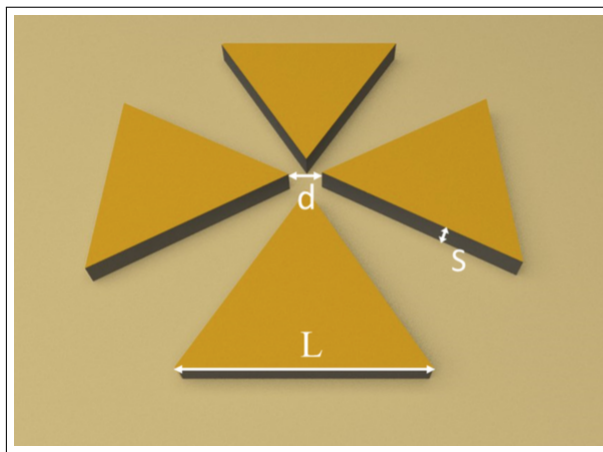


Figure 7.15: Schematic of a double bowtie antenna [?, ?, ?].

This antenna design utilizing a symmetric arrangement of four identical triangle-shaped blocks, separated by a small gap. This setup allows LSP modes local to individual blocks to couple with each other resulting in the formation of an intense hot-spot in the center area [?], see ?. The actual electromagnetic response of a double bowtie nano-antenna depends on its physical design parameters such as gap size, material used, geometry and size. Furthermore, properties of incident light such as wavelength and polarization determine antenna operation.

The improved electromagnetic field at the center of a metallic nano-antenna can be used to increase the spontaneous emission rate of emitters emitting at frequencies close to the resonance frequency of the antenna. This result is the known as Purcell effect [?]. The gap between the antenna arms acts as a resonant cavity providing a strong near field interaction with the emitter. This interaction modifies the density of states of the system, effectively providing additional modes for the emitter to decay into, thus amplifying its total decay rate. The amplification affects both radiative and non-radiative decay. The magnitude of the amplification for an emitter is quantified by the ratio of its enhanced decay rate to its free space decay rate, known as the Purcell

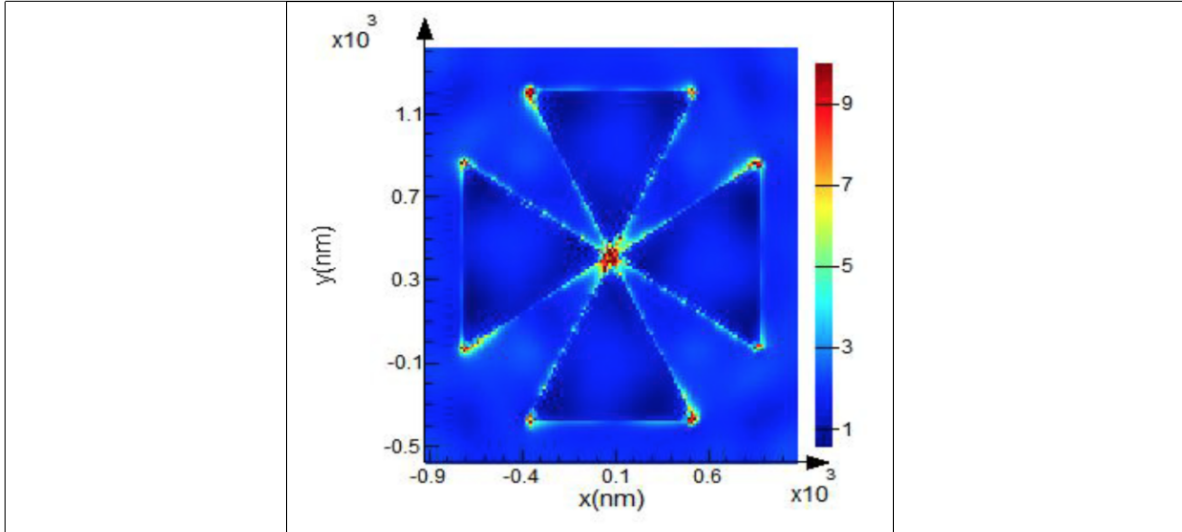


Figure 7.16: Simulation result of the electric field map of a gold double bowtie nanoantenna [?, ?, ?]. The structure has gap of  $d = 150$  nm, a side length of  $L = 2\text{ }\mu\text{m}$  and a thickness of  $S = 60$  nm. The center of the antenna exhibits an area of pronounced focus, the so-called hot-spot.

factor  $F_p$ . This factor is proportional to  $Q/V_{eff}$  where  $Q$  denotes the quality of the antenna and  $V_{eff}$  the volume of the hot-spot. Thus antenna design must optimize  $F_p$  as a necessary condition for significant enhancement of fluorescence light emission.

In addition to the antennas local field enhancement, the emitters original quantum yield  $\eta_0$  influences the overall effectiveness of the emission enhancement. From theoretical considerations [?, ?, ?, ?], the modified quantum efficiency  $\eta$  of the combined system consisting of emitter and antenna can be obtained as

$$\eta = \frac{\eta_0}{\frac{1-\eta_0}{F_p} + \frac{\eta_0}{\eta_{ant}}}, \quad (7.1)$$

where  $\eta_{ant}$  denotes the fraction of fluorescence light which is not dissipated through losses in the metal of the antenna. It is clear that an emitter with  $\eta_0 \rightarrow 1$  will not profit from the Purcell effect. On the contrary, for realistic antennas with  $\eta_{ant} < 1$  antenna-induced losses reduce the overall quantum yield  $\eta$ . Consequently poor emitters with low initial  $\eta_0$  stand to profit the most from antenna-emitter coupling provided antennas are engineered well, i.e. they maximize their Purcell Factors and minimize their losses. For an in-depth review

The presented considerations illustrate that due to their relatively low quantum efficiency, SiV centers are excellent candidates for coupling with antennas. Thus it is promising to exploit the improved electromagnetic field at the center of a double bowtie antenna to enhance the spontaneous emission rate of SiV centers and thus improve their merit as single photon sources.

### 7.3.2 Plasmonic Antenna Design and Simulation

To couple SiV centers to optical antennas, we work with gold double bowtie antennas on a gold substrate. In comparison with triangular, or single bowtie antennas, double bowtie antennas offer significantly improved intensity enhancements. Antennas were provided by N. Rahbany, group of C. Couteau, University of Technology of Troyes in a joined effort to explore the possibilities of combining antennas with SiV centers. The antennas themselves were fabricated using electron beam lithography, a technique suitable to imprint predetermined patterns onto a suitable substrate with nano-scale resolution [?]. Figure 7.17a shows a SEM image of an array of antenna structures of various sizes. In Figure 7.17b a detail of an individual double bowtie antenna is shown. It can be seen that the double bowtie antenna is placed in the center of another structure, a so-called bulls-eye antenna, consisting of multiple concentric gratings. When illuminated by a laser at a proper angle, the gratings excite surface plasmon polaritons (SPPs) which are directed towards the center of the structure. If a double bowtie antenna is present in the center, SPPs can interact with the LSPs of the double bow tie, leading to an even stronger localization of electromagnetic fields in the gap of the bowtie. While this interaction certainly merits exploration in the context of enhancing SiV centers, we omit the excitation of SPPs in our first exploration of the coupling of SiV centers and antennas. Thus the presence of the gratings can be ignored for our purposes. The reader interested in the details of bulls-eye antennas and their properties is referred to [?].

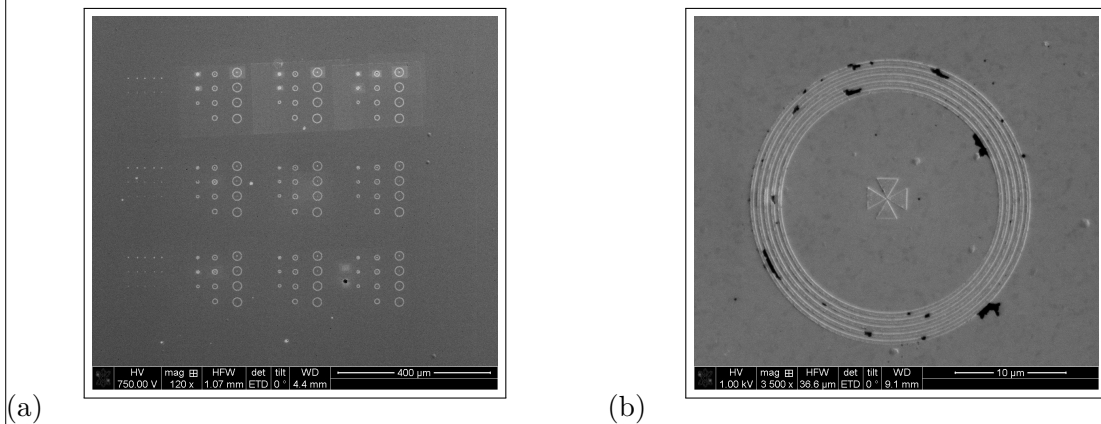


Figure 7.17: SEM images of antenna structures. (a) Overview of a field of antenna structures exhibiting various dimensions. (b) Detail of one antenna structure. In the middle the double bowtie design is visible. A grating structure consisting of multiple gratings is surrounding it.

To effectively enhance the emission of an emitter by coupling it to an optical antenna, the emission wavelength must match the resonant wavelength of the antenna. In the context of SiV centers a value of 738 nm is required. Since this value can be considered constant, the design parameters of the antenna must be chosen such, that the resulting resonance matches it. An additional constraint is placed on the size of the antenna gap,

since it must be big enough to accommodate nanodiamonds hosting SiV centers, the former are around 100 nm in size. However, it cannot be chosen arbitrarily big, since bigger gaps lead to larger effective volumes and thus smaller Purcell Factors.

Using finite time difference domain (FDTD) simulation deploying Lumerical Software the design space of gold double bowtie nano-antennas on a gold substrate was explored [?]. Although we initially attempted to simulate antennas without a nanodiamond present in the gap, it was subsequently discovered that its ab initio inclusion yielded superior results. Thus to determine usable design parameters for our purposes, an integrated system combining antenna and nanodiamond was used. To better mimic experimental conditions and associated imperfections, the nanodiamond was placed slightly off-center in the gap.

In a series of simulation it was established that a gap-size of  $d = 150$  nm, a side length of  $L = 2\text{ }\mu\text{m}$  and a structure thickness of  $S = 60$  nm are feasible parameters as referred to in ???. The simulation required the index of refraction for gold which was taken from Palik [?, ?, ?, ?].

The resulting geometry hosting a nanodiamond is capable of producing a suitable hot-spot when excited.

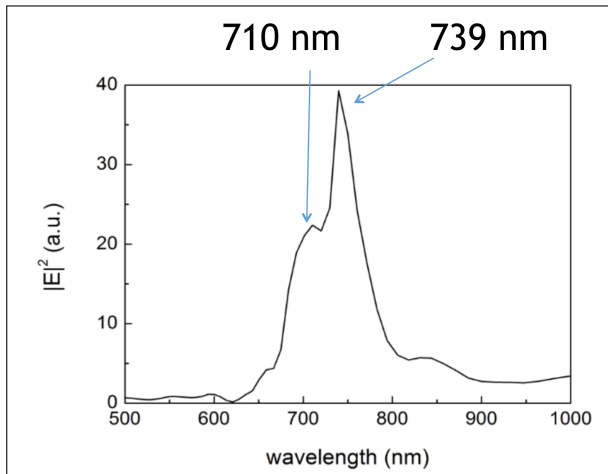


Figure 7.18: FDTD simulation of the electric field intensity of a double bowtie nano-antenna as a function of the wavelength of incident light. Two peaks are identified. The major peak corresponds exceptionally well with SiV center emission at 738 nm. The minor peak is attributed to the presence of a nanodiamond.

Finally, to pin-point the resonant wavelength for the antenna hosting a nanodiamond, the electric field intensity is simulated as a function of the wavelength of the incident light. The resulting spectrum is shown in Figure 7.18. Two resonant peaks are found. The intense major peak at 739 nm coincides exceptionally well with the SiV center emission wavelength 738 nm indicating successful antenna design. In addition to the major peak, an additional minor mode at a lower wavelength of 710 nm is found [?]. We remark that if the nanodiamond in the gap of the antenna is removed from the

simulations, the minor feature vanishes. Thus the additional peak is well-attributed to the presence of the nanodiamond.

In summary, the combined simulation results suggest, that the engineered system of nano-antenna and nanodiamond is well suited to effectively enhance the emission from an SiV center hosted in the nanodiamond. In the following sections we report on the experimental realization of this preposition.

### 7.3.3 SiV center in a Plasmonic Double Bowtie Antenna

In the following we report on our attempts to couple SiV centers to gold double bowtie nano-antennas in order to study the properties of the resulting integrated system. Ideally, a suitable nanodiamond containing exactly one SiV center is placed in the center of the antenna. The term suitable is used to summarize both desirable spectroscopic properties such as narrow-bandwidth saturated single-photon emission as well as technical requirements such as nanodiamond size and degree of isolation on the surface. Naturally, the odds of identifying and addressing a nanodiamond fulfilling all these criteria simultaneously are small. As a result identifying a perfect candidate for coupling is prohibitively time-consuming.

To mitigate this difficulty we decided to relax the condition of exactly one SiV center per nanodiamond and initiate our exploratory work with nanodiamonds containing several, potentially many active SiV centers. Relying on  $g^{(2)}(0)$  measurements we identify two interesting classes of nanodiamonds. The first class consists of nanodiamonds containing large ensembles of SiV centers acting as coherent emitters. The fluorescence light received from large ensemble of emitters is mainly coherent, leading to a flat response in the  $g^{(2)}(0)$  function. The second class of nanodiamonds we investigate features nanodiamonds hosting multiple SiV centers. As a result relevant  $g^{(2)}(0)$  measurements report weak but discernible anti-bunching dips. Both classes have in common that relevant nanodiamond specimen are significantly easier to obtain than nanodiamonds containing singleton SiV centers. Thus nanodiamonds containing ensembles of SiV centers as well as nanodiamonds containing few SiV centers are both valid starting points for our work. It is likely that the experience gained during our preliminary explorations will be valuable once nanodiamonds containing singleton SiV centers become available.

In the following sections we report on our efforts to couple nanodiamonds containing SiV centers to antennas. We illustrate the coupling process and its challenges and discuss relevant results regarding the coupling of nanodiamonds of the classes described above. We close the chapter with a short discussion and suggestions for further research.

#### Nanodiamonds Containing Ensembles of SiV centers Coupled to Antennas

**Remark:**

- fuer Figure 7.20b braucht noch das richtige bild. also eine g2 function mit coherent light
- die photostrecke pick-and-place kannst du noch nancy bilder durch deine bilder ersetzen. Ansosten muessen da noch nancy citate hin.

The nanodiamonds used for the approach of coupling ensembles of SiV centers to an antenna were wet-milled from a CVD diamond film<sup>1</sup>. The solution of nanodiamonds exhibiting a median size of 100 nm was spin-coated on an iridium substrate treated with Piranha etch. To ensure that a preselected nano-diamond exhibiting preferred optical properties can reliably be located, the iridium substrate was engraved with reference cross markers produced by a focused ion beam after the spin-coating process. After spin-coating, the sample was placed in an oven for 3 h at 450 °C to oxidize the surface and remove any residual graphite and amorphous carbon. See ?? for more information.

To determine the position of nanodiamonds on the original substrate, first a scan with a commercial laser scanning microscope (LSM) was performed as described in subsection 7.1.2. Figure 7.19a shows a part of an obtained LSM image. After transferring the sample into the confocal setup, confocal fluorescence light scans of the corresponding areas are performed to identify nanodiamonds containing active emitters. The scanned area is shown in Figure 7.19b. It corresponds to the area shaded blue in Figure 7.19a. Thus, upon close inspection some of the bright spots appearing in the fluorescence light scan can be associated with selected nanodiamonds in Figure 7.19a by eye. The correspondence between the SEM and LSM images in conjunction with the cross-markers on the substrates allows to precisely locate preselected nanodiamonds containing suitable emitter in the SEM.

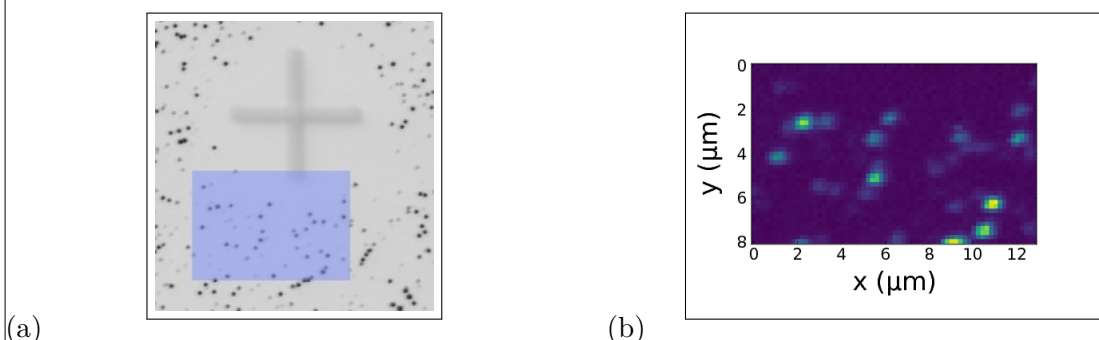


Figure 7.19: (a) Picture recorded with a commercial high resolution laser scanning microscope. Black dots are individual nanodiamonds. The cross-marker serves as an orientation aid. The area shaded in blue represents the photoluminescence scan in image (b). (b) Photoluminescence scan of a 8  $\mu\text{m} \times 13 \mu\text{m}$ .

The most promising candidate nanodiamonds are characterized by fluorescence light

<sup>1</sup>wet-milling performed by A. Muzha, group of A. Krueger, Julius-Maximilians Universität Würzburg, diamond film grown by group of O. Williams, School of Engineering, Cardiff University

spectra with very narrow zero-phonon-lines and minimal phonon side band features. Figure 7.20a shows the spectrum stemming from one such preselected nanodiamond. The ZPL feature exhibits a center wavelength of  $(738.55 \pm 0.01)$  nm and a linewidth of  $(5.00 \pm 0.03)$  nm, corresponding well with the ZPL of unstrained SiV centers. Photon autocorrelation measurements revealed that the nanodiamond contains an ensemble of SiV centers collectively generating coherent fluorescence light light, see Figure 7.20b.

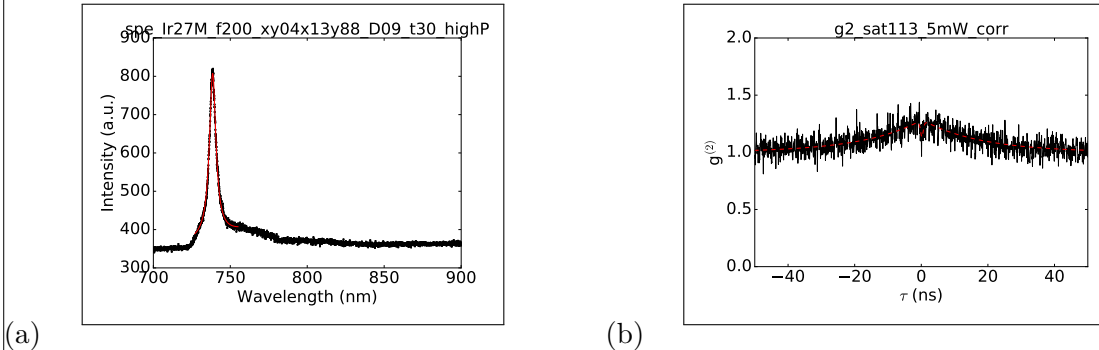


Figure 7.20: a) PL spectrum of the emitter in the preselected nanodiamond at room temperature. Black: experimental results; red: fit to experimental data, which yields a ZPL center wavelength of  $(738.55 \pm 0.01)$  nm and a linewidth of  $(5.00 \pm 0.03)$  nm. b) Intensity autocorrelation function recorded for the ensemble of emitters hosted by the nanodiamond. The flat response indicates the coherent nature of the fluorescence light light.

After a proper candidate for coupling with an antenna has been identified, it needs to be relocated from its original substrate to the antenna. To this end a pick-and-place process introduced in subsection 7.2.1 is used. A complete illustration of the steps involved is given in Figure 7.21.

We remark that the gold surface of the plasmonic antenna exhibited strong adhesion forces between the antenna surface and the nanodiamond. Once the nanodiamond touched the gold, it could not be picked up again with the tungsten tip. The nanodiamond first touched the antenna structure a few nanometers away from the gap and immediately stucked to the surface, on top of one of the triangles. Therefore, the nanodiamond had to be pushed into the gap with the nano-manipulator tip. This process caused some damage to the antenna structure. The damage is visible as black area at the tip of the top triangle in Figure 7.21e. Luckily, FDTD simulations of damaged antennas reveal that this modification of the antenna hardly influences the antenna resonance.

After successful placement, the antenna sample is installed in the confocal setup. The antenna itself was located during a scan of the sample surface under white light illumination. A scan of the antenna is performed in the confocal setup using a 660 nm continuous wave laser. It serves to locate the middle of the antenna structure and therefore the nanodiamond which had been placed there. An outline of the rings is visible in an overview scan of the antenna structure shown in Figure 7.22a. Zooming

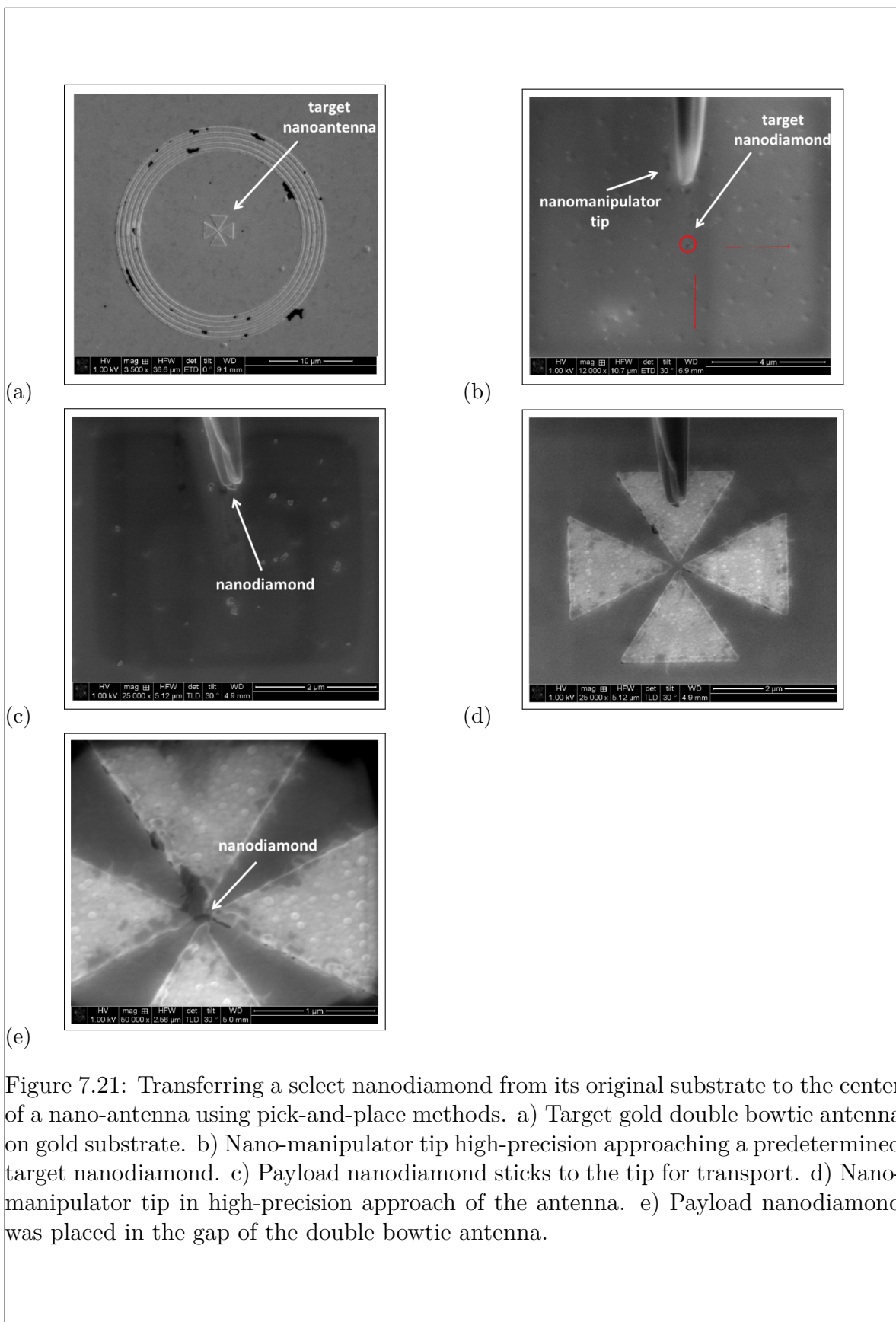


Figure 7.21: Transferring a select nanodiamond from its original substrate to the center of a nano-antenna using pick-and-place methods. a) Target gold double bowtie antenna on gold substrate. b) Nano-manipulator tip high-precision approaching a predetermined target nanodiamond. c) Payload nanodiamond sticks to the tip for transport. d) Nano-manipulator tip in high-precision approach of the antenna. e) Payload nanodiamond was placed in the gap of the double bowtie antenna.

in to the exact center of the rings, some of the edges of the bowtie antenna are vaguely visible in Figure 7.22b.

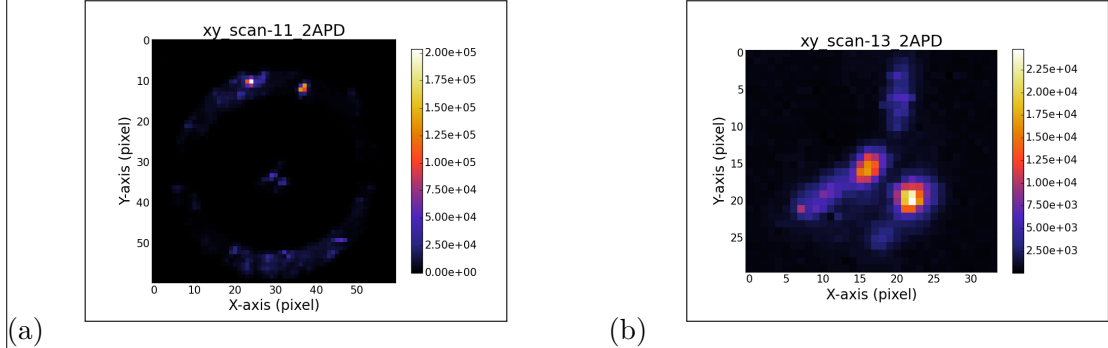


Figure 7.22: (a) Confocal scan of the double bowtie antenna where a nanodiamond containing multiple SiV centers had been placed. The rings are visible. (b) Detail scan of the triangles of the same antenna structure, which make up the double bowtie antenna. While the separate triangle cannot be seen, some edges and two bright spots are visible. To identify the place of the nanodiamond we compare the middle point of the rings in (a), the point of intersection of the edges and the bright spot and conclude that the upper bright spot in (b) is the location of the nanodiamond.

These images suffices to locate the nanodiamond with sufficient precision to measure PL spectra. The PL spectrum of the ensemble of SiV centers in the nanodiamond is shown in Figure 7.23a. It can be seen that at 738 nm a major peak is present, almost exactly at the same wavelength than the SiV center zero-phonon-line, i.e. 739 nm. The additional minor peak at 726 nm is attributed to the antenna resonance mode. We remark that, any damage sustained through electron radiation during the pick-and-place process is likely not sufficient to invalidate the nanodiamond. This is expected as a large ensemble of SiV centers can easily lose several emitters without any noticeable difference in the optical properties. Needless to say, the exact opposite is true for nanodiamonds with very few hosted SiV centers making them risky to work with.

We verified successful coupling of the ensemble of SiV centers to the antenna by combining experimental and numerical results. In particular, we convolve the experimental PL spectrum of the nanodiamond measured before placing it in the nano-antenna, see Figure 7.20a, with the intensity spectrum of the nano-antenna obtained by means of simulations given in ???. The result of the convolution is the spectrum given in Figure 7.23b. The agreement with the measured spectrum in Figure 7.23a is almost perfect, indicating successful coupling of emitters and antenna. At the same time we confirm that the minor peak in Figure 7.23a is indeed due to the antenna resonance.

Finally, keeping experimental conditions unchanged, we measure a spectrum of an identical antenna without a nanodiamond present in order to rule out surprising artifacts induced by the antenna itself. The resulting spectrum is given in Figure 7.24.

At this point one must resist the temptation of comparing the values of the intensity maxima of the spectra in Figure 7.20a and Figure 7.23a in order to determine the

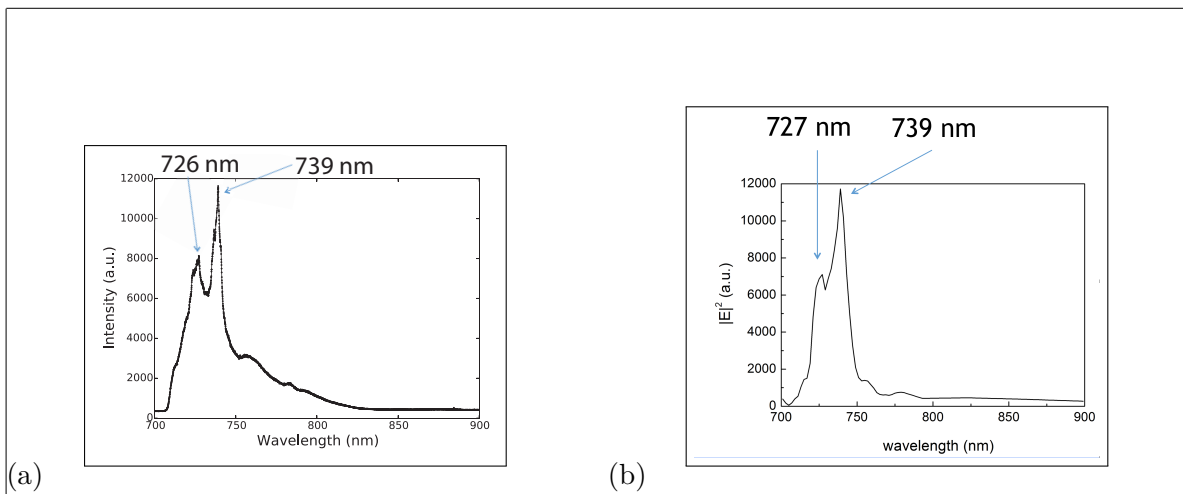


Figure 7.23: (a) Measured PL spectrum of the emitter after placing the nanodiamond into the nano-antenna, (b) Convolution of the spectrum of the measured PL spectrum of the emitter before pick-and-place, see Figure 7.20a, and the simulated resonance spectrum of the nano-antenna, see Figure 7.23a.

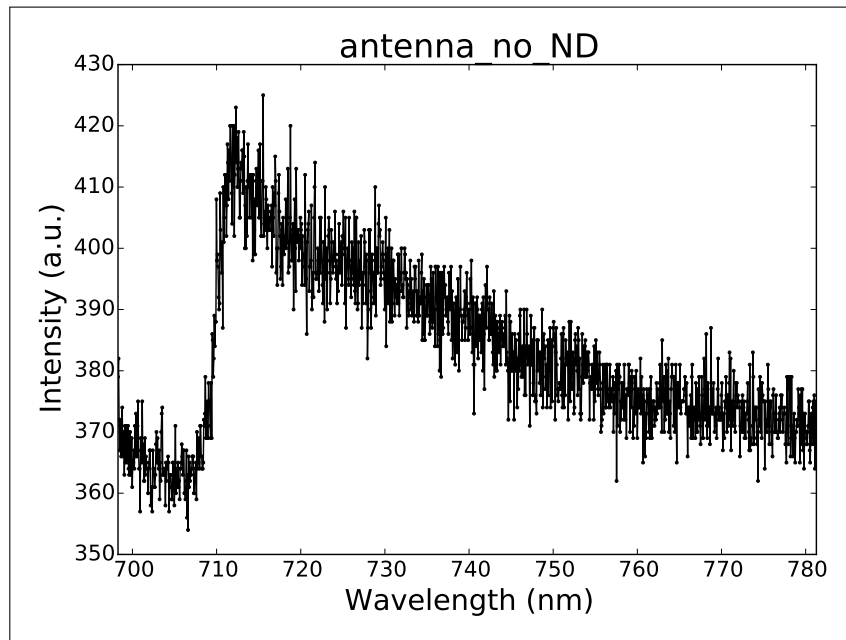


Figure 7.24: Spectrum of a gold double bowtie nano-antenna without a nanodiamond present.

enhancement the ensemble of emitters experiences. These values inherently do not allow a meaningful comparison.

A meaningful comparison can in principle be achieved via intensity saturation measurements. By measuring the saturation intensities before and after insertion into the antenna and accounting for effects related to the polarization of emitters, the magnitude of the Purcell enhancement can be determined. Unfortunately, these methods are reserved for single emitters and do not apply for ensembles of SiV centers. Thus at this point we have no method to determine the Purcell enhancement ensembles of SiV centers experience.

In summary, in this section we showed that coupling of nanodiamonds containing ensembles of SiV centers with gold double bowtie antennas is feasible using a pick-and-place approach. Furthermore we verified that the coupling is indeed present after the nanodiamond was placed in the gap of the antenna. Unfortunately, at present there is no reliable method available to us to quantify the magnitude of fluorescence light enhancement experienced by the SiV center ensemble.

### Nanodiamonds Containing Few SiV centers Coupled to Antennas

#### Remark:

- FDTD bilder fehlen komplett. Muessen unten eingefuegt werden.
- FDTD simulation fuer verschiedenen dipole orientations werden kurz erwaehnt, gibts da bilder?
- Fuer das spectrum von nanodiamond + antenne sind die locations von den subpeaks wichtig? Irgendwo sollte erwaehnt werden, dass der neue major peak nicht dort ist wo man die SiV center zero-phonon-line erwarten wuerde.
- Die fits an die subpeaks von dem spectrum nanodiamond + antenne werden nicht erklaert. Wenn die nicht wichtig sind, sollte man sie zumindest beilaeufig erwaehnen.

After a first successful validation of inserting nanodiamonds hosting large ensembles of SiV centers into a gold double bowtie antenna, we attempt to select nanodiamonds containing a comparatively small number of SiV centers. Suitable nanodiamonds show an anti-bunching dip in the  $g^{(2)}$  function in addition to count-rate saturation. This can be regarded an intermediate step towards using nanodiamonds containing singleton SiV centers. We stress that in comparison to nanodiamonds hosting large ensembles of emitters, nanodiamonds containing only a few emitters are already difficult to identify. Naturally, technical requirements applying to candidate nanodiamonds such as sufficiently isolation for picking it up in the pick-and-place process and a size not larger than that of the antenna gap still need to be observed.

The starting material for the nanodiamonds used here was an electronic grade diamond film produced by the company rho-BeSt coating (now renamed to CarbonCompetence).

The film was then milled in a bead-assisted sonic disintegration process<sup>2</sup> to nanodiamonds of a median size of approximately 100 nm. The nanodiamonds were drop-cast at 60 °C onto an iridium substrate containing cross markers. Prior to drop-casting the substrate was cleaned with Piranha etch.

Given samples containing nanodiamonds the tedious task of identifying potential candidates for transfer to the antenna. As described in the previous section, a commercial laser scanning microscope (LSM) is used to identify nanodiamonds on the substrate. Using the cross markers to address their exact positions, a corresponding fluorescence light scan allow us to single out nanodiamonds with bright emission. We further test the suitability of potential candidates as follows. First, a saturation curve is recorded to establish whether the SiV centers in a nanodiamond saturate. Since saturation is a necessary albeit not sufficient condition for single-photon emission, only nanodiamonds that saturate are capable of showing an anti-bunching dip in the  $g^{(2)}$  function. Note that, measuring the  $g^{(2)}$  function potentially requires hour-long measurements, while determining saturation requires merely seconds. Thus, in search of candidate nanodiamonds we may use the saturation behavior as a quick check whether a candidate is feasible to follow up with a lengthy  $g^{(2)}$  function measurement. For nanodiamonds containing SiV centers showing saturation we then check the spectrum to assert that the emitters are indeed SiV centers. After this last check  $g^{(2)}$  function measurements are established.

After a significant search, involving a sizable number of discarded candidates, a nanodiamond with a discernible anti-bunching dip was found. ?? shows its  $g^{(2)}$  function function while Figure 7.25b reports its saturation curve. While the dip in  $g^{(2)}$  function is quite weak, it is present and a fitting it was possible. This indicates that the nanodiamond neither contains a singleton SiV center nor does it host enough SiV centers to emit coherent light. Thus we conclude that a limited number of SiV centers must be present. While it is not possible to quantify the number of emitters directly, the candidate sufficiently differs from nanodiamonds hosting large ensembles of SiV centers. Thus it is viable to take it to the stage of coupling.

In order to relocate the identified nanodiamond to the center of a gold double bowtie antenna we repeat the pick-and-place procedure described in the previous section, see Figure 7.21. We remark at this point that since the nanodiamond in question contains fewer SiV centers as compared to the nanodiamonds hosting large ensembles of SiV centers, it is expected to be less resilient to adverse effects such as the electron radiation present during the pick-and-place process.

After a successful relocation, the sample containing the antenna is mounted in the confocal setup to investigate the properties of the combined system consisting of antenna and SiV centers. Figure 7.26a gives the spectrum of the candidate nanodiamond after being relocated to the center of a gold double bowtie antenna. Interestingly we find a multitude of individual peaks in the vicinity of the SiV center zero-phonon-line line. In addition we find that the sideband appears more pronounced in relation to the intensity

---

<sup>2</sup>A. Krueger, Julius-Maximilians Universität Würzburg

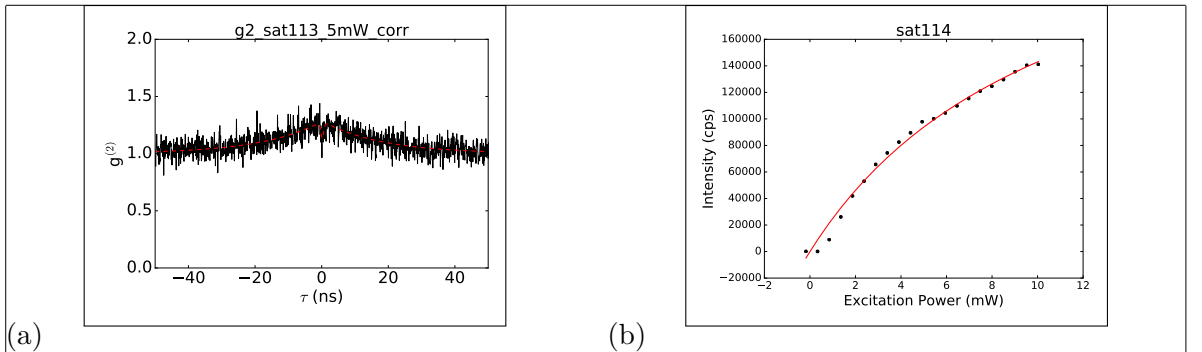


Figure 7.25: (a) The  $g^{(2)}$  function of the preselected nanodiamond believed to host a limited number of SiV centers. A dip at  $g^{(2)}(0)$  is present, however its decrease is not sufficient for a singleton SiV center. This indicates that a limited number of SiV centers is present since the absence of a dip can only be measured under coherent emission, i.e. for larger ensembles of SiV centers. The dashed red line gives a fit to the data.

cps zu a.u. aendern

. (b) Saturation curve of the same emitter

zahlen fuer sat eintragen

. Data points are black, fitted curve red.

of the major feature after the nanodiamond has been relocated to the antenna. Due to the shape of the recorded sideband we conjecture that it arises as a combination of the phonon side bands associated with individual SiV centers and additional contributions due to fluorescent contaminations. Figure 7.26b showing the spectrum of the same nanodiamond before being relocated to the antenna. Here the phonon side band is weaker in comparison to the zero-phonon-line feature.

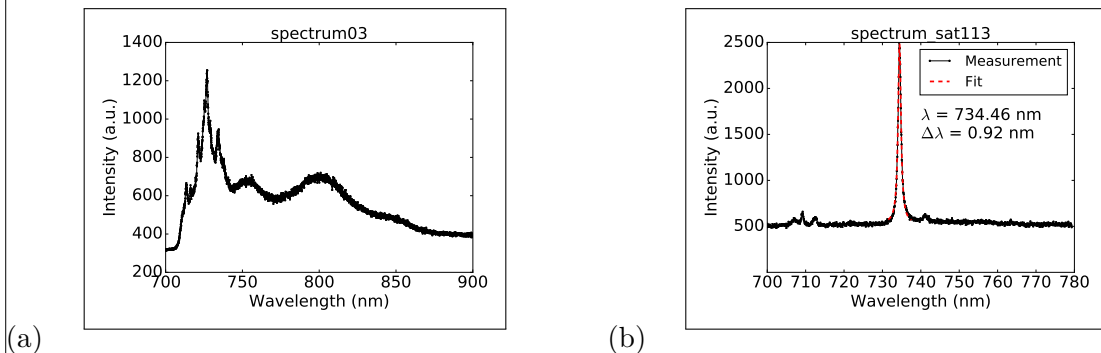


Figure 7.26: (a) Spectrum of the preselected nanodiamond hosting few SiV centers after being relocated to the center of a double bowtie antenna. (b) Spectrum of the same nanodiamond before relocation.

To exclude the possibility that the obtained peaks are artifacts due to misalignment of the experimental setup, we rechecked the alignment which proved to be precise.

To reverify the obtained spectrum, we repeated the measurement. Unfortunately, we

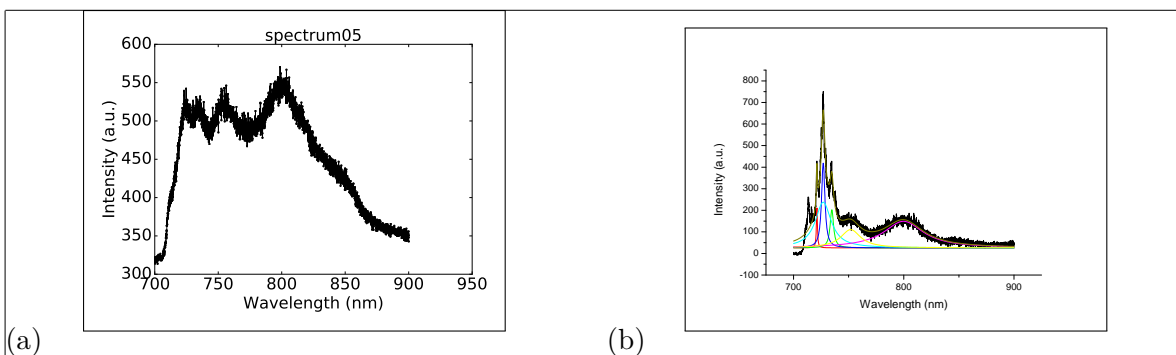


Figure 7.27: (a) Spectrum of the nanodiamond hosting few SiV centers coupled to the double bowtie antenna after the emitter bleached. (b) Background corrected spectrum of the transferred nanodiamond in the double bowtie antenna. Peaks are fitted, results of the fits are the colored lines. For background correction, the spectrum in (a) was used.

obtained an entirely different result, showing only a broad background seen in Figure 7.27a. After checking in the confocal scan that the measurement was performed at the correct position, we had to conclude that all of the SiV centers hosted by the nanodiamond permanently bleached after recording the spectrum seen in Figure 7.26a. It is likely that continued application of energy from the laser triggered this effect as earlier independent measurements established that SiV centers exhibit an increased likelihood of bleaching after being exposed to electron radiation [1]. Thus we conclude that the exposure to electron radiation during the pick-and-place left the SiV centers in an unstable state susceptible to bleaching.

Even though the nanodiamond was invalidated for further measurements, the spectrum that was obtained remains to be discussed further. To better understand the obtained observations, we turn to FDTD calculations of nanodiamond coupled to a gold plasmonic double bowtie antenna as described in the beginning of this chapter. In particular, we fold the spectrum of the nanodiamond before insertion into the antenna as given in Figure 7.26b with the simulation spectrum of the integrated system consisting of nanodiamond and antenna. The simulation result thus constitutes a prediction of what we the spectrum in Figure 7.26a should look like. ?? illustrates the simulation prediction and demonstrates that we have no reason to expect the to see the peaks between 700 nm to 750 nm observed experimentally. Hence we must conclude that the spectrum of the nanodiamond was modified during the pick-and-place process. While it is not possible to pinpoint exactly which circumstance caused the modification, several effects could influence the observed spectra.

First, the electron radiation itself. While it lacks the energy to modify the lattice itself, it can influence the electrons present and in particular may modify the charge state of SiV centers. As was mentioned before, electron radiation was linked to increased likelihood of photo-bleaching.

Next, during the pick-and-place process it is possible that the nanodiamond collects

additional contaminating matter on its surface. Contaminations may be fluorescing themselves, thus modifying the spectrum. The fact that we record a significant sideband signal in Figure 7.26a supports this conjecture.

Yet another property of SiV centers which should not be neglected is their dipole orientation interacting with the antenna. Conducting dedicated FDTD simulations with a focus on different dipole orientations indicated a dramatic effect on the resulting spectra. Therefore, future experiments aiming to investigate the effect of coupling nanodiamonds containing few SiV centers to antennas should include polarization measurements to experimentally quantify the impact of the emitter orientation.

As it stands, the most likely explanation of the recorded spectrum consists of a combination of the discussed effects. Since the nanodiamond bleached almost immediately no further measurements were possible. It is thus advised to repeat the experiment hoping for a nanodiamond that manages to complete the pick-and-place process unharmed. At the moment it is not clear if this can be done, thus further investigation is required.

# Summary and Conclusions

In this thesis we explore selected properties of the silicon color center (SiV center) hosted in nano-sized diamond grains (nanodiamonds). Studying the silicon-vacancy center in diamond is motivated by the fact that this particular color center has surfaced as a promising candidate for realizing reliable on-demand single photon sources. Such non-classical light sources are key for the proper calibration of detectors and other instruments designed to operate reliably in the single-photon counting regime. This in turn is expected to drive a shift towards quantum based radiometric SI units, such as the quantum candela, which in the long run is expected to foster improvements in our ability to work with individual photons in a wide range of practical applications.

The SiV center has the potential to add considerable momentum to this cause. It is a very efficient and stable narrow linewidth emitter, emitting single photons with high intensity. Conveniently, SiV centers operate at room temperature under normal pressure and hence do not require extremely sophisticated experimental setups. As an alternative to hosting SiV centers in bulk diamond, they can be implanted in nano-sized diamond grains offering increased collection efficiency. Grains containing individual SiV centers can be identified and preselected according to their properties. As a result individual emitters can be made mobile using pick-and-place techniques. In our work, we demonstrate that this ability unlocks applications requiring select single emitters such as coupling to antennas or the use as hybrid integrated single photon sources in conjunction with vertical-cavity surface-emitting laser (VCSEL).

To enable our research, we synthesize nanodiamonds containing SiV centers using a variety of different techniques. Chemical vapor deposition, high-pressure, high-temperature synthesis as well as wet-milling methods are used to produce a sizable set of samples. To investigate them, i.e. to study the optical properties of embedded SiV centers we rely on optical excitation. In particular, confocal microscopy is used to collect emitted fluorescence light single photons. An attached spectrometer or a Hanbury Brown and Twiss setup offer further insights into the properties of the fluorescence light emission.

Our work can roughly be subdivided into two larger explorations. The first, reported in chapter 6, revolves around charting the luminescence properties of a large set of emitters, allowing us to establish distributions of selected SiV center properties. To our knowledge, our efforts result in the largest coherent examination of SiV centers to date. In contrast to that the second exploration focuses on individual nanodiamonds and our attempts to relocate them to different nano structures in order to achieve a coupling

between SiV centers and the host structure. chapter 7 details our efforts to realize a controllable integrated single photon source by placing a nanodiamond containing SiV centers onto vertical-cavity surface emitting laser (VCSEL). Furthermore, we combine nanodiamonds with plasmonic nano-antennas in order to enhance the emission properties of the contained SiV centers. A detailed summary of the results obtained in both explorations follows below.

With regards to the investigation of large sets of emitters we find a previously unknown strongly inhomogeneous distribution of SiV center spectra in nanodiamonds. The distribution in particular suggest a partitioning of emitters according to the wavelength and linewidth of their zero-phonon-lines (ZPL) into two groups, a vertical (group V) and a horizontal (group H) group.

Group H consists of ZPLs exhibiting a narrow linewidth from below 1 nm up to 4 nm and a broad distribution of center wavelength between 710 nm and 840 nm. Compared to that, group V is comprised of ZPLs with a broad linewidth between just below 5 nm and 17 nm and center wavelength ranging from 730 nm to 742 nm. This data is consistent with previously measured SiV spectra [?, ?]. For comparison, an SiV center in unstrained bulk diamond exhibits a linewidth of 4 nm to 5 nm at a center wavelength of 737.2 nm[?, ?]. We show that both the observed blue-shift and the observed red-shift of group V are consistently explained by strain in the diamond lattice. Further, we conjecture, that group H might be comprised of modified SiV centers, the structure of which is currently unclear.

In addition to the zero-phonon-line, we also investigate the phonon side band of the available emitters. In group V we find one prominent peak at a shift of 42 meV, which corresponds to a well-known feature assigned to non-localized lattice vibrations [?, ?]. In group H we see an accumulation of peaks, at around 43 meV, 64 meV, 150 meV and 175 meV, which are consistent with sideband peaks reported in [?, ?, ?].

We further report photon autocorrelation measurements asserting the existence of single SiV centers acting as single photon source both in group H and group V. Investigating the time trace of SiV center photoluminescence, we find that some SiV centers exhibit fluorescence intermittence, also known as blinking, with on-times ranging from several microseconds up to 41 s. All but one emitters in group H exhibit blinking, where only one of the emitters in group V exhibits blinking.

Furthermore, we establish for the first time an exponential distribution for bright-time intervals and a log-normal distribution for dark-time intervals, consistent with research on single molecules [?].

After reporting the results of charting the properties of large sets of nanodiamonds and their contained SiV centers, we move on to working with individual nanodiamonds. The ability to examine SiV centers individually opens up the possibility to preselect emitters according to desired spectroscopic parameters, such as narrow linewidths, high count-rates and single photon emission.

Once such suitable candidates are identified, they can be moved between different sub-

strates with precision using pick-and-place methods. Although these methods are difficult to execute, SiV centers may be relocated and coupled to photonic structures where their extraordinary properties can be exploited to create single photon source. In the scope of this thesis, nanodiamonds including suitable SiV centers were identified and coupled to two different kinds of structures: Vertical-Cavity Surface Emitting Lasers (VCSELs) and plasmonic nano-antennas.

Red AlGaInP-based oxide-confined VCSELs are perfect candidates for the excitation of SiV centers in a hybrid integrated single photon source. Their physical size and the fact, that their output beam is perpendicular to the substrate implies that candidate nanodiamonds containing SiV centers can simply be placed on-top of the light-emitting region of the structure relying on pick-and-place methods. Then, the VCSELs output laser can be used to optically excite SiV centers, steering emission of the SiV center indirectly via the operation of the VCSEL. Through the use of suitable optical filters allowing only SiV center fluorescence light to emerge, a controlled single photon source can be realized in principle. This system is interesting in the context of metrological applications, as it constitutes a promising building block for a portable device ready to calibrate single photon detectors.

As a first step we characterize the behavior of the VCSEL itself, establishing a lasing wavelength of 655 nm for operation currents of 1.5 mA and 3 mA. At the same time a maximum output power was established  $\approx 0.6$  mW. Thus, the VCSEL is suitable for exciting SiV centers.

Next we placed a nanodiamond containing SiV centers on-top of the output region of the VCSEL using pick-and-place methods. We compare spectra of the nanodiamond before and after the relocation process and unfortunately find that the major zero-phonon-line feature at 746.0 nm disappeared with a formerly minor peak remaining as the dominant feature. Damage to the color center due to exposure to electron radiation during the pick-and-place process seems the most likely explanation for this development.

With one significant peak still remaining in the spectrum we decide to proceed to use the Vertical-Cavity Surface Emitting Laser to excite the SiV centers contained in the nanodiamond. Since the position of the nanodiamond on-top of the VCSEL is known, we measure the spectrum of light originating from this position. A second spectrum is obtained from an identical VCSEL measuring the corresponding position without a nanodiamond present. Comparing the two spectra, no meaningful difference can be found. In particular, a lack of any distinct lines in the spectrum of the VCSEL with nanodiamond attributable to SiV center emission is striking. We believe that this observation is caused by significant VCSEL sideband contributions in the wavelength range relevant for SiV center fluorescence.

Although our initial attempt to realize a hybrid-integrated single photon source by coupling SiV centers to a VCSEL is thwarted by large side band emissions of the latter, a clear direction for further improvements was identified. In particular it seems promising to explore the idea of putting an additional gold layer on-top of the VCSEL. If well-engineered it could be used a mirror to suppress the VCSEL side band in the

relevant SiV center emission regime.

After attempting to couple individual nanodiamonds and their emitters to VCSELs, we proceed to explore the possibilities of combining SiV centers with plasmonic nano-antennas. Nano-antennas are very recent nano-scale devices designed to efficiently convert freely propagating optical radiation into localized energy and vice versa. Here we use gold double bowtie antennas on a gold substrate. This design allows the creation of focused electromagnetic field at the gap in the center of the antenna, a so-called hot-spot. Placing emitters in such a hot-spot is known to increase their spontaneous emission rate provided their emission frequency is close to the resonance frequency of the antenna. This is known as Purcell effect which can be used to improve the emission of emitters [?].

In our work we aim to place a nanodiamond in the hot-spot of a double bowtie antenna in order to enhance the emission of the hosted SiV centers. A necessary condition for enhancement is that the frequencies of the SiV center emission and the resonance frequency of the antenna match. Furthermore, the gap of the antenna must be large enough to accommodate nanodiamonds. Feasible physical design parameters for the antenna meeting these requirements were determined using finite time difference domain (FDTD) simulations. After suitable antennas were fabricated, their resonance frequencies were verified experimentally.

At this point, suitable nanodiamonds containing exactly one SiV center each can be placed in the center of the antenna to study the integrated system. The term suitable is used to summarize both desirable spectroscopic properties such as narrow-bandwidth saturated single-photon emission as well as technical requirements such as nanodiamond size and sufficient degree of isolation on the surface to enable pick-and-place. Naturally, the odds of identifying and addressing a nanodiamond fulfilling all these criteria simultaneously are small. As a result identifying a perfect candidate for coupling is prohibitively time-consuming.

To mitigate this difficulty we decided to relax the condition of exactly one SiV center per nanodiamond and initiate our exploratory work with nanodiamonds containing several, potentially many active SiV centers. Relying on  $g^{(2)}(0)$  measurements we identify two interesting classes of nanodiamonds. The first class consists of nanodiamonds containing large ensembles of SiV centers acting as coherent emitters. The fluorescence light received from large ensemble of emitters is mainly coherent, leading to a flat response in the  $g^{(2)}(0)$  function. The second class of nanodiamonds we investigate features nanodiamonds hosting multiple SiV centers. As a result relevant  $g^{(2)}(0)$  measurements report weak but discernible anti-bunching dips. Both classes have in common that relevant nanodiamond specimen are significantly easier to obtain than nanodiamonds containing singleton SiV centers. Thus nanodiamonds containing ensembles of SiV centers as well as nanodiamonds containing few SiV centers are both valid starting points for our exploration. To our knowledge, our experiments were the first attempts of coupling SiV centers to plasmonic bowtie antennas.

We begin by selecting a suitable nanodiamond containing a large ensemble of SiV centers

and measure its spectrum in isolation. Using FDTD simulations we obtain the predicted spectrum of the antenna by itself without a nanodiamond present. A convolution of both spectra yields a prediction of what the spectrum of the combined system consisting of nanodiamond and antenna should look like. Indeed, our measurements of the integrated systems are congruent with the prediction asserting successful coupling facilitated by the pick-and-place method. The remarkable agreement of the theoretically predicted and the experimentally recorded spectra for an ensemble of SiV centers in a nanodiamond make our simulation assisted approach very useful and promising candidate for future explorations of antenna-emitter coupling.

We remark at this point, that a meaningful quantification of the Purcell emission enhancement induced by the coupling can in principle be achieved via intensity saturation measurements. By measuring the saturation intensities before and after insertion into the antenna and accounting for effects related to the polarization of emitters, the magnitude of the Purcell enhancement can be determined. Unfortunately, these methods are reserved for single emitters and do not apply for ensembles of SiV centers. Thus at this point we have no method to determine the Purcell enhancement ensembles of SiV centers experience.

Next we report our attempts to couple nanodiamonds hosting a limited number of SiV centers to plasmonic gold double bowtie antennas. Suitable nanodiamonds show an anti-bunching dip in the  $g^{(2)}$  function in addition to count-rate saturation. This can be regarded an intermediate step towards using nanodiamonds containing singleton SiV centers.

Analogous to the process of coupling nanodiamonds with large ensembles of SiV centers, we begin by recording the spectrum of the nanodiamond in isolation. By folding the obtained spectrum with the FTDT simulated spectrum of an antenna without nanodiamond we once again obtain a prediction of what the spectrum of the integrated system should look like. Next we relocate the nanodiamond in question to the center of the antenna using the pick-and-place method. Having assembled the integrated system, we record its spectrum to compare it with the simulation-assisted prediction. Unfortunately, this time the results disagreed significantly. This surprising event prompted us to verify the experimental setup. Since no misalignment could be detected we proceeded to redo the spectrum in an attempt to assert the spectrum obtained earlier. However, the SiV centers hosted by the nanodiamond seemed to have bleached, permanently invalidating the nanodiamond in the antenna. The obtained spectrum showed only the expected result for the antenna in isolation.

It is likely that continued application of energy from the laser triggered this effect as earlier independent measurements established that SiV centers exhibit an increased likelihood of bleaching after being exposed to electron radiation. Thus we conjecture that exposure to electron radiation during the pick-and-place left the SiV centers in an unstable state susceptible to bleaching.

Even though the nanodiamond in the antenna was invalidated for further measurements, the spectrum that was obtained in the initial measurement remains to be discussed

further.

Given the lack of agreement between measurement and simulation-assisted prediction we must conclude that the spectrum of the nanodiamond was modified during the pick-and-place process. While it is not possible to pinpoint exactly which circumstance caused the modification, several effects could influence the observed spectra. These include damage through electron radiation as well as additional fluorescing surface contaminations the nanodiamond might have picked up during the pick-and-place process. The fact that a significant sideband signals were recorded supports the latter conjecture. It also seems logical to assume that nanodiamonds containing only a few SiV centers are less resilient to radiation damage than nanodiamonds containing large ensembles of SiV centers. Yet another property of SiV centers which should not be neglected is their dipole orientation interacting with the antenna. Conducting dedicated FDTD simulations with a focus on different dipole orientations indicated a dramatic effect on the resulting spectra. Therefore, future experiments aiming to investigate the effect of coupling nanodiamonds containing few SiV centers to antennas should include polarization measurements to experimentally quantify the impact of the emitter orientation. As it stands, no conclusive explanation of the recorded spectrum and the instant bleaching are available. Thus it is advised to repeat the whole procedure starting with a different nanodiamond hosting few SiV centers.

Finally, we want to take a step back and discuss our results regarding SiV centers in the context of the quest for reliable on-demand single photon source. One of the properties that make SiV centers interesting single photon sources for the purpose of calibrating detectors is their narrow linewidth zero-phonon-line. Since detectors may have different sensitivity at different wavelength, the actual wavelength of the zero-phonon-line can become important. Thus, the existence of group H containing emitters with zero-phonon-lines of various wavelengths is interesting. In conjunction with the ability to preselect emitters according to their optical properties, candidate nanodiamonds tailored to a particular application can be found. An analogous argument is true for group V with regards to the center wavelength of emitters. However, at this point it needs to be emphasized that the preselection of emitters can quickly become an extremely tedious and time consuming process, hampering the feasibility of the approach. In particular when nanodiamonds are required that contain a single SiV center, the odds of finding suitable emitters seem painfully small at the moment.

In addition to questions of applications, our results regarding distribution of SiV center properties raise further fundamental questions. While we managed to tie the observed variety of the emitters in group V to varying strain in the nanodiamonds, a consistent explanation of the data in group H is still missing. Here we hope that our results serve as input for further research into such questions.

In our work we also explored the possibility of combining nanodiamonds containing SiV centers with other nano structures in order to create an integrated single photon source with favorable properties. To this end we utilize pick-and-place methods to relocate selected nanodiamonds to target structures. Coupling nanodiamonds to VCSELs is a promising approach to create a single photon source whose activity can be controlled

### 7.3. COUPLING NANODIAMONDS TO DARTER ANTENNAS

via the operation of the VCSELs. In our work we demonstrated the first steps towards this goal. While we also identified the first roadblock preventing us from realizing a functioning integrated single photon source for now, a promising approach to overcome it was suggested.

While coupling to VCSELs was aimed at increasing the control over the resulting integrated single photon source, coupling to antennas aims at changing the properties of the emitters via the interaction between them and the antenna. Here we managed to demonstrate successful coupling between a nanodiamond containing an ensemble of SiV centers and an antenna. However, at this point we were not able to properly quantify the enhancement emitters experience through the coupling. However, the combination of numerical FTDT simulations and experimental methods has been established as a valuable method to predict the behavior of the coupled system. Thus we recommend this method to be incorporated in future attempts of coupling SiV centers to antennas to create enhanced single photon source.

In conclusion, our research aims to contribute to the development of reliable on-demand single photon source based on SiV centers in two major ways. First, we establish properties of SiV centers over large sample sets of nanodiamonds. In doing so, we add to the understanding of this type of color center with the intention of subsequently improving our abilities to use SiV centers as constituents of integrated single photon source. To proceed in this direction we use individual nanodiamonds and couple their hosted SiV centers to various nano structures. We demonstrate successful coupling and identify valuable suggestions for further research. We hope that our contributions add momentum to the development of single photon source, to the development of novel calibration standards and photon detectors and ultimately, to the universal adoption of the quantum candela.